DESIGN, FABRICATION, AND ALIGNMENT IN MODERN OPTICS

by

Hyukmo Kang

Copyright © Hyukmo Kang 2022

A Dissertation Submitted to the Faculty of the

JAMES C. WYANT COLLEGE OF OPTICAL SCIENCES

In Partial Fulfillment of the Requirements
For the Degree of

DOCTOR OF PHILOSOPHY

In the Graduate College

THE UNIVERSITY OF ARIZONA

2022

THE UNIVERSITY OF ARIZONA
GRADUATE COLLEGE

As members of the Dissertation Committee, we certify that we have read the dissertation prepared by *Hyukmo Kang*, titled *Design, Fabrication, and Alignment in Modern Optics* and recommend that it be accepted as fulfilling the dissertation requirement for the Degree of Doctor of Philosophy.

Daewook Kim — Date: Apr 27, 2022

James T Schwiegerling — Date: Apr 27, 2022

James Schwiegerling

Yuzuru Takashima — Date: Apr 27, 2022

Yuzuru Takashima

Final approval and acceptance of this dissertation is contingent upon the candidate's submission of the final copies of the dissertation to the Graduate College.

I hereby certify that I have read this dissertation prepared under my direction and recommend that it be accepted as fulfilling the dissertation requirement.

Daewook Kim — Date: Apr 27, 2022

Daewook Kim
Dissertation Committee Chair
Optical Sciences / Astronomy

ACKNOWLEDGEMENTS

My family: Thank you for everything. I couldn't start and make it through without your support. I love you.

Daewook Kim: Thank you for your guides and all advises and inspirations. I have learned all the end-to-end attitudes about the researches. You are an amazing advisor.

Heejoo Choi: Having you in our group was a blessing. God bless you.

LOFTers: Thank you all for the incredible memories. You are the best thing that I could have during my Ph.D journey. So proud of you. We will get stronger together.

Friends in Korea: I really enjoyed our chat and hangouts. I owe you a lot.

Jummo Ahn and Junhyeok Park: I am still missing our road trips. Hope we have another chance to do that.

Robert Woerner: Thank you all for your helps. I will not forget and give it forward your kindness to anyone who needs helps.

Tucson Friends: You were my cool shades to survive in Tucson.

DEDICATION

To my family, friends, and those who walks their path.

TABLE OF CONTENTS

LIST OF FIGURES **8**

LIST OF TABLES **14**

ABSTRACT **15**

CHAPTER 1 Introduction **16**

1.1 Dwell time calculation for large optics fabrication 16

1.2 Deflectometry system alignment 17

1.3 Modular plug-in for Large Binocular Telescope 19

CHAPTER 2 GEANS: Genetic Algorithm-powered Non-Sequential Dwell Time Optimization **22**

2.1 Background 22

2.1.1 Non-sequential dwell time optimization 22

2.1.2 Genetic algorithm 24

2.2 Genetic algorithm-powered non-sequential dwell time optimization . . 25

2.2.1 Set up the bases of influence function matrix 26

2.2.2 Optimization parameters to construct influence function matrix 27

2.2.3 Optimization and fitness function 29

2.3 Verification of GEANS through simulations 31

2.3.1 CCOS simulation setup 31

2.3.2 Simulation results 33

2.3.3 Validation of GEANS 35

2.3.4 Error analysis of dwell time maps 38

2.4 Discussion 43

CHAPTER 3 Computational Vector Fiducial for Deflectometry System Alignment 44

3.1 Computational vector fiducial pattern 44
3.2 G and C polynomials 45
3.3 Reverse optimization of G and C polynomial coefficients 46
3.4 Verification of algorithm in freeform alignment 47
3.4.1 Simulation 48
3.4.2 Physical experimental demonstration 50
3.5 Discussion 53

CHAPTER 4 MOBIUS: A Modular Plug-in Spectrograph Enabling Cross-Dispersion for Large Binocular Telescope 55

4.1 Design of MOBIUS 55
4.1.1 Concepts 55
4.1.2 Design boundary conditions 57
4.1.3 Design process 58
4.2 Performance analysis 63
4.2.1 Designed performance 63
4.2.2 Table-top result 66

CHAPTER 5 Concluding Remarks 68

REFERENCES 71

APPENDIX A Genetic algorithm-powered non-sequential dwell time optimization for large optics fabrication 78

APPENDIX B Computational vector fiducial for deflectometry system alignment 96

APPENDIX C Computational alignment of on-machine deflectometry **101**

APPENDIX D Plug-in spectrograph module enabling cross-dispersion for Large Binocular Telescope **109**

APPENDIX E Modular plug-in extension enabling cross-dispersed spectroscopy for Large Binocular Telescope **129**

LIST OF FIGURES

1.1 Simple diagram of a deflectometry system [30]. The path of a single ray traced in the deflectometry system. To obtain local slope of UUT, we need the coordinates of screen pixel (x_s, y_s), detector pixel (x_d, y_d), sampled position (x_m, y_m), and distances along the optical axis from UUT to screen and detector, Z_{m2s}, Z_{m2d}. 18

1.2 An example spectrum model of an asteroid 25143 Itokawa. By comparing and fitting spectra models with measurement data, we can estimate the composition of the observation target. In this figure, the model suggests a composition of ol/(ol + low-Ca pyx) = 76% which is consistent with the known composition of 25143 Itokawa [33]. 19

1.3 Photos of (a) LBT, (b) one unit of MODS, and (c) LUCI. Both MODS and LUCI are existing on both sides of the binocular. Therefore each side could be configured with different instruments (mixed-mode) such as LUCI and MODS [35]. 20

2.1 Schematic diagram of genetic algorithm. Within the defined gene pool, the algorithm repeats evolving process (gray-box) until the generation number reaches to the maximum number. After all iterations, chromosome which has the highest fitness function is chosen as the optimal solution. 25

2.2 The flowchart of generating an influence matrix. Specific figures relate to each step, such as the number of groups at step will be optimized through GA. The detailed explanations are illustrated in Fig. 2.3 in the following section. 27

2.3 Parameters to be optimized through genetic algorithm. For GEANS, the number of optimization parameters is multiplied with the number of TIFs. Note that P^1 and P^2 are simulation-related parameters while P^3, P^4 and P^5 are tool-related parameters which are determined by machining capabilities. 28
2.4 Flowchart of GEANS simulation. 30
2.5 Target removal map for CCOS simulation. RMS of surface figure error is 0.749 μm. 31
2.6 CNS results dwell time maps and residual error maps. Dwell time map of (a) TIF 3 (b) TIF 2 and (c) TIF 1. Surface error maps after applying (d) TIF 3 (e) TIF 2 and (f) TIF 1 sequentially. Residual surface figure error after CNS was about about 15 nm. 34
2.7 Resulted maps from GEANS. Dwell time maps of (a) TIF 3 (b) TIF 2 (c) TIF 1. Residual surface error maps after applying (d) TIF 3 (e) TIF 2 and (f) TIF 1 in sequentially. Residual error map of GEANS was 43 nm of RMS. 35
2.8 (Left) Fitness function value over 20 generations of evolving. (Right) RMS of remained surface error and S_2 and S_3 of each generations. . . 36
2.9 The transformation of TIF 3 over generation. From left to right, as the generation is passed, the overall shape of dwell time map gets similar to the shape of target removal map (Fig. 2.5). 36
2.10 Comparison of dwell time map to show smoothing affects. Dwell time map of TIF 3 are shown here. (a) GEANS (b) GEANS without smoothing. (c) Center line profile (Red dotted lines in (a) and (b)) of each dwell time map. 37
2.11 Dwell time maps of TIF 3 when SSIM was (a) considered and (b) not considered in fitness function. Without SSIM, the resulted dwell time map was neither copying the shape of target removal map and smoothly continuous. (c) Center line profile (Red dotted lines in (a) and (b)) of each dwell time map. 38

2.12 Compared PSD of remained surface error map after considering practical operation of (a) GEANS method and (b) CNS method. PSD of GEANS was remained steady while the PSD of CNS was worsened with perturbation. 39
2.13 Histogram of dwell time slopes. X and Y axis are represented in log-scale. This different distribution in slopes of each method implies that the required maximum acceleration for GEANS is lower than CNS. 40
2.14 Variation of dwell time map when the acceleration limit (0.001 $mm/hour$) is applied. (a) Original dwell time map of TIF 3 from CNS and (b) Dwell points with high slopes were adjusted. As dwell time map was smoothed, total dwell time was extended as well. (c) Original dwell time map of TIF 3 from GEANS. (d) Slope limitation was applied but no difference in dwell time map. 41
2.15 Changes of residual error map when the acceleration limit was applied. (top row) Results from CNS and (bottom row) Results from GEANS. Slope limitation value was varied from no limits (most left column) to 10^{-5} $mm/hour$ (most right column). The RMS residual is rapidly increasing in CNS while remains same in GEANS. 42

3.1 Example images from the deflectometry simulator. (a) A Sinusoidal pattern is displayed on the screen. The yellow line represents the center of the screen, and the red outline shows the corresponding region to shine the UUT. (b) Image of UUT at the conjugated camera detector plane. (c) Fiducial screen dot pattern to generate (d) regular grid dot onto the camera detector. 45
3.2 Simulated images for computational fiducial pattern application. (a) Observed image of the fiducial pattern at the detector plane. White dots are measured patterns, and yellow circles are fiducial from the model. (b) Vector map drawn from computational yellow circles to measured white dots, which are updated in real-time. 46

3.3 Flowchart of the computational fiducial-based alignment procedure for simulation and physical experiment. 48
3.4 Surface map of sag departure from best-fit sphere for the simulation. 49
3.5 (a) Normalized sensitivity of **G** coefficients (b) Normalized sensitivity of **C** coefficients. Both graphs are represented in log scales due to small magnitudes of sensitivities. 50
3.6 Result of alignment simulation. Dotted lines mean initial random alignment error range, red lines represent mean values of remained errors, and blue boxes represent standard deviations of each. (a) Translation errors (b) Tilt errors. 50
3.7 (a) Experimental setup of deflectometry. The light source (screen) emits rays that are reflected at the UUT and collected by the camera. (b) Zoom-in view of UUT mounted on the computer-controlled rigid-body motion stage. 51
3.8 Result of physical experiments. (a) Translation errors (b) Tilt errors. 53
3.9 Improvement of surface map matching via alignment loop. 53
3.10 Similar vector behaviors between Dy and Tx. 54

4.1 The optical layout shows how MOBIUS works with LUCI. The MOBIUS-installed frame will be placed at the focal plane of LBT by substituting the traditional slit mask frame. With MOBIUS, LUCI is able to observe zJHK spectra in a single exposure without mixing between wavelength bands without additional modification in instrument settings. 56

4.2 Schematic figure of MOBIUS. (a) The pick-off mirror is placed near the focal point of LBT to deflect the input beam path (blue lines) into the plane of the mask frame. The beam is focused right after the reflection at the entrance surface of the pick-off mirror. (b) Inside of the frame mask, the beam is collimated and dispersed (green lines). The beam is reflected from the rear surface of the prism, then focused near the original focal point with shorter wavelength is located close to the prism. This process produces the cross-dispersion before the higher dispersion grating in LUCI. MOBIUS consists of two identical spectrographs to offer sky-subtraction by dithering between target and sky position. 57

4.3 Ray diagram of Littrow prism. The apex angle (α) of prism should be equal to the refractive angle to make retro-reflection. 60

4.4 Manufactured optical components of MOBIUS. (a) The pick-off mirror is made of Zerodur and gold coated. Clear aperture is 12 mm by 2 mm. (b) The spherical mirror is made of Zerodur and aluminum-coated. Clear aperture is 17.5 mm by 9 mm. (c) Littrow prism with silver-coated on rear surface. The entrance surface has about 13 mm by 8 mm of clear aperture. 61

4.5 (a) Optical layouts of a unit of MOBIUS. (b) The layout of MOBIUS mounted slit mask frame with alignment features. The frame was light-weighted to meet the weight limit of MOBIUS. Two identical spectrographs are located in plane symmetry and the slits are placed as close as possible for the sky subtraction by dithering. (c) MOBIUS with mask (black color). The mask blocks empty space of frame except the entrance to MOBIUS. 62

4.6 Spectra results at the LUCI detector. (a) When observing using LUCI and (b) LUCI with MOBIUS. With MOBIUS, spectra of each order are not overlapped up to 2.3 arcsecond of slit length. Two sets of zJHK spectra are found as the two spectrographs in MOBIUS are mirror-symmetric to allow the entrance slits to be closer together on sky. 64
4.7 Spot diagrams at the focal plane of (a) LBT and (b) when MOBIUS is inserted in each wavelength band. Numbers in the figure show the rms radius of each spot diagram. Although the rms value is increased after the MOBIUS, considering the smallest expected FWHM at the focal plane delivered from the telescope is 150 μm, the image quality is seeing-limited. 65
4.8 Ensquared energy comparison between (a) LUCI and (b) LUCI with MOBIUS-equipped. In every wavelength band, the difference in half width distance between LUCI and MOBIUS for 90% fraction energy is less than a pixel of the detector. This difference is insignificant as the expected seeing disk size is >2 pixels or 0.25 arcsecond. 66
4.9 (a) MOBIUS with pre-lightweighted frame is mounted in the table-top test setup. (b) The test setup of MOBIUS. 66
4.10 The table-top results. (a) Image without MOBIUS and (b) with MOBIUS. (c) The profile of MOBIUS spectrum along with the center gray line in (b). The length of the MOBIUS spectrum is about 110 pixels (3.3 mm) which corresponds to the expected result from the Zemax model (3.6 mm). 67

LIST OF TABLES

2.1 Ranges of parameters to be optimized through GA. These values are determined empirically. Numbers in brackets represent the range of each parameter. For example, [5:5:30] means [minimum : steps : maximum]. 32
2.2 Computing speed comparison between GEANS and CNS. 37

4.1 Tolerance results for alignment of each component and apex angle of the pick-off mirror. 63
4.2 Specification of detector for table-top test.[57] 67

ABSTRACT

As the demanded performances are being more challenging, optical systems are being more complicated. Astronomical telescopes require a larger aperture to secure light-gathering power for deep space, and advanced instruments with extended functionalities for various scientific objectives. The usage of freeform is increased in various applications to achieve improved image quality, higher throughput with a compact form factor. To satisfy these demanding requirements, innovative, efficient solutions in manufacturing/metrology are necessary. This dissertation covers contributions to the field of optical design, fabrication, and alignment techniques in modern astronomical and industrial applications. The first work is the development of a dwell time optimization for large optics which leverages the genetic algorithm, summarized in Chapter 2. The next work is the development of an alignment algorithm for deflectometry calibration, summarized in Chapter 3. The third is the development of a modular plug-in spectrograph for the Large Binocular Telescope which enables cross-dispersion and requires no heavy modification for the current instrument, summarized in Chapter 4. Each of these topics has been researched and verified through simulations and physical experiments where applicable. The key results and contributions are summarized in Chapter 5.

CHAPTER 1

Introduction

The modern optical systems are being more sophisticated as the desired performances are being more challenging. Astronomical telescopes require a larger aperture to secure light-gathering power for deep space, and advanced instruments with extended functionalities for various scientific objectives. The usage of freeform is increased in various applications to achieve improved image quality, higher throughput, and compact form factor. Since these needs of demanding requirements have pushed the current techniques to their limits, innovative, efficient solutions are necessary for the manufacturing of modern optical systems.

This dissertation presents advancements and contributions in optical fabrication and metrology techniques as well as an optical module design to extend the functionality of the existing instrument. The following sections of the chapter describe the backgrounds of each topic covered in this dissertation.

1.1 Dwell time calculation for large optics fabrication

The size of next-generation observatories is getting larger to observe deeper space to expand our understanding of the Universe. Especially, as there are less limitations in size and weights for ground telescopes, current and future projects such as Giant Magellan Telescope (GMT) [1], Thirty Meter Telescope (TMT) [2], and Extremely Large Telescope (ELT) [3, 4] have hundreds square-meter of collecting area. These telescopes contain from seven to hundreds of meter-class segmented mirrors that are aspheric or asymmetric. Thus, an efficient and robust manufacturing process of mirrors is essential to meet their extreme requirements.

Computer Controlled Optical Surfacing (CCOS) has been widely applied for large aspheric optical surface fabrication [5–12]. Dwell time calculation is a key

process as it deterministically guides the motion of surfacing tools to remove material from the workpiece at successive dwell points. The calculation aims to obtain a non-negative and smooth dwell time solution that minimizes the estimated residual errors of the workpiece.

In the case of large optics, such as GMT fabrication platform at The University of Arizona, multiple tools with different sizes and Tool Influence Functions (TIF) are utilized for a single workpiece [13–15] to efficiently correct various spatial frequencies in the surface errors. Thus, the dwell time algorithm is also expected to provide dwell times of multiple tools in the planning phase.

The present work in Chapter 2 introduces a new dwell time optimization algorithm, called GEANS (GEnetic Algorithm-powered Non-Sequential dwell time optimization) which has enhanced practicality in the actual CCOS process. The theoretical backgrounds for previous non-sequential dwell time optimization and genetic algorithm are briefly reviewed in Chapter 2.1. Detailed GEANS method is introduced in Chapter 2.2 and the improved performance is verified through simulation in Chapter 2.3. Chapter 2.4 discusses the limitations of the proposed method.

1.2 Deflectometry system alignment

The demand for robust metrology is growing as the usage of freeform optics is increasing in the high-performance systems. Deflectometry is an optical metrology method that has a high dynamic slope-measuring range while no null optics is required [16, 17]. These features make deflectometry as an attractive solution for freeform metrology since a single deflectometry can test various types of optical surfaces without extensive modifications.

Figure. 1.1 shows the concept of deflectometry. Deflectometry calculates local slopes of the Unit Under Test (UUT) using the relative coordinates of each component (illumination source, UUT, and camera), so obtaining reliable geometrical information of the deflectometry system is critical for accurate measurement. Multiple approaches were studied to calibrate the deflectometry system using external

measuring devices [17, 18], reference features with known surface [19–23], or employing optimization to estimate geometric parameters [24–29].

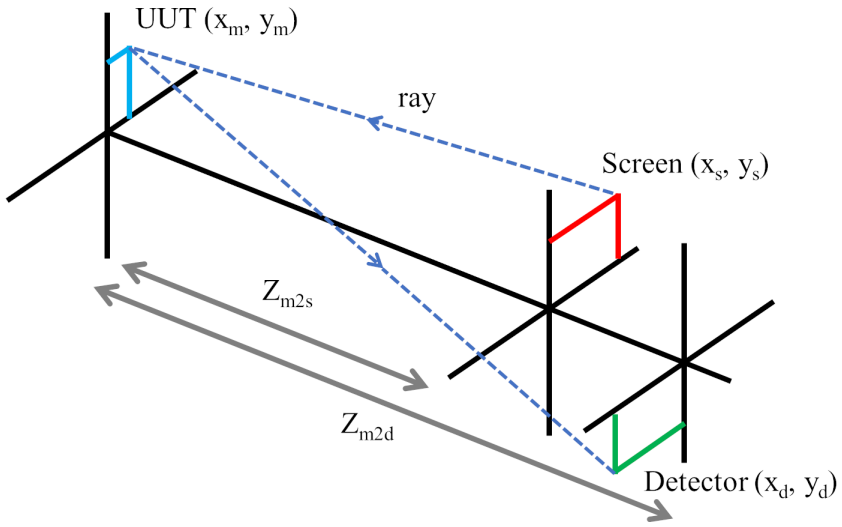


Figure 1.1 Simple diagram of a deflectometry system [30]. The path of a single ray traced in the deflectometry system. To obtain local slope of UUT, we need the coordinates of screen pixel (x_s, y_s), detector pixel (x_d, y_d), sampled position (x_m, y_m), and distances along the optical axis from UUT to screen and detector, Z_{m2s}, Z_{m2d}.

The present work in Chapter 3 introduces an alignment method based on computational vector fiducials for deflectometry. The computational fiducial is analogous to the interferometer's alignment mode, which guides the user to roughly align the test optics within the detectable range. Further, by leveraging **G** and **C** vector polynomials [31, 32], the current alignment status can be quantified for the slope measurement using deflectometry. Theoretical backgrounds and utilized software tool is introduced in from Chapter 3.1 to 3.3. The performance of the proposed algorithm is validated at Chapter 3.4 through simulation and physical experiment, and the limitations are discussed in Chapter 3.5.

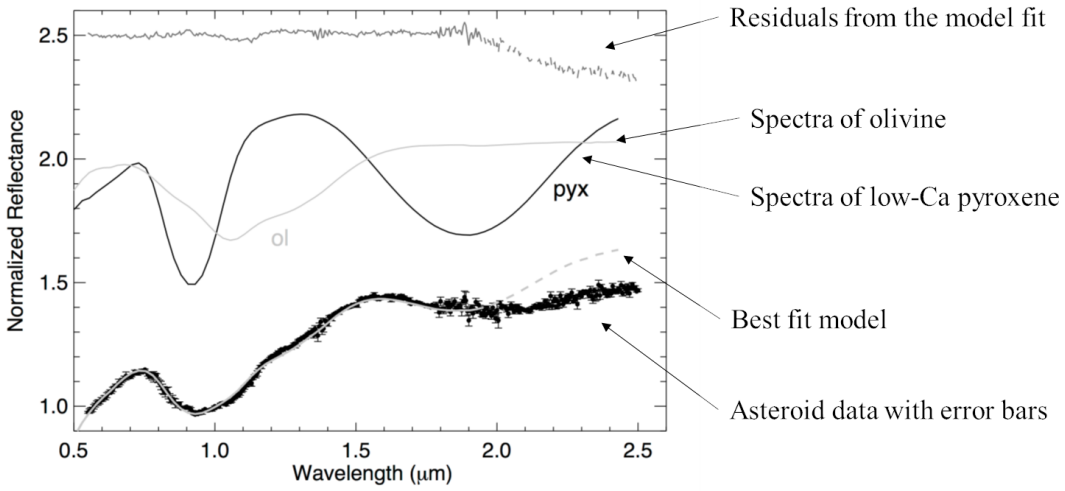


Figure 1.2 An example spectrum model of an asteroid 25143 Itokawa. By comparing and fitting spectra models with measurement data, we can estimate the composition of the observation target. In this figure, the model suggests a composition of ol/(ol + low-Ca pyx) = 76% which is consistent with the known composition of 25143 Itokawa [33].

1.3 Modular plug-in for Large Binocular Telescope

Studying asteroids or comets provide clues about the chemical composition of the primordial Solar System during its formation about 4.6 billion years ago. Spectroscopy provides clues about the surface chemical compositions of observation targets. UltraViolet (UV) to Near-InfraRed (NIR) spectra ($0.3 - 2.5\ \mu m$) have been widely used to determine surface compositions of asteroids [33]. This is because the most common components of asteroid surface materials such as pyroxene, olivine, and other mafic materials have diagnostic spectral features in these bands 1.2. It would be of benefit to observe the full UV to NIR range simultaneously.

The Large Binocular Telescope (LBT) is made up of two f/15 Gregorian telescopes, and two 8.4 m diameter primary mirrors are located side-by-side for the 11.8 m of effective diameter (Fig. 1.3(a))[34]. LBT can spectrally characterize faint objects from UV to NIR using two instruments, MODS (The Multi-Objects Double Spectrographs) (Fig. 1.3(b)) [35] and LUCI (LBT Utility Camera in the

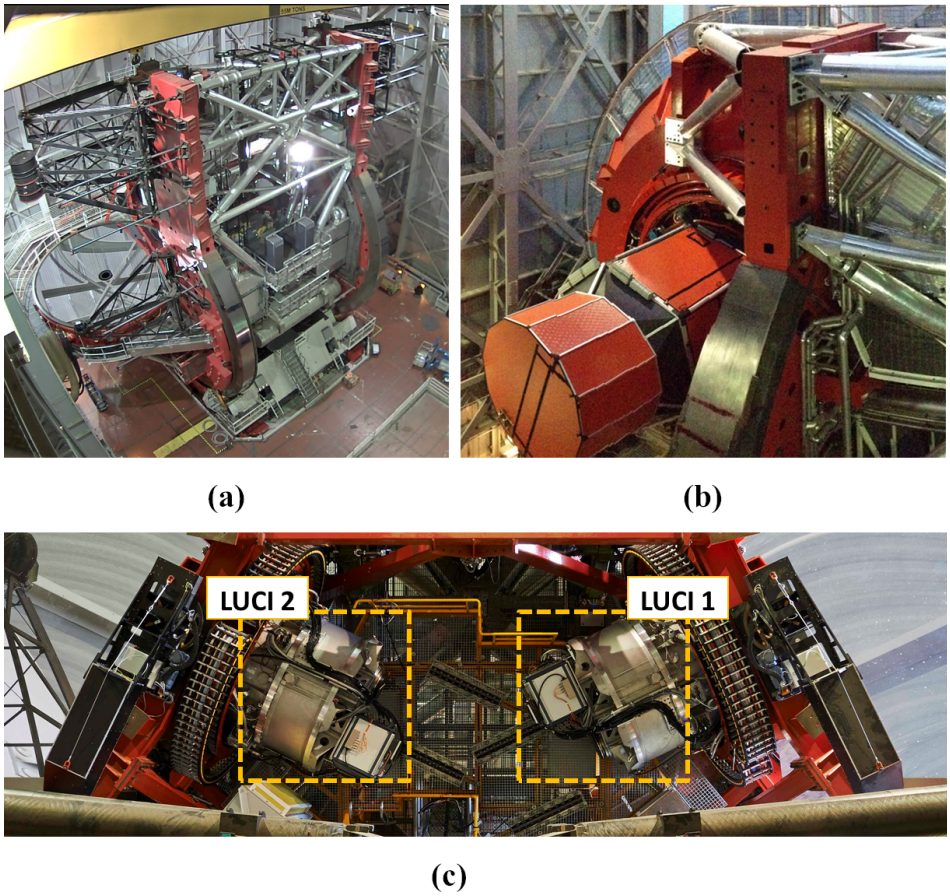


Figure 1.3 Photos of (a) LBT, (b) one unit of MODS, and (c) LUCI. Both MODS and LUCI are existing on both sides of the binocular. Therefore each side could be configured with different instruments (mixed-mode) such as LUCI and MODS [35].

Infrared) (Fig. 1.3(c)) [36]. The MODS are a pair of UV to NIR ($0.32 - 1\mu m$) imager/spectrographs, and the LUCI is a pair of NIR ($0.86\mu m - 2.4\mu m$) imagers/spectrographs. Both instruments provide long-slit spectroscopy and Multi-Object Spectroscopy (MOS). As each mirror of LBT can be equipped independently, we can configure mixed spectrographs pairs to get a continuous UV to NIR spectrum depending on scientific studies.

The present work in Chapter 4 introduces MOBIUS (Mask-Oriented Breadboard Implementation for Unscrambling Spectra) that a cross-disperser module for LBT which enables a single LUCI to cover zJHK spectrum with a single exposure. The

concept and design are described in Chapter 4.1 and the performance is demonstrated through tabletop experiment in Chapter 4.2.

CHAPTER 2

GEANS: Genetic Algorithm-powered Non-Sequential Dwell Time Optimization

This chapter is a summary of an article published at the journal *Optics Express*, Appendix A.

2.1 Background

2.1.1 Non-sequential dwell time optimization

The dwell time for multiple tools was mostly optimized sequentially until the Non-Sequential dwell time optimization method (NS) was proposed in the previous research [37]. The NS method considers multiple TIFs simultaneously in a single optimization run, which implicitly adds the necessary regularization to stabilize the linear solver. Therefore, it balances the dwell time for each tool and reduces the generation of mid-spatial-frequency errors effectively, which is a common issue in the sequential matrix-based methods[38–43].

Derived from the Preston equation [44], the material removal map ($z(x, y)$) in CCOS has been modeled as the convolution of a TIF ($t(x, y)$) with the corresponding dwell time ($d(\xi, \eta)$). When the sampling has finite resolution, the convolution process can be represented in matrix form as

$$z(x_k, y_k) = \sum_{i=1}^{N_d} t(x_k - \xi_i, y_k - \eta_i)\ d(\xi_i, \eta_i) \tag{2.1}$$

for $k = 1,\ 2,\ ...,\ N_z$, where N_z is the number of sampling points in $z(x_k, y_k)$, N_d is the number of dwell points, (ξ_i, η_i) is the ith dwell point, and $t\,(x_k - \xi_i, y_k - \eta_i)$ represents the material removed per unit time at point (x_k, y_k) when the TIF dwells at (ξ_i, η_i). Depending on the tool path or available tool overhang distance, $(x_k,\ y_k)$ and $(\xi_i,\ \eta_i)$ coordinates can be different.

In large optics fabrication, when the target removal map is $z_d(x, y)$, multiple TIFs are combined with different tool paths to achieve the desired residual error, $z_r(x, y) = z_d(x, y) - z(x, y)$, in the shortest available overall polishing time. Previous study [37] proposed the NS technique that counts multiple TIFs simultaneously in a single optimization process, which can be expressed as

$$z(x_k, y_k) = \sum_{j=1}^{N_t} \sum_{i=1}^{N_d^j} t_j(x_k - \xi_{j,i}, y_k - \eta_{j,i})\ d_j(\xi_{j,i}, \eta_{j,i}) \tag{2.2}$$

where N_t is the number of TIFs, $(\xi_{j,i}, \eta_{j,i})$ represents the ith dwell point on the tool path of the jth TIF, and N_d^j is the number of total dwell points for the jth TIF. Each TIF has its own dwell time map, and the dwell points of each TIF can be varied when necessary. By considering multiple TIFs in optimization, the NS can achieve more balanced dwell time maps for each TIF to enhance CCOS efficiency than those optimized in the sequential way [37].

Additionally, the alignment terms can be added, such as piston, tip and tilt, to the target removal amount and run optimization. This process is expressed as

$$z(x_k, y_k) = \sum_{j=1}^{N_t} \sum_{i=1}^{N_d^j} t_j(x - \xi_{j,i}, y - \eta_{j,i})\ d_j(\xi_{j,i}, \eta_{j,i}) + \sum_{l=1}^{N_a} a_l(x, y) \tag{2.3}$$

where N_a is the number of optimized alignment terms and $a_l(x, y)$ is adjusted amount of the lth term. Considering the solution of a dwell time map must be non-negative in CCOS processes, the alignment terms help relax this constraint in the optimization, although the total dwell time may increase.

The optimized dwell time map $\mathbf{d}_{opt}$ is calculated as

$$\begin{aligned} \mathbf{d}_{opt} = & \min_{\mathbf{d},\mathbf{a}} \|\mathbf{td} - (\mathbf{z}_d + \mathbf{a})\|_2^2 \\ & s.t.\ \mathbf{d} \geq \mathbf{0} \end{aligned} \tag{2.4}$$

where $\mathbf{z}_d$, $\mathbf{t}$ represent the target removal map and influence function matrix of multi-

ple TIFs for each, and **a** represents adjusted alignment map. Therefore the estimated residual error map, $\mathbf{z}_f$, can be represented as

$$\mathbf{z}_f = \mathbf{z}_d - \mathbf{td}_{opt} - \mathbf{a} \tag{2.5}$$

2.1.2 Genetic algorithm

A Genetic Algorithm (GA) is an evolutionary algorithm that models processes of natural selection to search a globally optimized solution [45, 46]. It finds an optimized solution set (*i.e.,* chromosome) which is encoded in a sequence of numbers that representing optimizing parameters (*i.e.,* gene) among given parameter candidates (*i.e.,* gene pool). Each chromosome of a population is evaluated by predefined fitness function. The next generation of population is created through following genetic operations. To prompt the evolution path towards as our preference, those operations are based on the fitness. Chromosomes with higher fitness score has more probability to be mated (selection) and transfer their genes to the next generation by exchanging genes (crossover). Especially, chromosomes which have the highest fitness can be carried to the next generation directly (elitism) to keep the superiority. While exchanging genes, some of genes can be randomly selected and changed to others with a certain probability (mutation). Often, immigrants are joining to the next generation to keep the diversity in population. Over generations, the chromosomes are evolving toward the optimal solution until the maximum number of generation. The process of GA is shown in Fig. 2.1.

The GA has a high potential in solving complex problems such as dwell time optimization in CCOS process. For example, we can guide the optimization result to reflect our preference using the fitness function with preferred target criteria. Besides, if the gene pool has practical machining parameters only, the optimized dwell time map will be achievable solution in consequence. Thus, the GA enables us to find optimal combination of parameters while considering machining feasibility or our preference in CCOS process.

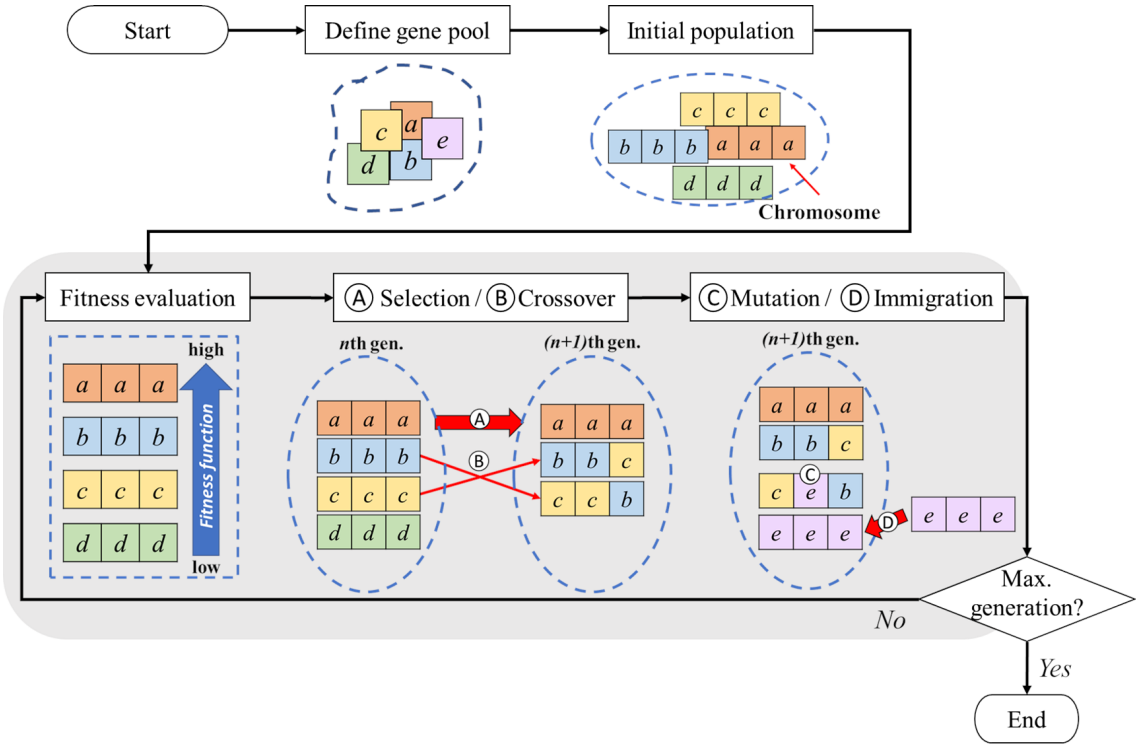


Figure 2.1 Schematic diagram of genetic algorithm. Within the defined gene pool, the algorithm repeats evolving process (gray-box) until the generation number reaches to the maximum number. After all iterations, chromosome which has the highest fitness function is chosen as the optimal solution.

2.2 Genetic algorithm-powered non-sequential dwell time optimization

The results from the Conventional NS (CNS) are mathematically ideal and show high figuring efficiency in terms of the estimated residual errors. However, they have limitations in practical application. Firstly, the hardware capabilities are not reflected during the calculation. The applicable maximum local slope of dwell time map is limited due to the finite acceleration of the Computer Numerical Control (CNC) hardware limitations. Hence a smooth dwell time map is preferred in actual CCOS processes, yet is not considered machine axis motion in CNS. Secondly, the calculated dwell time map barely resembles the target surface error map shape. Because of uncertainties in tool positioning and tool vibration, a dwell time map

that is different from the target removal map increases the risk of inducing new mid-to-high spatial frequency surface error after figuring. Lastly, as the size of the influence matrix is multiplied by the number of TIFs in CNS, the computation time rises considerably. Especially in large optics fabrication (*e.g.,* GMT 8.4 m diameter mirror segment), the computational burden is even heavier since the sizes of measured removal maps and TIFs are enormous so that iterative optimization is difficult.

The main objectives of GEANS is to enhance the performance of CNS to produce a preferable dwell time map which closely duplicates the shape of a target error map and reflects the machining capability of the CNC unit while boosting the computational efficiency. GEANS consists of two interdependent parts: Composing the bases of the influence function matrix, and optimizing the dwell time using those bases via GA.

2.2.1 Set up the bases of influence function matrix

As Eq. 2.2 is usually ill-posed, finding the dwell time map relies on an optimization process. Constructing proper building blocks of the influence function matrix enables the optimization algorithm to find desired results easily and improves computational efficiency. Dwell time bases were set up with following fundamental rules: i) grouping ii) dividing and iii) smoothing.

The first step is to form a single basis by grouping neighboring dwell points with similar removal amount. The idea of grouping is valid as adjacent dwell points with similar target removal amounts are expected to require similar dwell time distribution as well. It also benefits in computing costs as the total size of dwell time matrix is decreased. For instance, if n-points are combined and worked as a single dwell basis, the size of dwell time matrix is reduced by $n-1$. Then, if the size of a single basis is too large, the optimization engine would not have enough degree of freedom in solution space. Therefore, in the algorithm, a criterion is set and a big single basis will be divided into smaller pieces to secure flexibility in optimization so that the overall figuring efficiency can be improved. A Smoothing filter is applied to

all dwell time bases that are generated from above steps. The Gaussian smoothing filter was applied in GEANS to prevent sharp features and impose constraints on the local slope of the dwell time map. In addition, smoothing also prevents square-wave like dwell time solutions from grouping and dividing processes and provides more reasonable solutions. After all, the convolution between each dwell time basis and TIF forms the influence matrix ($\mathbf{t}$) from Section 2.1. Figure 2.2 illustrates the process of making influence matrix.

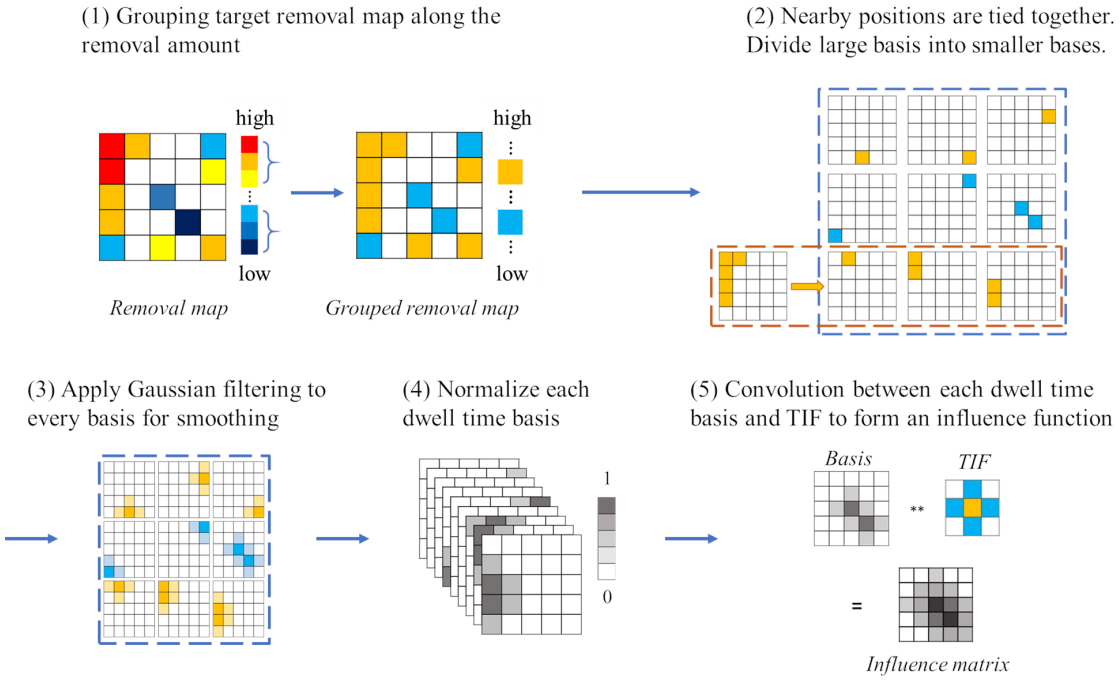


Figure 2.2 The flowchart of generating an influence matrix. Specific figures relate to each step, such as the number of groups at step will be optimized through GA. The detailed explanations are illustrated in Fig. 2.3 in the following section.

2.2.2 Optimization parameters to construct influence function matrix

By leveraging GA, optimal parameter sets can be found for the influence function matrix and GEANS to generate a dwell time map while reflecting optician's preference in solution.

To implement GA, the parameters to be optimized (genes) and solution space (gene pool) should be defined first. In the case of GEANS, the parameters related in making influence matrix, explained in Section 2.2.1, comprise genes. Then the gene pool is built within the range available to the machine to assure the feasibility of a dwell time map. The gene pool should be wide enough to not restrain a possible solution space too hard, but at the same time, should not be too wide for efficient optimization.

The dwell position of a tool is another essential parameter to be determined. Since the accessible dwell points are limited by tool size and motion, a smaller size tool is advantageous to edge-side fabrication of the workpiece in general. Therefore, in current simulation work, the coverage of the smallest tool is limited to edge-side only to find reasonable balance between total fabrication time and remaining surface error. The applied parameters are summarized in Fig. 2.3.

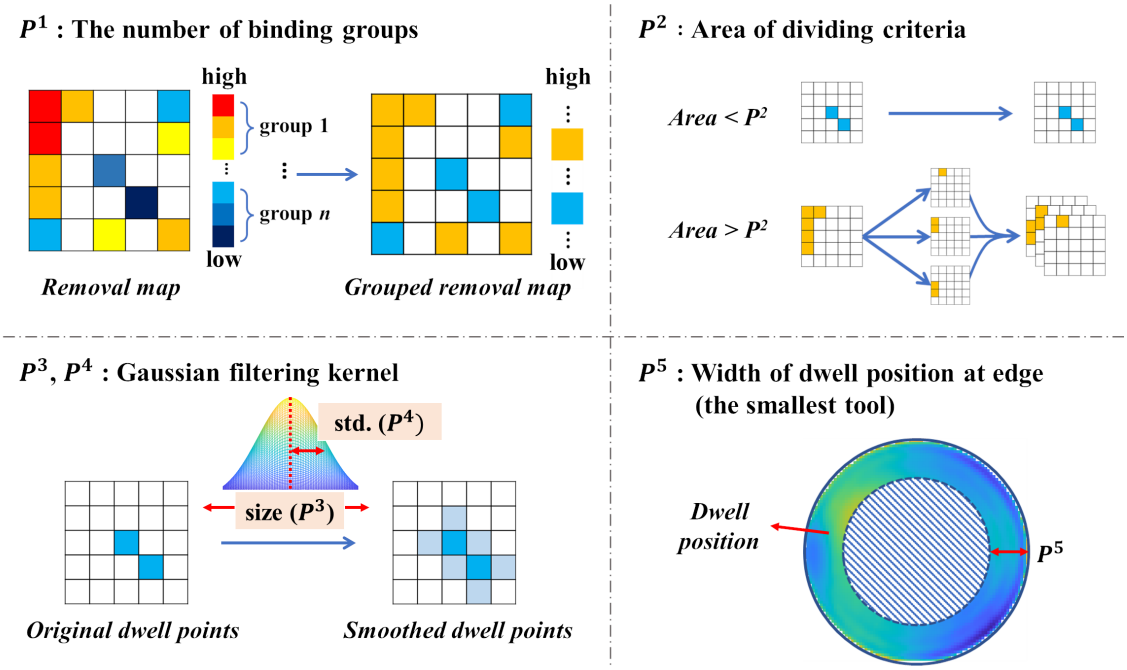


Figure 2.3 Parameters to be optimized through genetic algorithm. For GEANS, the number of optimization parameters is multiplied with the number of TIFs. Note that P^1 and P^2 are simulation-related parameters while P^3, P^4 and P^5 are tool-related parameters which are determined by machining capabilities.

2.2.3 Optimization and fitness function

Setting an appropriate fitness function is critical to lead the evolution of GA for our needs. The valid dwell time map in CCOS should duplicate the target removal map shape while achieving high figuring efficiency. Therefore, the performance of the dwell time map is evaluated with two indices: figuring efficiency and structural similarity.

Figuring Efficiency (FE) represents the accuracy of the algorithm for a given target removal map. The FE is defined as

$$FE(\mathbf{z}_d, \mathbf{z}_f) \equiv \frac{RMS[\mathbf{z}_d] - RMS[\mathbf{z}_f]}{RMS[\mathbf{z}_d]} \tag{2.6}$$

where RMS means Root Mean Squared value of each map. FE varies from 0 to 1, and a higher value means better figuring performance.

The Structural SIMilarity (SSIM) [47] is a quantified index to represent the visual similarity between two signals, μ_A and μ_B, by comparing luminance (l), contrast (c), and structural information (s). SSIM score varies from 0 to 1, and higher score means better similarity. The SSIM equation is represented as

$$SSIM(\mu_A, \mu_B) = l(\mu_A, \mu_B) \cdot c(\mu_A, \mu_B) \cdot s(\mu_A, \mu_B) \tag{2.7}$$

This index can be utilized to evaluate the validity of the dwell time map in CCOS since the valid dwell time map should closely copy the shape of the target removal map. In this work, SSIM index between the normalized target error map and dwell time map of a TIF as

$$S_k(\mathbf{z}_d^{norm}, \mathbf{d}_k^{norm}) \equiv SSIM(\mathbf{z}_d^{norm}, \mathbf{d}_k^{norm}) \tag{2.8}$$

where $\mathbf{z}_d^{norm}$ and $\mathbf{d}_k^{norm}$ represent normalized target error map and dwell time map of kth TIF.

With FE and S_k, we form the fitness function (Q) as

$$Q(FE, S_k) = \frac{FE + \sum_{k=1}^{l} w_k \cdot S_k}{1 + \sum_{k=1}^{l} w_k} \tag{2.9}$$

where w is relative weight of SSIM of each TIF case compared to FE. Note that the w has no general solution for the simulation, and can be changed based on the priority of the optimization result or machining capability.

The whole process of GEANS simulation is shown in the following Fig. 2.4.

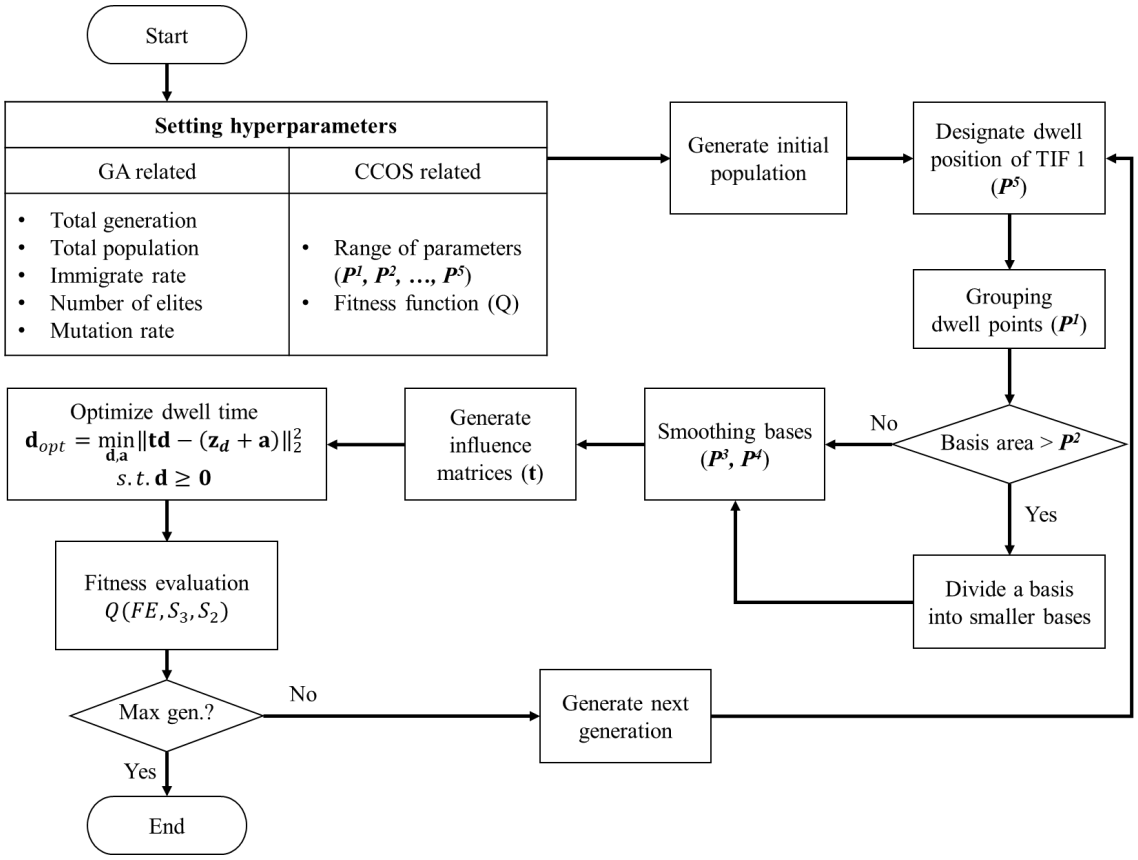


Figure 2.4 Flowchart of GEANS simulation.

2.3 Verification of GEANS through simulations

2.3.1 CCOS simulation setup

CCOS simulation was performed using actual measurement data of the target removal map (Fig. 2.5) and TIF data to verify the performance of GEANS compared to CNS. The target workpiece was a mirror, 4.25 m in diameter with an initial Root Mean Square (RMS) surface figure error of 0.749 μm. The target removal map was 341 by 341 pixels with a 12.5 mm pixel scale.

Three different TIFs were used for the simulation. The radius of orbital stroke TIFs [44] were 100 mm (TIF 1), 250 mm (TIF 2), and 400 mm (TIF 3) respectively. Due to the limited overhang ratio, TIF 2 and 3 were restricted to travel farther than 100 mm (8 pixels) from the edge.

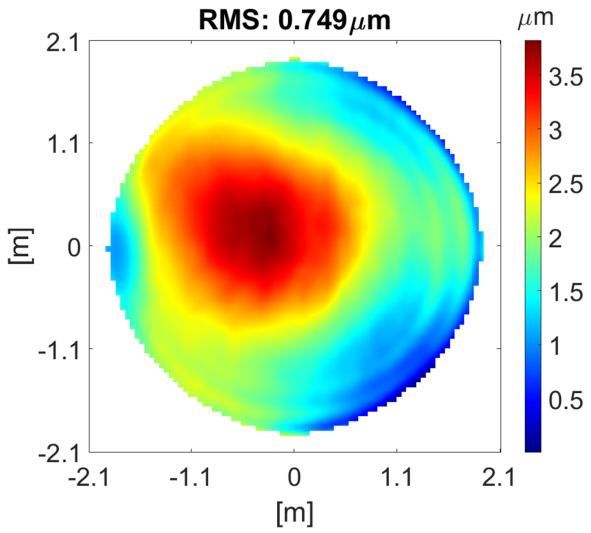


Figure 2.5 Target removal map for CCOS simulation. RMS of surface figure error is 0.749 μm.

Defining the proper range of parameters and hyperparameters are important to induce the desired result from GEANS. It is worthy to note that the used range of optimization parameters and hyperparameters can be varied upon the CCOS circumstances of users based on their target removal map, practical limitations (*e.g.*

maximum tool size and weight), available polishing resources (*e.g.* sufficient and stable polishing compound supply chain, available pitch types), or achievable machining specifications (*e.g.* maximum motor speed, gear wear). The specific values of hyperparameters were determined empirically in this work. For hyperparameters related to GA, the maximum generation number was set to 20, and each generation consists of 50 chromosomes. Among 50 chromosomes, 5 chromosomes were from the previous generation which scores high, 30 chromosomes were children that formed through crossover with a random multiplication rate of 0.3, and 15 chromosomes were new immigrants.

Domains of parameters illustrated in Chapter. 2.2.1 is another critical part to improve the performance of GEANS, yet the general solutions do not exist. In this simulation, the domains of each parameter was set empirically as well and summarized in Table 2.1.

Table 2.1 Ranges of parameters to be optimized through GA. These values are determined empirically. Numbers in brackets represent the range of each parameter. For example, [5:5:30] means [minimum : steps : maximum].

	TIF 1	TIF 2, 3
P^1 (px.)	[5:5:30]	
P^2 (px.^{2})	[1000:200:2000]	[20000:20000:120000]
P^3 (px.)	[13×13]:[4×4]:[29×29]	
P^4 (px.)	[1:1:4]	
P^5 (px.)	[5:5:30]	N.A

As the smallest TIF (TIF 1) is dedicated to edge area only, only SSIM index of TIF 2 and 3 were included in the fitness function. Although multiple TIF sizes will be optimized simultaneously in GEANS, the actual polishing runs will remain sequential (*e.g.,* from larger to smaller tool sizes). In this simulation, the SSIM of TIF 3 has higher weight than that of TIF 2 by assuming the TIF 3 will be applied earlier than TIF 2. The fitness function defined is

$$Q(FE, S_3, S_2) = \frac{FE \ + \ 5 \cdot S_3 + \ 2 \cdot S_2}{8} \tag{2.10}$$

The simulations were performed with MATLAB verison 2021a on a desktop equipped with AMD Ryzen 9 3950X (16 cores, 3.5 GHz) and 128 GB RAM.

2.3.2 Simulation results

2.3.2.1 Simulation result from CNS

The performance of CNS algorithm is set as baseline. In the simulation, the dwell points are equal to the sampling points, and the raster tool path is used while this can be any other tool path (*e.g.,* spiral) according to the actual machine's configuration. Note that the CCOS simulation conditions were mostly identical between CNS and GEANS except for the constraints of TIF 1 and the spatial resolution of data. Due to the high memory occupation, less sampled data that has half the spatial resolution (171 by 171) was used in CNS. The computing efficiency between algorithms is summarized at Table 2.2 in the following chapter.

Figure 2.6 shows the dwell time maps of each TIF and remaining error map after applied each dwell time map from CNS method. In this simulation, it is assumed that TIFs were applied sequentially from TIF 3 to TIF 1. The adjusted alignment amounts for CNS were $-0.86\ \mu m$ of piston, $6.57 \times 10^{-5} mrad$ in x-tilt and $-3.04 \times 10^{-4} mrad$ in y-tilt. The RMS of residual surface error (Fig. 2.6(f)) is about 15 nm which corresponds to 98 % of FE. Although CNS shows very high FE, the outcome dwell time maps have several point-like, disconnected spots (top row of Fig. 2.6). These dwell time maps are not preferred in actual CCOS running because the machine requires high acceleration and deceleration. It usually requires the post-processing to translate dwell time maps into affordable machine motion, and it induces the unexpected error on final outcome. Besides, the dwell time maps barely followed the shape of target removal map, so that the risk of inducing unexpected spatial frequency errors on residual surface is high. Therefore the results from CNS have limited potential for practical implementation.

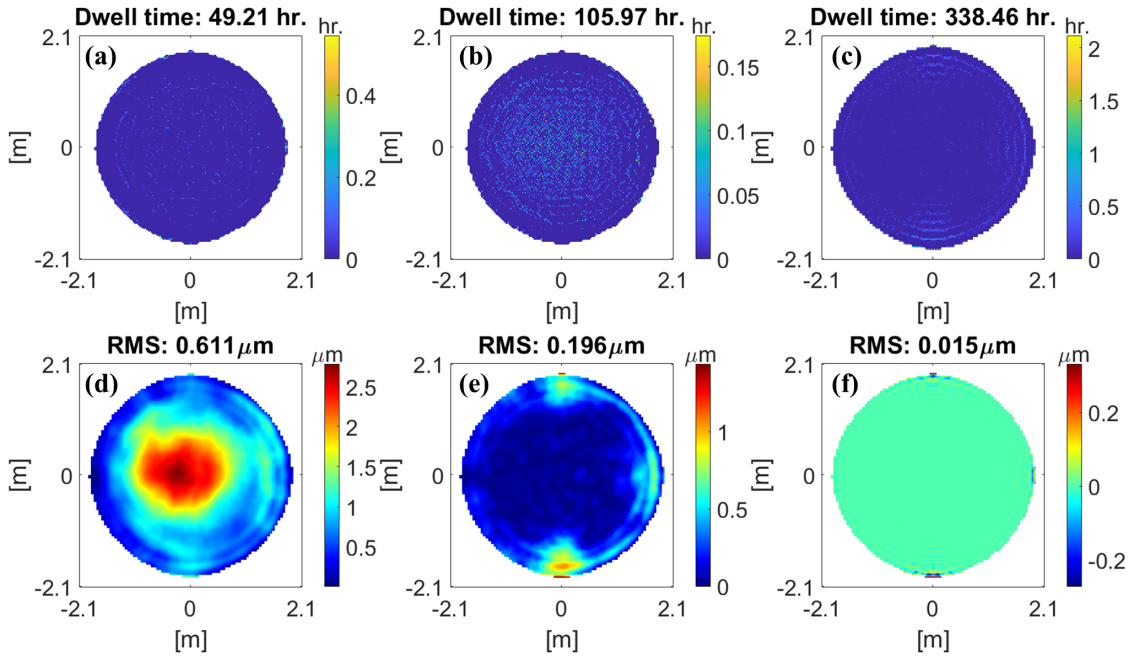


Figure 2.6 CNS results dwell time maps and residual error maps. Dwell time map of (a) TIF 3 (b) TIF 2 and (c) TIF 1. Surface error maps after applying (d) TIF 3 (e) TIF 2 and (f) TIF 1 sequentially. Residual surface figure error after CNS was about about 15 nm.

2.3.2.2 Simulation result from GEANS

Figure 2.7 shows the result of GEANS. Similar to CNS, the dwell points were equal to the sampling points. In GEANS, however, the smallest tool (TIF 1) only covers the area determined by $\boldsymbol{P^5}$ as illustrated at Section. 2.2.2, and the sampling interval is 12.5 mm which yields double resolution of CNS. After optimization the RMS of the residual surface error was 0.043 μm which corresponds to 94.3% of FE. Adjusted alignment amounts were -1.26 μm of piston, $-1.46 \times 10^{-6} mrad$ in x-tilt and $1.79 \times 10^{-5} mrad$ in y-tilt. Compared to CNS, the FE value was dropped 3.7 percentage points but still reasonably high FE. In terms of similarity of dwell time map, dwell time map of TIF 3 (Fig. 2.7(a)) and 2 (Fig. 2.7(b)) closely replicate the shape of target removal map (Fig. 2.5) as intended. The SSIM indices of each tool are 0.91 for TIF 3 and 0.85 for TIF 2.

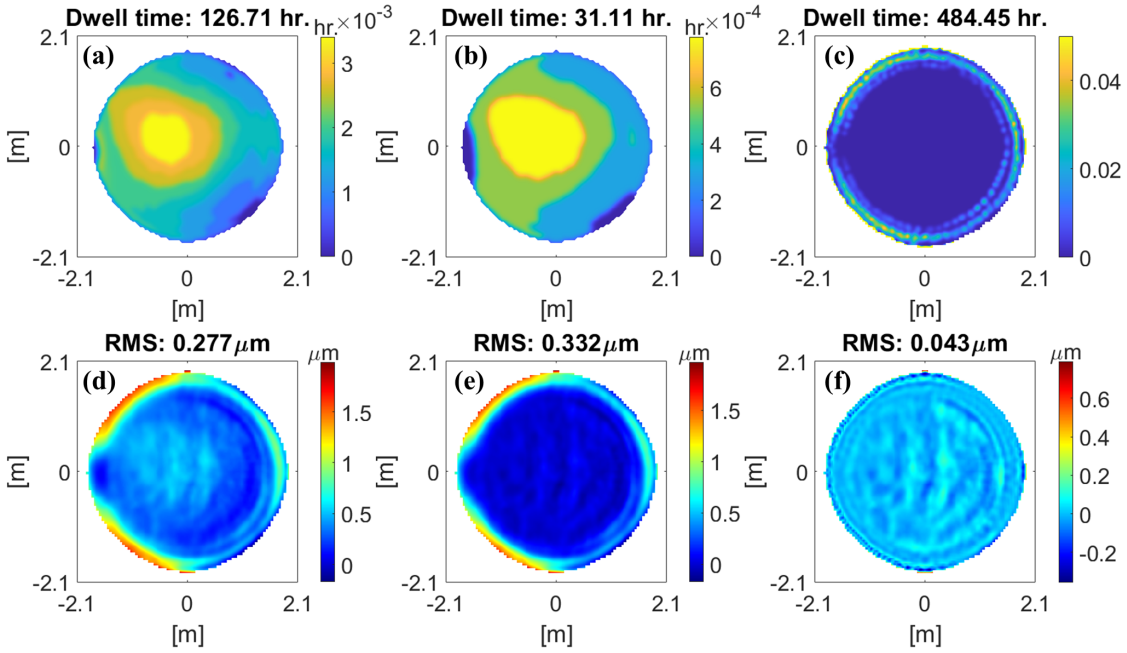


Figure 2.7 Resulted maps from GEANS. Dwell time maps of (a) TIF 3 (b) TIF 2 (c) TIF 1. Residual surface error maps after applying (d) TIF 3 (e) TIF 2 and (f) TIF 1 in sequentially. Residual error map of GEANS was 43 nm of RMS.

Figure 2.8 shows how the fitness function, RMS of residual surface error, and similarity of TIF 2 and 3 were changed over 20 generations. The RMS and similarity values were from the chromosome which has the highest score in that generation. Though the RMS of the residual map and both SSIM do not monotonically decrease or increase, the fitness function increases as the generations pass. The transformation of TIF 3 over generations is shown in Fig. 2.9.

2.3.3 Validation of GEANS

Compared to CNS, GEANS shows enhanced practicality of dwell time maps through three main features: building the influence matrix, smoothing dwell time maps, and employing SSIM index to make dwell time map to copy the shape of target removal map. In this chapter, the impact of these aspects are analyzed on GEANS's performance.

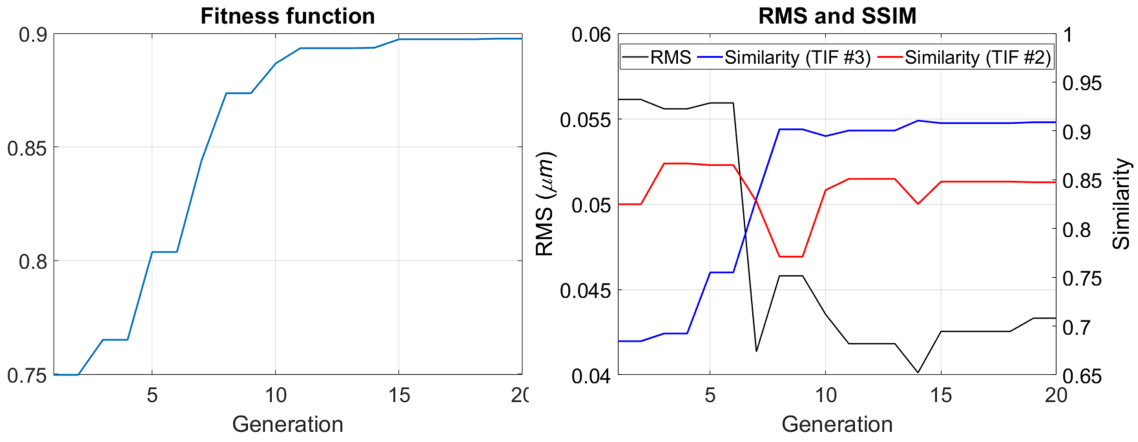


Figure 2.8 (Left) Fitness function value over 20 generations of evolving. (Right) RMS of remained surface error and S_2 and S_3 of each generations.

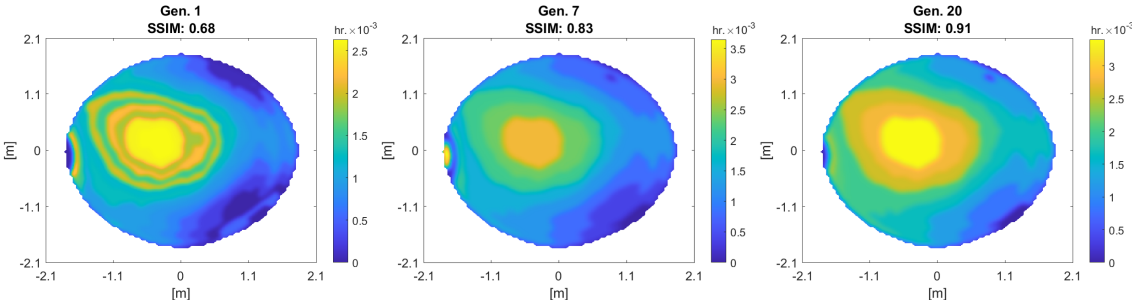


Figure 2.9 The transformation of TIF 3 over generation. From left to right, as the generation is passed, the overall shape of dwell time map gets similar to the shape of target removal map (Fig. 2.5).

Since GEANS utilized a GA that requires large number of repeated optimization calculations, improved computing efficiency was essential. By grouping and dividing, GEANS cuts down the size of elements of the influence function ($\mathbf{t}$) to more than 10 times smaller than CNS at the same resolution (Table 2.2) while maintaining enough degrees of freedom in optimization for figuring efficiency. As a result, GEANS shows 1000 times optimization speed increase for a single optimization on average. The total calculation time was shorter yet, as GEANS required 905 (50 times from the first generation, and 45 times from the rest generations) iterative optimizations. It

also enables us to use higher resolution data which benefits in large optics fabrication. Even with higher resolution, the size of influence matrix of GEANS is smaller so that the single computation took still less time than CNS.

Table 2.2 Computing speed comparison between GEANS and CNS.

Method	Map size [px.]	Size of $\mathbf{t_{m\times n}}$	$m \times n$	Computation [s]	FE [%]
GEANS	341 × 341	72641×3681	267,391,521	Single: 24.4 Total: 22,082	94.3
GEANS (Low samp.)	171 × 171	18317×3898	71,399,666	Single: 4.9 Total: 4,437	94.4
CNS (Low samp.)	171 × 171	18317×51423	941,915,091	5,131	98.0

Smoothing with Gaussian filtering also increased practicality of dwell time maps from GEANS. Figure 2.10 shows the resulted dwell time map of TIF 3 from GEANS when smoothing was applied (Fig. 2.10(a)) and was not (Fig. 2.10(b)). Without smoothing, the slope of dwell time change was abruptly between adjacent well points. Further the dwell time map was less similar ($S_3 = 0.59$) to the shape of target removal map than GEANS result ($S_3 = 0.91$).

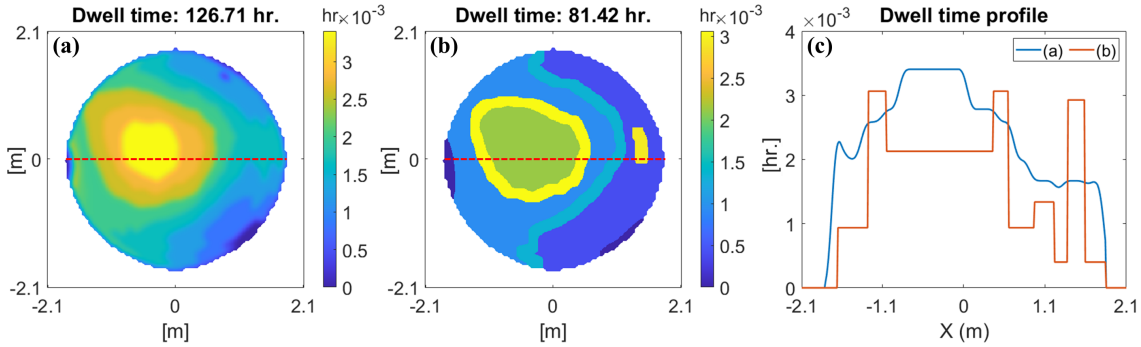


Figure 2.10 Comparison of dwell time map to show smoothing affects. Dwell time map of TIF 3 are shown here. (a) GEANS (b) GEANS without smoothing. (c) Center line profile (Red dotted lines in (a) and (b)) of each dwell time map.

SSIM also has an important role to produce desirable dwell time map in GEANS. Figure 2.11 shows the obtained dwell time maps of TIF 3 with and without SSIM

index in the fitness function. Without SSIM (Fig. 2.11(b)), dwell time map is not duplicating the target removal map noticeably. Besides, some dwell points were not linked together and slope of dwell time map is steep which causes inessential acceleration of tool (Fig. 2.11(c)).

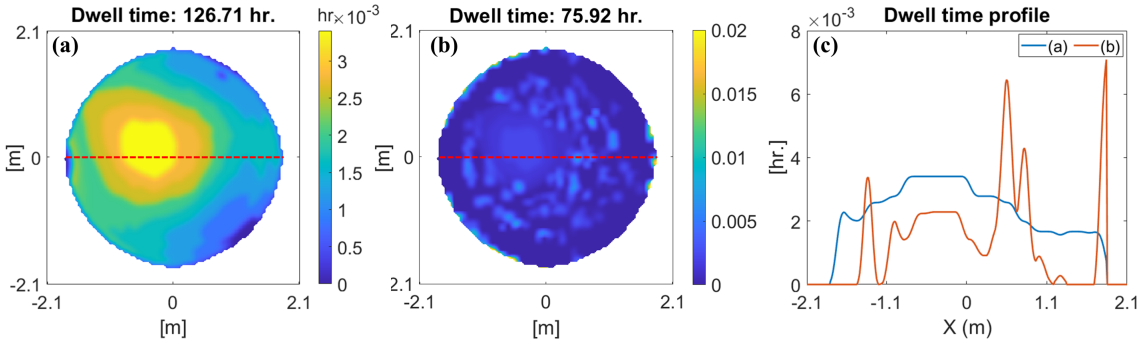


Figure 2.11 Dwell time maps of TIF 3 when SSIM was (a) considered and (b) not considered in fitness function. Without SSIM, the resulted dwell time map was neither copying the shape of target removal map and smoothly continuous. (c) Center line profile (Red dotted lines in (a) and (b)) of each dwell time map.

2.3.4 Error analysis of dwell time maps

Simulation results are degraded while applying in actual CCOS process due to various error sources which include tool positioning error, random variation in TIF, limited acceleration of tool, or laboratory environment. Considering these factors, the robustness test was performed to compare the stability and usability of dwell time maps from GEANS and CNS.

First, random errors were imposed to dwell position and TIF and checked how the Power Spectral Density (PSD) is changed. Both random error had rectangular distribution function of which boundary values were up to ± 10 mm for tool positioning errors and $\pm 10\%$ for TIF value errors. Within the boundary, random errors were added or subtracted from the original dwell time. Figure 2.12 shows the variation of PSD with perturbations. Without error (thick blue lines in the figure), the CNS method (Fig. 2.12 (b)) shows lower PSD in overall frequency than GEANS

(Fig. 2.12 (a)). However, with perturbations, PSD of CNS was changed and distributed broadly while PSD of GEANS was remained stable. These results implied that GEANS result is more predictable and robust against to the given errors so that more applicable than CNS in actual CCOS operation.

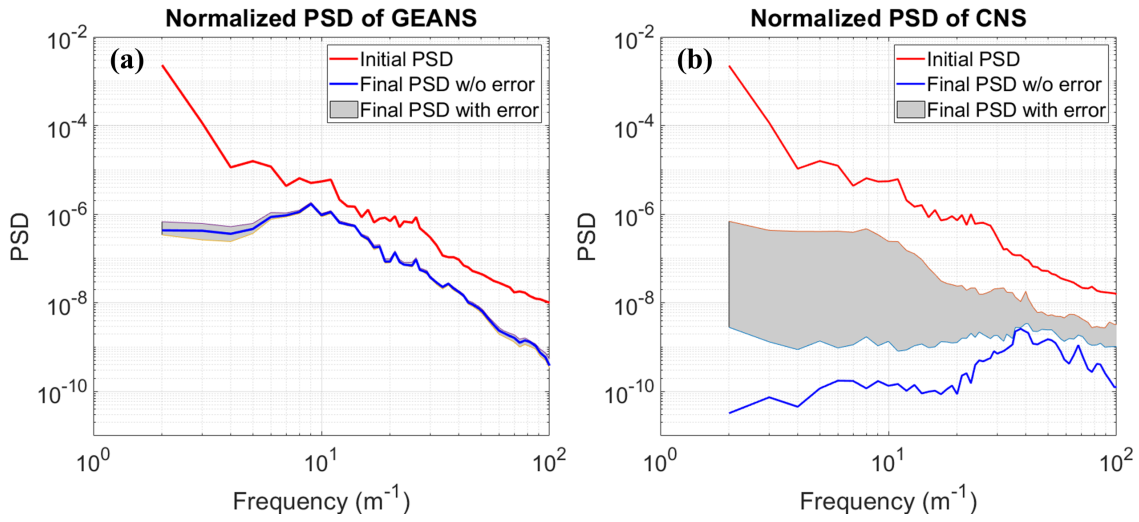


Figure 2.12 Compared PSD of remained surface error map after considering practical operation of (a) GEANS method and (b) CNS method. PSD of GEANS was remained steady while the PSD of CNS was worsened with perturbation.

Then applicability of dwell time maps from each method was evaluated. In actual CCOS running, since the maximum acceleration of tool is limited, dwell time maps that have smooth slopes along tool path are preferred and feasible solutions. Especially in large optics fabrication, as the sizes of tools are larger, controlling the tool acceleration is getting more difficult. Figure 2.13 is a histogram showing distribution of dwell time slopes of TIF 2 and TIF 3 from GEANS and CNS. As expected, slopes of CNS were higher than GEANS in general.

The impact of limited acceleration to the residual error map was also investigated. The continuous raster motion tool path was employed, and limits was set in dwell time difference along the path. If the difference is larger than the set limit, the dwell time limit is added or subtracted to an adjacent dwell point along the tool path until every difference is under the limit. Assuming the TIF 1 can have higher

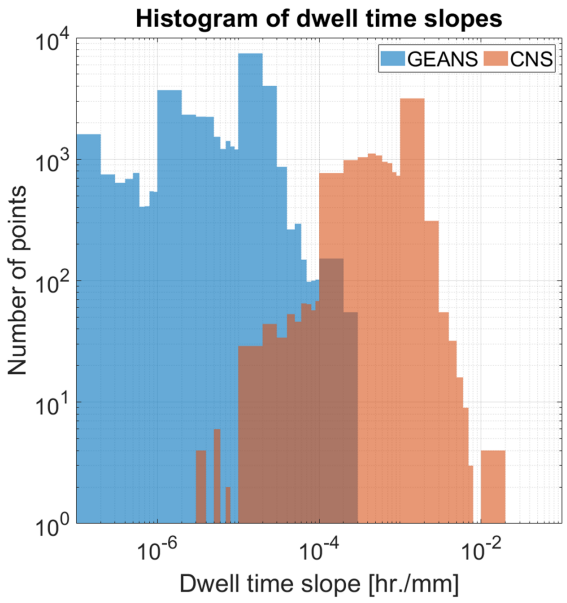


Figure 2.13 Histogram of dwell time slopes. X and Y axis are represented in log-scale. This different distribution in slopes of each method implies that the required maximum acceleration for GEANS is lower than CNS.

acceleration, this adjustment is applied to TIF 2 and 3.

Various slope limitations from 10^{-2} $mm/hour$ to 10^{-5} $mm/hour$ were applied. Figure 2.14 shows how the dwell time map of TIF 3 is changed when the maximum slope is limited to 0.001 $mm/hour$. In CNS, compared to the original map (Fig. 2.14(a)), dwell points with steep slopes were elongated and in consequence total dwell time was increased (Fig. 2.14(b)). GEANS, on the other hand, had no change in dwell time maps from the initial results since most of dwell points were already within the limit (Fig. 2.14(c), (d)).

The variation in dwell time maps, of course, affect to the final CCOS results as well. Figure 2.15 shows how the residual error map changed due to acceleration limitations. The FE of CNS was rapidly worsening because the dwell time maps could not be applied as optimized yet the results fron GEANS remained stable.

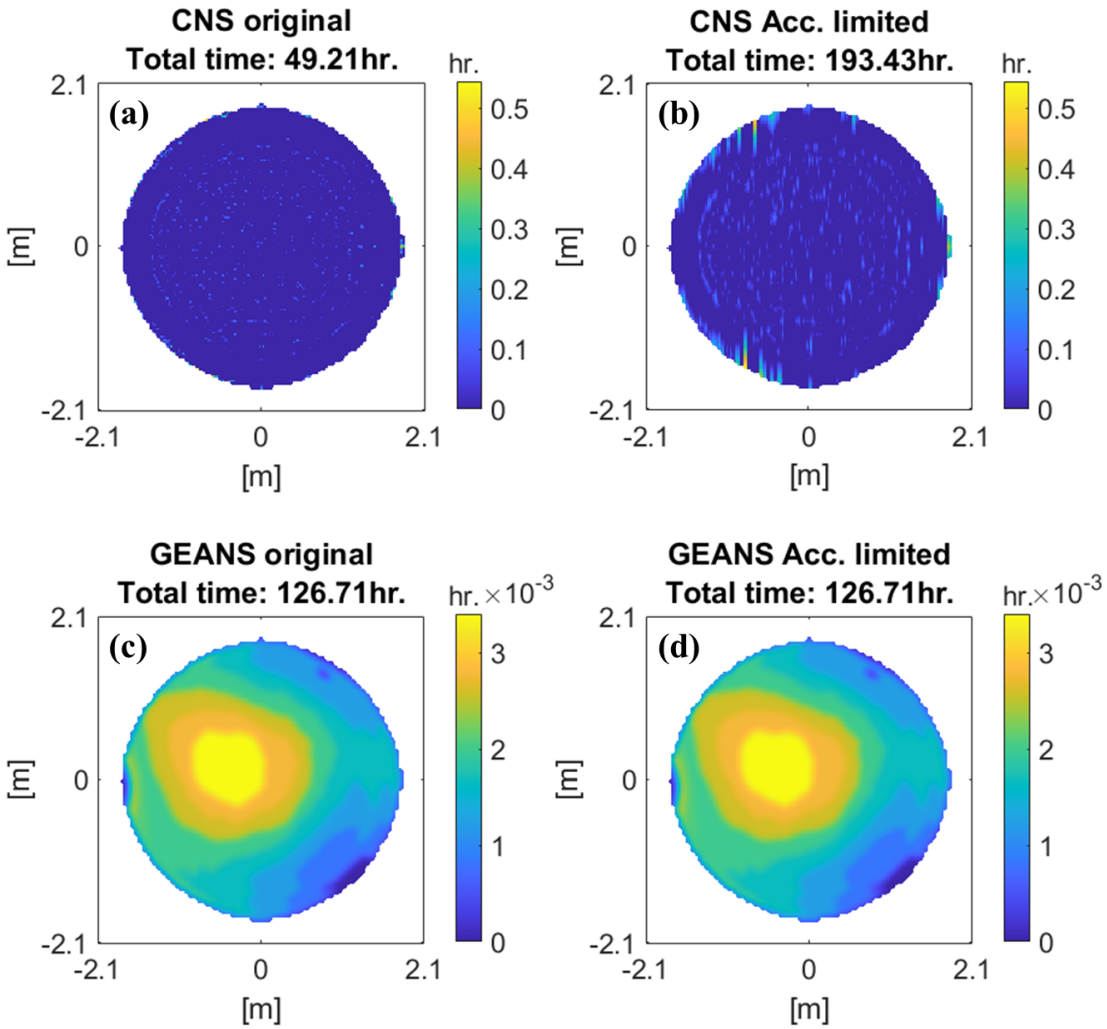


Figure 2.14 Variation of dwell time map when the acceleration limit (0.001 $mm/hour$) is applied. (a) Original dwell time map of TIF 3 from CNS and (b) Dwell points with high slopes were adjusted. As dwell time map was smoothed, total dwell time was extended as well. (c) Original dwell time map of TIF 3 from GEANS. (d) Slope limitation was applied but no difference in dwell time map.

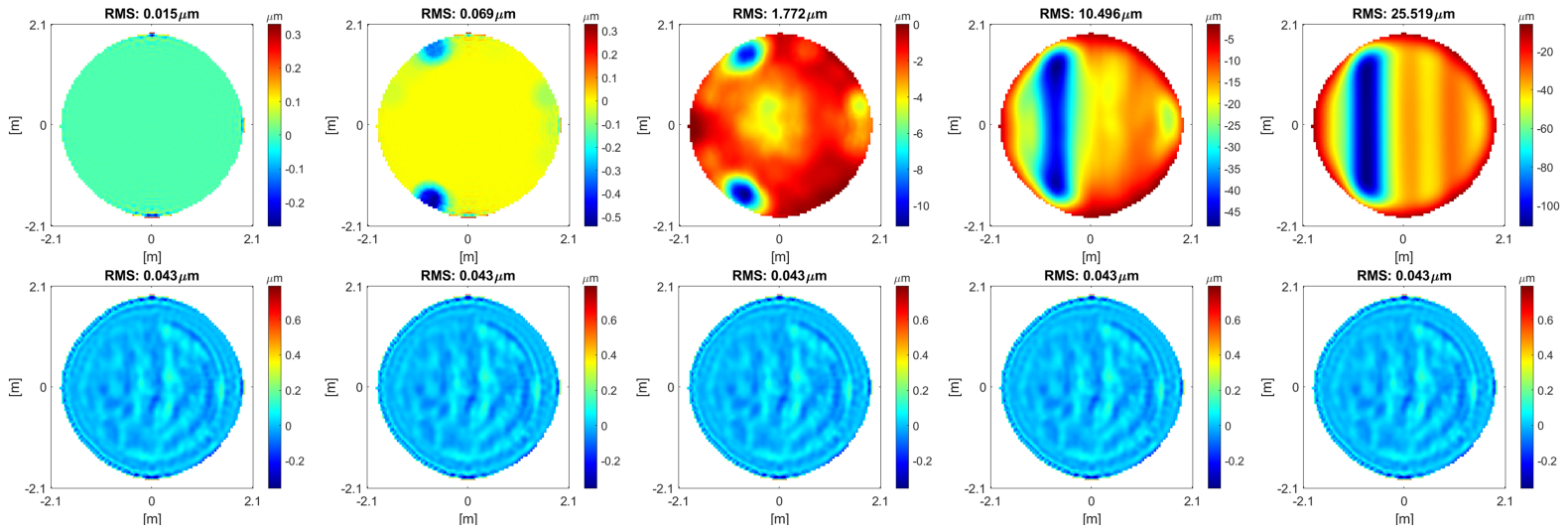


Figure 2.15 Changes of residual error map when the acceleration limit was applied. (top row) Results from CNS and (bottom row) Results from GEANS. Slope limitation value was varied from no limits (most left column) to 10^{-5} $mm/hour$ (most right column). The RMS residual is rapidly increasing in CNS while remains same in GEANS.

2.4 Discussion

The increased residual RMS and total dwell time in GEANS compared to CNS. It is also worth mentioning that, although CNS showed better initial results than GEANS in simulation, the results from CNS have limited potential for practical implementation. For example, the total dwell times of each CNS (Fig. 2.6) and GEANS (Fig. 2.7) were 494 hour and 642 hour respectively. Further, the residual RMS of CNS (0.015 μm) was lower than that of GEANS (0.043 μm). However, when we consider the limit in tool acceleration as shown in Figs. 2.14, 2.15, the total run time of CNS will be increased notably as well as the estimated residual RMS unless the CCOS machine can meet the rapid motion limit.

CHAPTER 3

Computational Vector Fiducial for Deflectometry System Alignment

This chapter is a summary of an article published at the journal *Optics Letters*, Appendix B and SPIE proceedings, Appendix C.

3.1 Computational vector fiducial pattern

The deflectometry ray-tracing simulator [48] provides coordinate relationships between the screen, UUT, and detector pixels (Fig. 3.1). Using the simulator, we can estimate the image at the camera with a specific screen pattern (Fig. 3.1(a), (b)), or control the illumination pattern and brightness on the screen to generate a specific camera image as we want.

This feature of the simulator is used to inversely generate the computational fiducial pattern to assist alignment of the deflectometry setup. The fiducial pattern is a specific pattern displayed on the screen that maps a grid dot image onto the camera detector(Fig. 3.1(c), (d)). Figure 3.2 is an example of how the fiducial pattern is utilized in alignment. The yellow circles are the locations of the fiducial for a perfectly-aligned system, the recorded white dots mark their observed locations, and the gray squares are equally distributed areas for each zonal analysis. Each dot is a 2D Gaussian shape to reduce the ambiguity in position determination. Since this pattern is calculated based on the model geometry parameters, any deviation from the fiducial points (Fig. 3.2(b)) implies an inconsistency in the geometry parameters between the model and the experimental setup. It is worthy to note that, if a surface shape error is in a way that produces the same vector fiducial changes as a misalignment, such fundamental degeneracy cannot be distinguished. The rectangular grid dot pattern is also preferable to utilize $\mathbf{G}$ and $\mathbf{C}$ polynomials sets that are introduced in the following chapters.

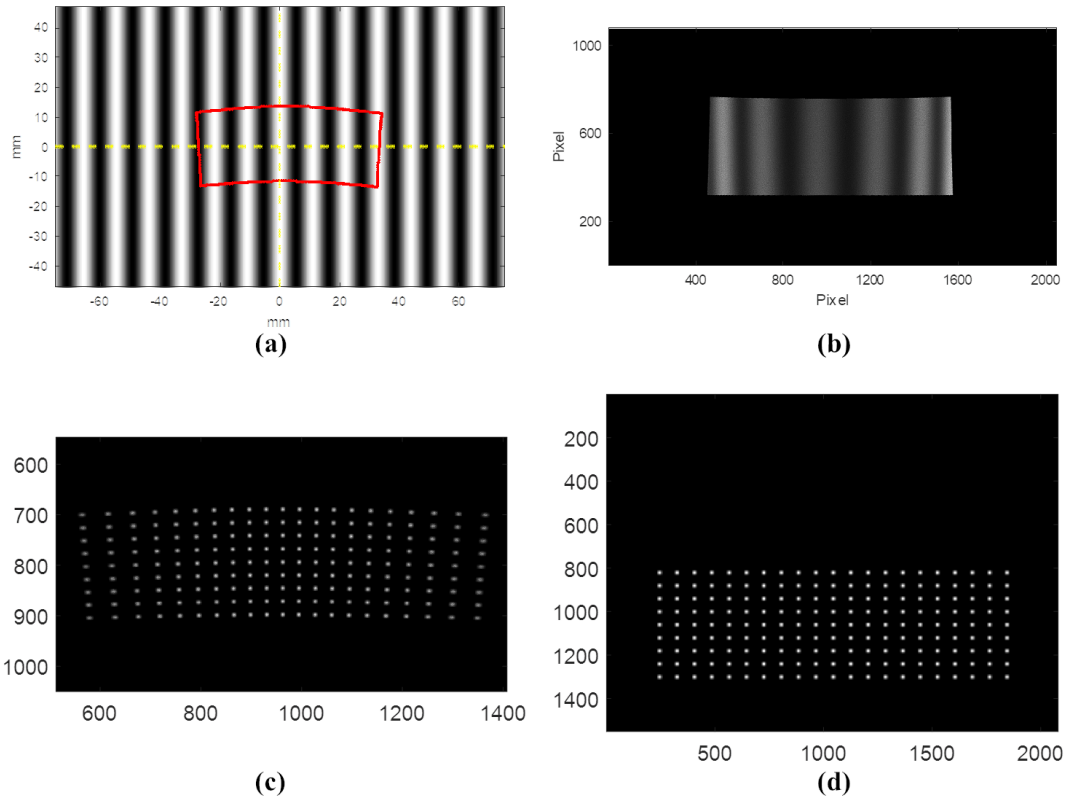
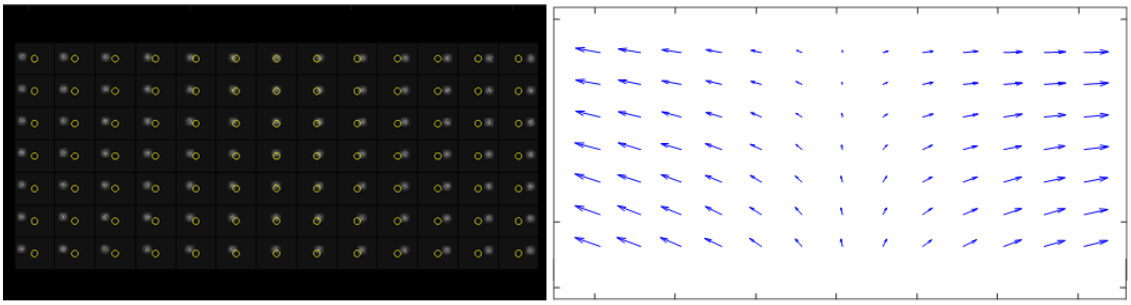


Figure 3.1 Example images from the deflectometry simulator. (a) A Sinusoidal pattern is displayed on the screen. The yellow line represents the center of the screen, and the red outline shows the corresponding region to shine the UUT. (b) Image of UUT at the conjugated camera detector plane. (c) Fiducial screen dot pattern to generate (d) regular grid dot onto the camera detector.

3.2 *G* and *C* polynomials

The fiducial dot pattern can be used to systematically quantify the misalignment status when it is associated with vector polynomials. As misalignments shift the image of the fiducial dots from their reference points, we can connect corresponding dots from their referenced position to their perturbed position to make vectors (Fig. 3.2(b)).

G and **C** polynomial sets are vector polynomials that are derived from the two-dimensional Chebyshev polynomials [31, 32]. The **G** polynomial set is derived from the gradients of the two-dimensional Chebyshev polynomials of the first kind, and **C**



(a) (b)

Figure 3.2 Simulated images for computational fiducial pattern application. (a) Observed image of the fiducial pattern at the detector plane. White dots are measured patterns, and yellow circles are fiducial from the model. (b) Vector map drawn from computational yellow circles to measured white dots, which are updated in real-time.

polynomial set is based on the curl of two-dimensional Chebyshev polynomials of the first kind. Since both **G** and **C** polynomials are orthogonal sets in the rectangular domain, specific vector terms can be directly related to system errors in alignment of the UUT. While **G** and **C** vector polynomials are utilized in this letter, the general computational vector fiducial method can be used with any other vector polynomials in order to be used for different UUT aperture shape applications (e.g., Zernike based vector polynomials defined over a circular domain).

3.3 Reverse optimization of *G* and *C* polynomial coefficients

The reverse optimization algorithm (Eq. 3.1) is widely used to align optical systems [49, 50].

$$\mathbf{A} = \mathbf{S}\Delta\mathbf{D},$$

$$\mathbf{A} = \begin{bmatrix} G_1 \dots G_i & C_1 \dots C_j \end{bmatrix}^T, \mathbf{S} = \begin{bmatrix} \frac{\delta G_1}{\delta x_1} & \dots & \frac{\delta G_1}{\delta x_n} \\ \vdots & \ddots & \vdots \\ \frac{\delta C_j}{\delta x_1} & \dots & \frac{\delta C_j}{\delta x_n} \end{bmatrix}, \Delta\mathbf{D} = \begin{bmatrix} \Delta x_1 \\ \vdots \\ \Delta x_n \end{bmatrix} = \begin{bmatrix} x_1 \\ \vdots \\ x_n \end{bmatrix} - \begin{bmatrix} x_1^o \\ \vdots \\ x_n^o \end{bmatrix} \tag{3.1}$$

This algorithm consists of three matrices which are as follows: (1) the measured **G** and **C** polynomials coefficients (**A**), (2) sensitivity (**S**), and (3) the amount of misalignment ($\Delta\mathbf{D}$) that displacement of each degree of freedom between current position (x) and target position (x^o). Sensitivity means how much the **G** and **C** polynomials coefficients are changed when the system is perturbed by a unit amount in each degree of freedom. The sensitivity can be determined through simulation or actual measurements at each location. After the sensitivity matrix is determined, the misalignment can be calculated using the least square fitting from the measured coefficients (Eq. 3.2).

$$\Delta\mathbf{D} = (\mathbf{S}^T\mathbf{S})^{-1}\mathbf{S}^T\mathbf{A} \tag{3.2}$$

This algorithm provides an accurate solution when the sensitivity is linear to the misalignment and the degrees of freedom are orthogonal to each other.

3.4 Verification of algorithm in freeform alignment

The performance of algorithm is verified through simulation and physical alignment experiment. First the sensitivity was investigated by moving the UUT by a known amount. Random misalignments were then imposed to the UUT's position, and vector data of the fiducial displacements were collected. The set of vector data was then fitted to the **G** and **C** polynomials, and the amount of misalignment was calculated through a reverse optimization process. These processes were repeated

until the criteria was met (Fig. 3.3).

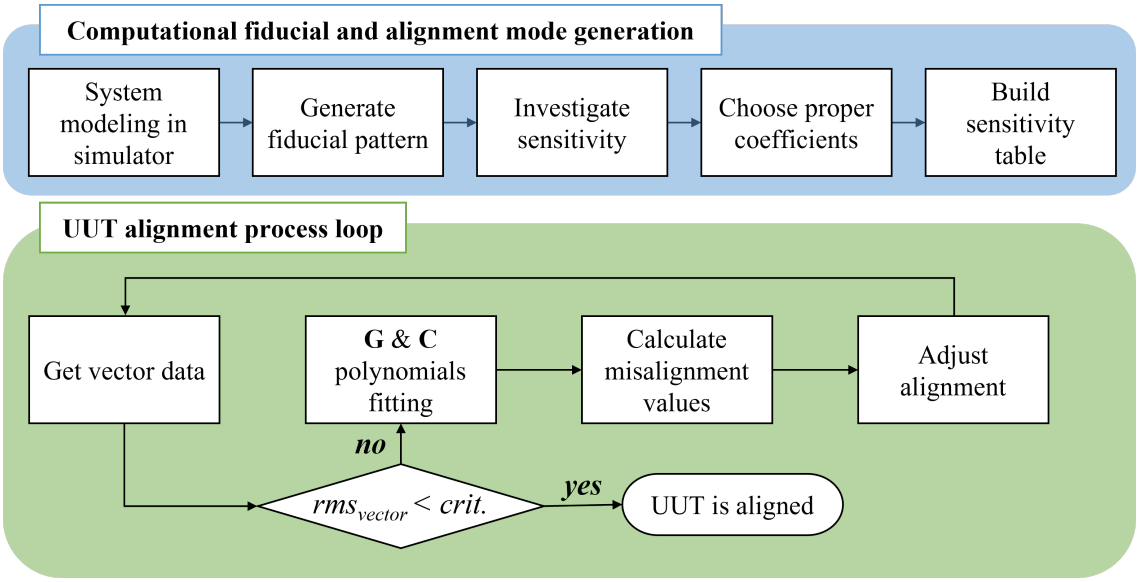


Figure 3.3 Flowchart of the computational fiducial-based alignment procedure for simulation and physical experiment.

3.4.1 Simulation

A freeform optic with 2.99 *mm* Peak-to-Valley (PV) aspheric departure within a rectangular aperture is used for the simulation study (Fig. 3.4). During the computational fiducial and its alignment mode generation process, the ideal deflectometry-and-UUT configuration is perturbed and misaligned in the simulation model.

A 27 × 20 grid of 540 dots were generated for vector sampling over the whole UUT aperture for the simulation. The investigated range of sensitivity was ±0.5 mm for translations and ±0.1° for tilts. The collected vector data is fitted to 100 terms of each **G** and **C** polynomials. Among the 100 coefficients, first 22 terms were selected from each **G** and **C** polynomial coefficients as the alignment modes, a total of 44 coefficients to build sensitivity matrix. To calculate the misalignment without degeneracy, each degree of freedom should have distinct sensitivities from one another. Hereafter translation in x, y, and z-axis are denoted as Dx, Dy, Dz for each, and tilt about x, y, and z-axis are denoted as Tx, Ty, Tz. In general,

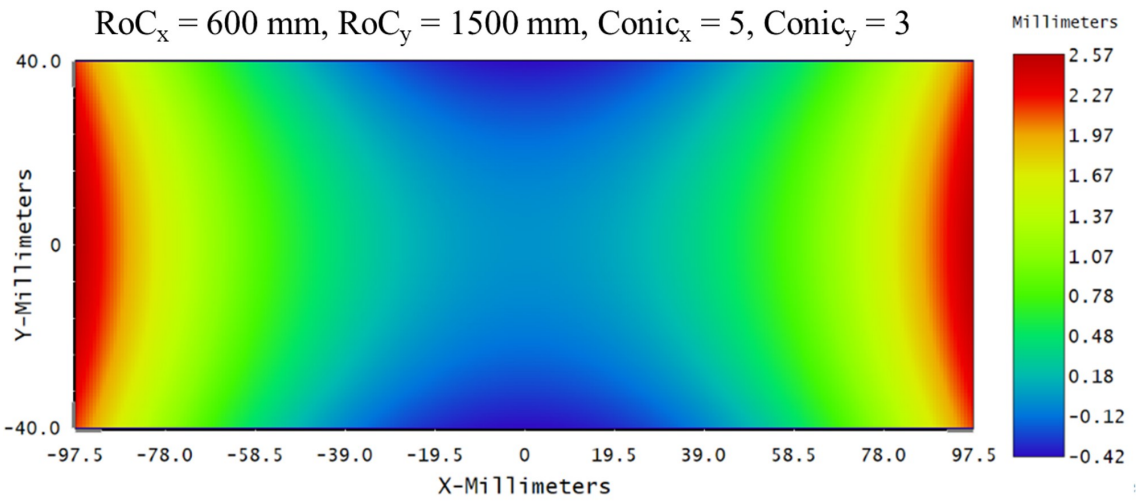


Figure 3.4 Surface map of sag departure from best-fit sphere for the simulation.

Dx-Ty and Dy-Tx are coupled motions that show similar tendency. Fig. 3.5 shows the normalized sensitivity ratio of some representative coefficients that have high sensitivities among the used 44 terms. Their sensitivities resembled each other but have different ratio between coefficients to be distinguished as a unique set of alignment mode fingerprints. Considering these characteristics of sensitivity matrix, it is expected that the misalignments would converge eventually in every degree of freedom with iterations (Fig. 3.3).

A total of 30 times alignment simulations were performed, and the random alignment error were imposed within sensitivity investigated range. The alignment end criteria was 0.08 pixel of RMS vector size (0.2 μm in this case) at the image plane. Simulation results are showed in Fig. 3.6. Although the required number of alignment steps were varied, the RMS vector sizes were converged and met the criteria at the end. The remaining amounts of misalignments were reasonably small in all 6 degrees of freedom. The remained error for Dy was relatively higher than others ($\sim$8 μm), but still within affordable range to have the consistence in surface measurements with deflectometry.

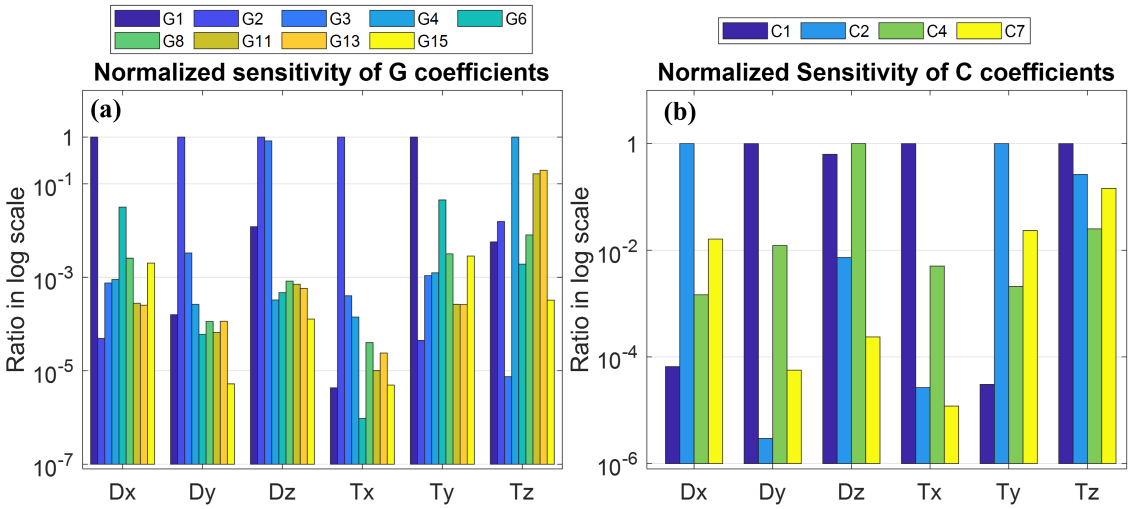


Figure 3.5 (a) Normalized sensitivity of **G** coefficients (b) Normalized sensitivity of **C** coefficients. Both graphs are represented in log scales due to small magnitudes of sensitivities.

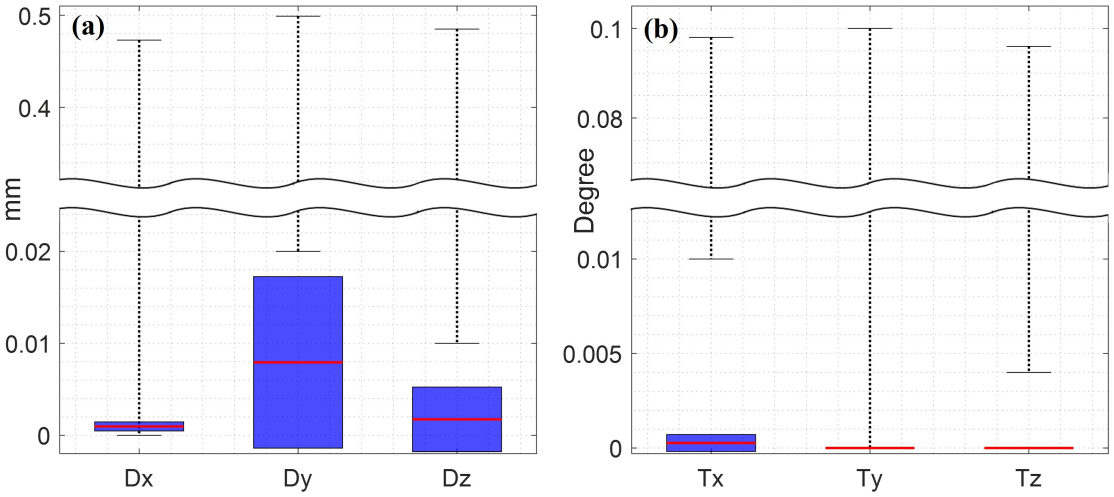


Figure 3.6 Result of alignment simulation. Dotted lines mean initial random alignment error range, red lines represent mean values of remained errors, and blue boxes represent standard deviations of each. (a) Translation errors (b) Tilt errors.

3.4.2 Physical experimental demonstration

Once the viability of the algorithm had been tested it was applied to an experimental deflectometry setup (Fig. 3.7). A 546 *mm* (22-inch) LCD monitor which has 1920 × 1080 resolution was utilized as the light source and a 3.2 MP camera with

16 mm focal length objective lens was mounted near the LCD monitor. The UUT used in the experiment was a freeform image projection mirror with rectangular aperture that has a width of 195 mm and a height of 80 mm.

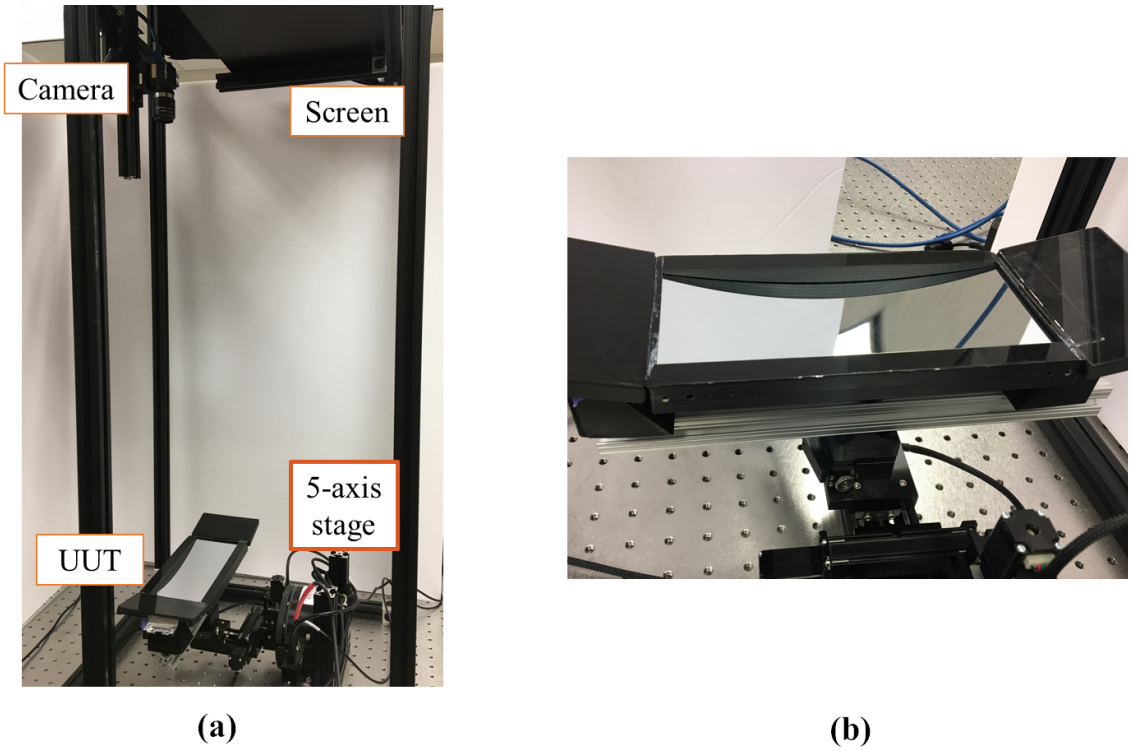


Figure 3.7 (a) Experimental setup of deflectometry. The light source (screen) emits rays that are reflected at the UUT and collected by the camera. (b) Zoom-in view of UUT mounted on the computer-controlled rigid-body motion stage.

To track the alignment status precisely, the UUT was mounted on a 5-axis motorized stage. (Note: The Tx was manually fixed due to the limited motorized hardware available in the lab.) The as-built vector fiducial alignment hardware system needs to be calibrated because the motion stage hardware, display, and camera are not ideal. It can be calibrated by aligning and measuring a reference UUT. Because the reference surface is known, after the alignment minimizing the surface residual error (i.e., difference between the measured and the known surface shape), the alignment state can be set as the nominal zero state and the residual error can be calibrated out as systematic error.

Similar to the simulation process, the sensitivity matrix was investigated first. In this case the UUT was translated ±0.5 mm along each axis, and tilted ±0.1° about the y and z-axis. Then the vector data were fit into 100 terms of each **G** and **C** polynomials. The total measuring time for **S** was about 20 minutes yet ∼90 % of the time was due to the series of image acquisition period limited by the as-built motorized stage speed. The sensitivity table was built using first 20 terms or more from each polynomial, and the alignment criteria was set to less than 0.3 pixel (0.75 μm) RMS for the vector size in detector plane. Then, the random misalignment were imposed within sensitivity investigated range and the algorithm was applied to calculate the amount of misalignment. These processes were controlled automatically and calculated repeatedly in closed-loop until alignment criteria was met. A commercial laptop (CPU: i5-1135G7 / RAM: 8 GB) was used for calculating and controlling the system and each iteration took less than 2 minutes.

A total of 10 alignment experiments were performed, and results are summarized in Fig. 3.8. The RMS vector size met the criteria, but the remaining amounts of misalignments were various for each degree of freedoms. Dy, Dz, and Tz converged well while Dx and Ty converged as well but had relatively large amounts of error remaining. This is because the Dx and Ty give the similar fiducial motion and hard to distinguish in vector space.

Alignment in most metrology systems is important so that misalignment is not embedded into surface measurements. The alignment results were validated by comparing the PV of the subtracted map between reference surface map against before/after aligned surface map. The reference is the surface map that is measured at home position. Thus the difference map shows both the capability of alignment loop to bring back the UUT to original position and repeatability of optical testing. The PV surface map error due to the residual misalignment is less than 8.4 μm from 10 times of experiments (Fig. 3.9). The result demonstrated that the proposed computational alignment algorithm can guide deflectometry system alignment to secure repeatability in optical testing without additional alignment devices. This is the deflectometry counterpart of the alignment mode of interferometry.

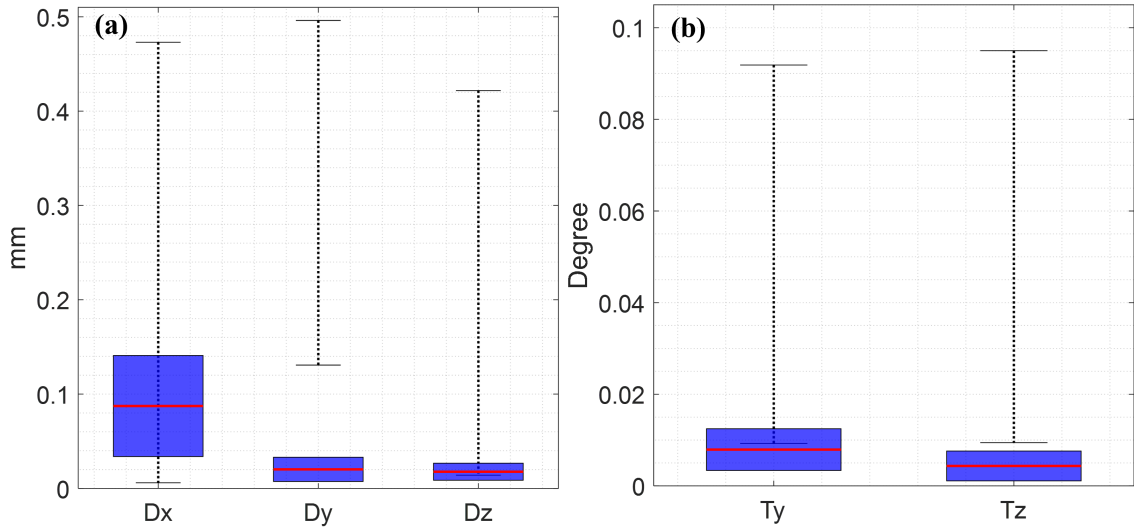


Figure 3.8 Result of physical experiments. (a) Translation errors (b) Tilt errors.

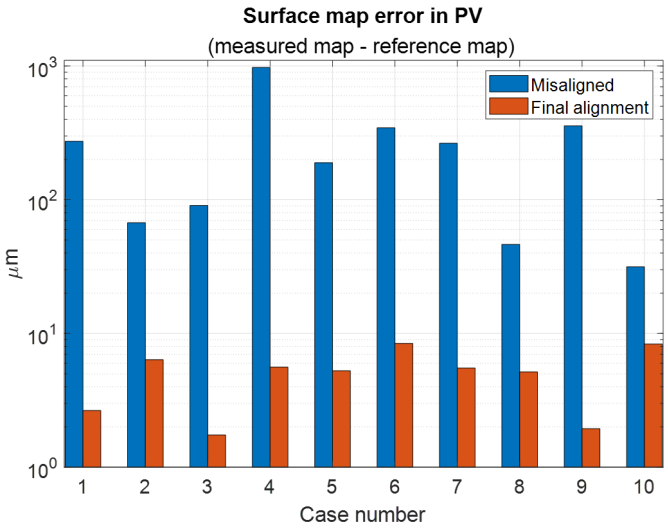


Figure 3.9 Improvement of surface map matching via alignment loop.

3.5 Discussion

The algorithm introduced in this work is a self-calibration method that uses vector fiducials from a single field of view. It is worth noting that the performance of the alignment status estimation was limited by the accuracy of hardware, not the algorithm itself as long as the misalignment is within a linear range of the sensitivity.

Indeed, the coupled translation and tilt are already predicted from the simulation stage. Fig. 3.10 shows the simulated vector fiducial image of Dx and Ty. Their difference is very small but still distinguishable with high order coefficients as shown in Fig.3.5. For this reason, the accuracy of the algorithm can be improved by obtaining more precise vector data (*i.e.,* higher repeatability data) or utilizing a higher resolution camera in a deflectometry system.

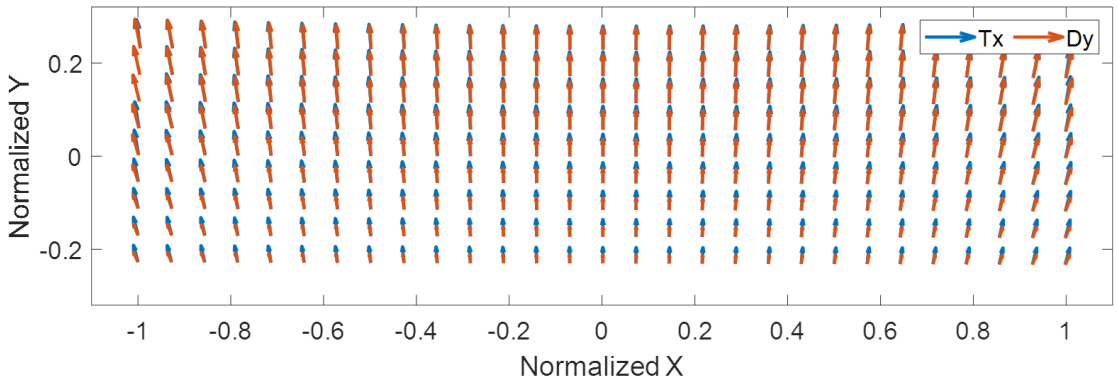


Figure 3.10 Similar vector behaviors between Dy and Tx.

For an application of a large misalignment case in that misalignments are non-linear, an adaptive or iteratively updating **S** throughout the alignment process can be applied. If then, updating **S** comes at the cost of modeling or measurement time.

There is also a fundamental limitation in the alignment algorithm. The fiducial can be disturbed by not only misalignment but surface error or any other mismatches between the simulated model and actual setup. The degeneracy between some surface shape errors (*i.e.,* tip and tilt) and alignment errors cannot be resolved because they have the same effect on camera images. As this is a common issue in alignment algorithms, overcoming such degeneracy will be a great future study topic.

CHAPTER 4

MOBIUS: A Modular Plug-in Spectrograph Enabling Cross-Dispersion for Large Binocular Telescope

This chapter is a summary of an article submitted to the *Journal of Astronomical Telescopes, Instruments, and Systems*, Appendix D and SPIE proceedings, Appendix E.

4.1 Design of MOBIUS

4.1.1 Concepts

The main objective of MOBIUS (Mask-Oriented Breadboard Implementation for Unscrambling Spectra) is a plug-in extension module of LUCI (LBT Utility Camera in the Infrared) to provide full wavelength coverage in a single unit subject to scientific objectives. For that purpose, the MOBIUS-equipped frame will be stored and handled by the MOS (Multi-Object Spectroscopy) unit. [51] Thus, MOBIUS can be placed in the focal plane of the LBT and removed on demand easily (Fig. 4.1). MOBIUS is also required to minimize the impact on the image quality at the LUCI detector plane while providing cross-dispersion in LUCI. This indicates that the optical properties of the incident beam from LBT (*i.e.,* f-number, chief ray angle, focal plane position) should be kept after the MOBIUS module is inserted. Lastly, MOBIUS consists of two identical cross-disperser modules symmetrically side by side in a single mask frame to offer sky-subtraction by dithering between source and sky positions.

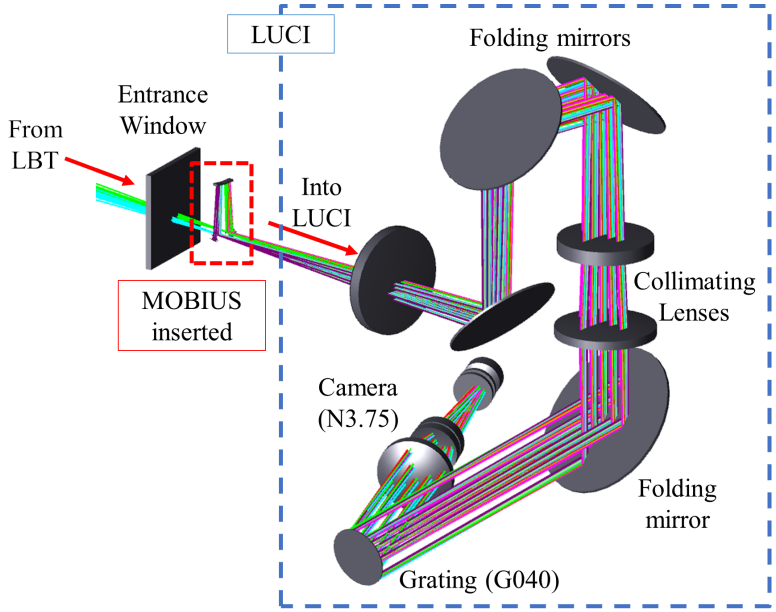


Figure 4.1 The optical layout shows how MOBIUS works with LUCI. The MOBIUS-installed frame will be placed at the focal plane of LBT by substituting the traditional slit mask frame. With MOBIUS, LUCI is able to observe zJHK spectra in a single exposure without mixing between wavelength bands without additional modification in instrument settings.

Littrow type of spectrographs[52, 53] is perfectly fit to concepts of MOBIUS. With a mirror-coated rear surface, Littrow prism configurations utilize a double pass that enables increased dispersion in a compact form and returns dispersed rays to near the original slit position.

The schematic concept of MOBIUS is shown in Fig. 4.2. The triangle shape pick-off mirror is located right before the focal plane of LBT to deflect the incident beam towards into the space in the mask frame, and a slit will be installed right after the pick-off mirror (Fig. 4.2(a)). The beam is then collimated through a spherical mirror and enters the Littrow prism which provides retro-reflection and dispersion. After reflection, the dispersed beam hits the spherical mirror again and is imaged on the other side of the pick-off mirror to advance to LUCI (Fig. 4.2(b)). Since the dispersed beams are still within the field of view of LUCI, there would be no vignetting as long as the ray angle and focal planes have remained unchanged from

the original LBT beam. As the beam is dispersed at the focal plane of LBT to the perpendicular direction of LUCI's dispersion, MOBIUS broadens the wavelength coverage of a single LUCI with no modification in the instrument setting.

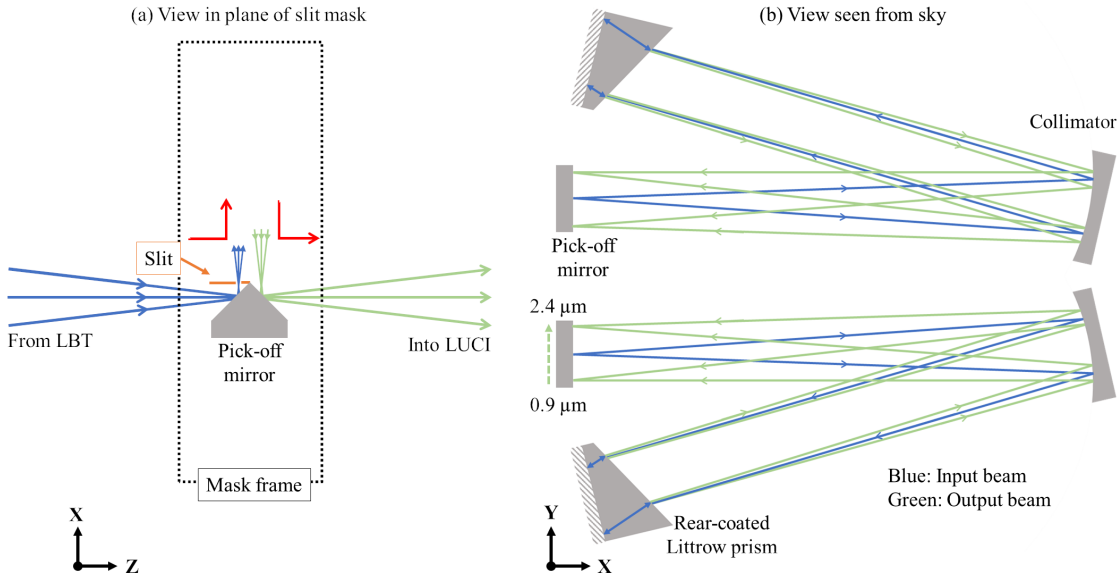


Figure 4.2 Schematic figure of MOBIUS. (a) The pick-off mirror is placed near the focal point of LBT to deflect the input beam path (blue lines) into the plane of the mask frame. The beam is focused right after the reflection at the entrance surface of the pick-off mirror. (b) Inside of the frame mask, the beam is collimated and dispersed (green lines). The beam is reflected from the rear surface of the prism, then focused near the original focal point with shorter wavelength is located close to the prism. This process produces the cross-dispersion before the higher dispersion grating in LUCI. MOBIUS consists of two identical spectrographs to offer sky-subtraction by dithering between target and sky position.

4.1.2 Design boundary conditions

The modular plug-in concept utilizes an existing feasture of LUCI (*i.e.* MOS unit[51]) to handle the MOBIUS-equipped make frame. Thus, the hardware boundary conditions are given from the capabilities of the MOS unit. Firstly, every optical and mechanical component needs to be packed within the slit mask frame space ($150\ mm \times 150\ mm \times 12\ mm$). Further, the extra weight of the MOBIUS system

should be kept within 20 grams of a standard MOS mask to be operated safely.

MOBIUS should provide a large enough dispersion distance to prevent overlapping between diffraction order spectra at the LUCI detector while securing the minimum slit length, 2 arcsecond, for scientific objectives. As the current MOBIUS design is optimized for the N3.75 camera and G040 grating[54], 2 arcsecond of slit length corresponds to the 1.2 mm of dispersion distance at the LBT focal plane. Considering the margin between spectra at the detector, target minimum dispersion distance between the central wavelength of each order was set as 1.5 mm at the exit surface of pick-off mirror.

4.1.3 Design process

MOBIUS consists of three optical components: a pick-off mirror, a spherical mirror as collimator, and a Littrow dispersing prism which has a mirror-coated rear surface. The specific parameters of each component are determined considering dispersion distance, maximum beam footprint size, and the best focal region of LBT.

The shape of the pick-off mirror is a right-angle prism, yet the outer surfaces are employed for reflection (Fig. 4.4(a)). Since the dispersed beam is retro-reflected, the input and output beams are nearly parallel to each other. So the apex angle of the pick-off mirror is designed 90° to preserve the ray angles before and after the MOBIUS. The location of the pick-off mirror inside of slit mask frame is determined by the best focal region of LBT (± 1.25 arcminutes in dispersion direction of LUCI which is perpendicular to the dispersion direction of MOBIUS) [51] as well as the focal length of the collimating mirror.

For the collimating mirror (Fig. 4.4(b)), although an Off-Axis Parabolic mirror (OAP) is commonly used, a spherical mirror was chosen because it made negligible aberration on the focused, slow f/15 beam from the telescope. The spherical mirror is advantageous in fabrication and alignment as well. The focal length of a spherical mirror is directly related to the dispersion distance since the longer focal length produces greater dispersion. The radius of curvature of the spherical mirror was set as 180 mm in MOBIUS. As a consequence, some margin at the clear aperture of

spherical mirror while extending slit length for scientific objectives.

The Littrow dispersing prism (Fig. 4.4(c)) is made of Strontium Titanate ($SrTiO_3$, $n = 2.28$ at $\lambda = 1.65\ \mu m$) which is transmissive and highly dispersive at the operating wavelengths and temperature [55, 56]. The apex angle of the prism determines dispersion distance primarily. To calculate the dispersion distance between two wavelengths, it is required to determine the deviation angle difference first. In the Littrow prism (Fig. 4.3), the apex angle (α) is equal to the refractive angle to make the refractive ray is reflected as normal to the rear surface. So the incident angle θ_i is determined as

$$\theta_i = \sin^{-1}(n_a \sin\alpha) \tag{4.1}$$

where n_a is refractive index of wavelength λ_a. Assumed that the base wavelength is λ_a, the refracted angle (θ_b) of wavelength λ_b inside of prism is

$$\theta_b = \sin^{-1}(\frac{n_a}{n_b} \sin\alpha) \tag{4.2}$$

Now, the beam is reflected from the rear surface, and resulted refracted angle from the prism (θ'_b) is

$$\theta'_b = \sin^{-1}[n_b \sin(2\theta_b - \alpha)] \tag{4.3}$$

Thus, deviation of λ_b when the base wavelength is λ_a ($\delta_{a,b}$) is

$$\begin{aligned} \delta_{a,b} &= \theta'_b - \theta_i \\ &= \theta'_b - \sin^{-1}(n_a \sin\alpha) \end{aligned} \tag{4.4}$$

Therefore the dispersion distance ($\Delta d_{a,b}$) is

$$\Delta d_{a,b} = f \tan(\delta_{a,b}) \tag{4.5}$$

where f represents the focal length of the spherical mirror.

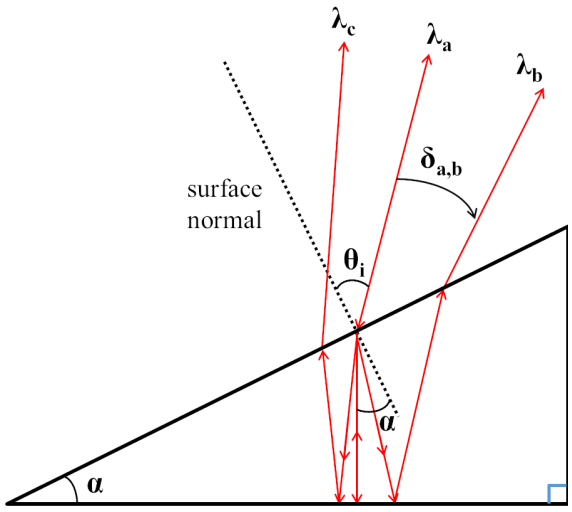
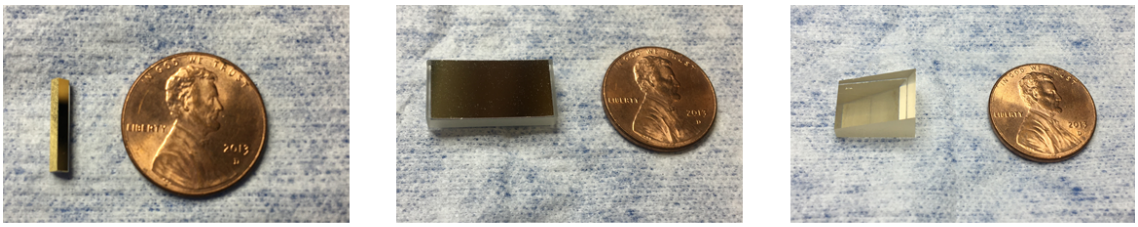


Figure 4.3 Ray diagram of Littrow prism. The apex angle (α) of prism should be equal to the refractive angle to make retro-reflection.

MOBIUS is required to separate four NIR bands corresponding to the orders of G040 grating in LUCI. The central wavelength (λ_c) of each band is 0.97 μm (z), 1.25 μm (J), 1.65 μm (H), and 2.2 μm (K)[54]. The apex angle of prism was derived to make minimum dispersion requirement between J-band and H-band since their refractive indices show the least difference. Above condition and Eq. 4.5 lead the apex angle was set as 19°. Also, the derived incident angle is 48° and the dispersion distance between the J and H band is 1.65 mm at the focal plane of the LBT which meets our requirement.



(a) (b) (c)

Figure 4.4 Manufactured optical components of MOBIUS. (a) The pick-off mirror is made of Zerodur and gold coated. Clear aperture is 12 mm by 2 mm. (b) The spherical mirror is made of Zerodur and aluminum-coated. Clear aperture is 17.5 mm by 9 mm. (c) Littrow prism with silver-coated on rear surface. The entrance surface has about 13 mm by 8 mm of clear aperture.

The optical design of a unit of MOBIUS is shown in Fig. 4.5(a) and the overall layout with optical components mounted in a slit mask frame is in Fig. 4.5(b). The light-weighted features are implemented on the frame to meet the safe weight requirement (total frame weight of 326 grams with 20 grams of additional weight) of the MOS unit. Alignment screws were also added in the MOBIUS module for fine adjustment.

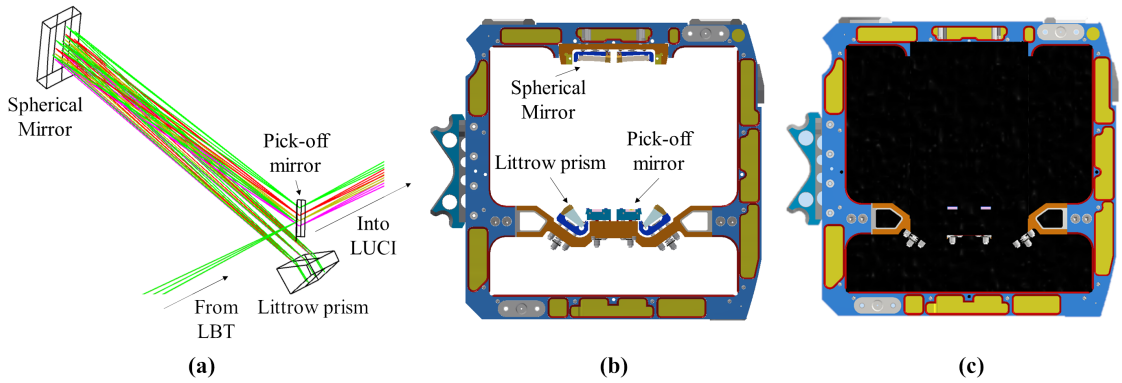


Figure 4.5 (a) Optical layouts of a unit of MOBIUS. (b) The layout of MOBIUS mounted slit mask frame with alignment features. The frame was light-weighted to meet the weight limit of MOBIUS. Two identical spectrographs are located in plane symmetry and the slits are placed as close as possible for the sky subtraction by dithering. (c) MOBIUS with mask (black color). The mask blocks empty space of frame except the entrance to MOBIUS.

Main concerns of MOBIUS is vignetting as the optical performance is kept good enough as long as the beam is not vignetted. A sensitivity analysis was performed to figure out the alignment tolerance of each optical component. Z-axis is defined along with beam path of LBT, and Y-axis is the direction of dispersion from MOBIUS. Table. 4.1 shows the tolerance results of MOBIUS. Translation in x, y, and z-axis are denoted as Dx, Dy, Dz for each, and tilt about x, y, and z-axis are denoted as Tx, Ty, Tz. As the entrance slit is coupled together, the X, Y, Z coordinate of the pick-off mirror is set as reference. Tolerances of Tz of pick-off mirror, Tx of spherical mirror and prism are not specified as they have minor effects only. Overall alignment tolerance is quite generous while the apex angle of the pick-off mirror is the most sensitive factor for vignetting. The tolerable range of apex angle of the pick-off mirror (α) is from -2.27 $mrad$ to 0.7 $mrad$ from the designed value, 90°.

Table 4.1 Tolerance results for alignment of each component and apex angle of the pick-off mirror.

	Dx (mm)	Dy (mm)	Dz (mm)	Tx (mrad)	Ty (mrad)	Tz (mrad)
Pick-off mirror	-	-	-	1.4	1.7	-
Spherical mirror	0.2	0.2	0.3	-	1.4	1.13
Prism	0.5	0.5	0.5	-	1.7	1.7
Apex angle of pick-off mirror	$89.87^\circ \leq \alpha \leq 90.04^\circ$					

4.2 Performance analysis

4.2.1 Designed performance

The footprint diagram of LUCI and LUCI with MOBIUS are shown in Fig. 4.6. In LUCI alone, (Fig. 4.6(a)), all the spectra are overlapped in a line so that the filter is essential to distinguish different bands. On the other hand, as MOBIUS generates perpendicular dispersion to LUCI, each spectrum is separated and distinguishable regardless of filters (Fig. 4.6(b)). In the current design configuration with N3.75 camera and G040 grating, MOBIUS can utilize a slit length up to 2.3 arcsecond without mixing different wavelength bands.

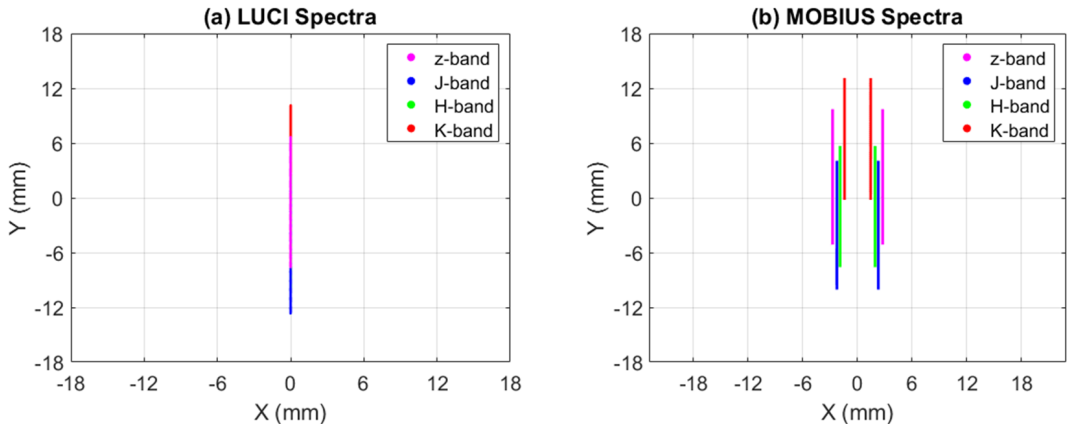


Figure 4.6 Spectra results at the LUCI detector. (a) When observing using LUCI and (b) LUCI with MOBIUS. With MOBIUS, spectra of each order are not overlapped up to 2.3 arcsecond of slit length. Two sets of zJHK spectra are found as the two spectrographs in MOBIUS are mirror-symmetric to allow the entrance slits to be closer together on sky.

On top of cross-dispersion, another important requirement for MOBIUS maintains the image quality of LUCI after being plugged in. The spot diagram at the LBT focal plane (Fig. 4.7) and ensquared energy at the LUCI detector plane (Fig. 4.8) were examined to verify that the image quality remains the same with MOBIUS. Although the overall radius of rms spot size has increased after MOBIUS is plugged-in (Fig. 4.7), the difference is negligible as the expected smallest Full-Width Half Maximum (FWHM) at the LBT focal plane is 150 μm. In ensquared energy case (Fig. 4.8), the most measurable difference is at K-band in half width distance for 90% fraction energy, which is about 2 μm. Since the expecting seeing disk size delivered by the telescope is >2 pixels on the N3.75 camera and a pixel size is 18 μm, MOBIUS is not limiting to the image quality while expanding wavelength coverage of LUCI with little penalty.

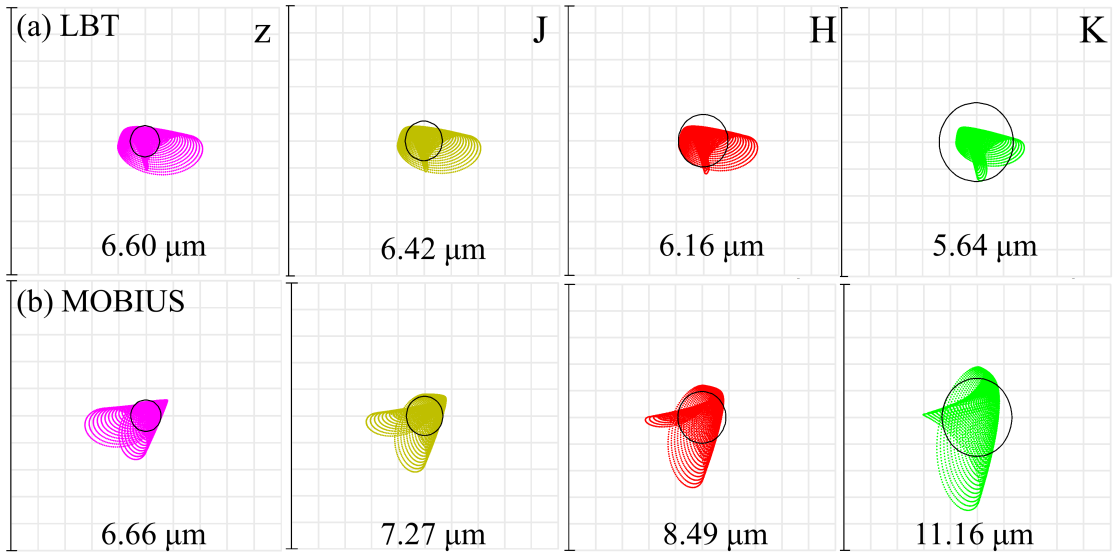


Figure 4.7 Spot diagrams at the focal plane of (a) LBT and (b) when MOBIUS is inserted in each wavelength band. Numbers in the figure show the rms radius of each spot diagram. Although the rms value is increased after the MOBIUS, considering the smallest expected FWHM at the focal plane delivered from the telescope is 150 μm, the image quality is seeing-limited.

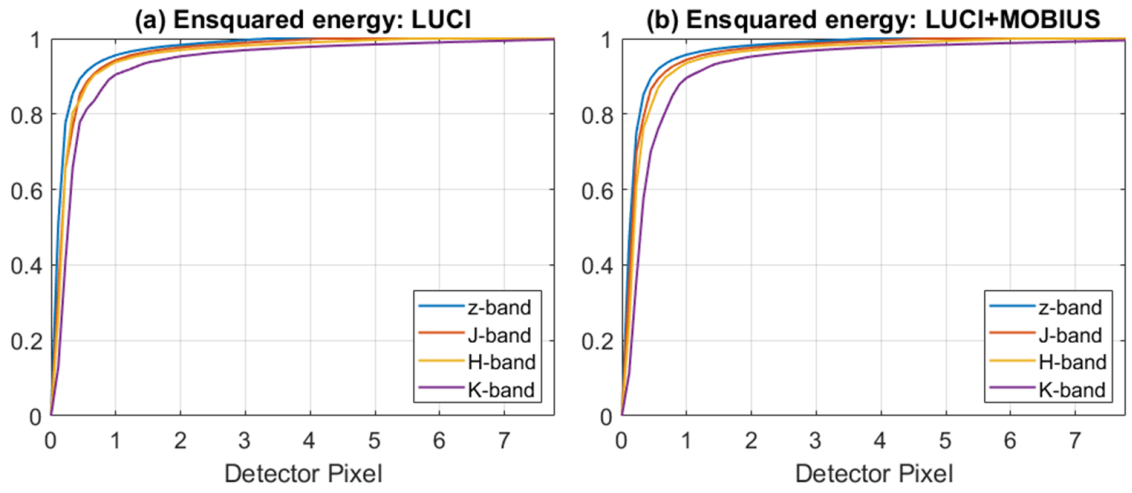


Figure 4.8 Ensquared energy comparison between (a) LUCI and (b) LUCI with MOBIUS-equipped. In every wavelength band, the difference in half width distance between LUCI and MOBIUS for 90% fraction energy is less than a pixel of the detector. This difference is insignificant as the expected seeing disk size is >2 pixels or 0.25 arcsecond.

4.2.2 Table-top result

The table-top test was performed with optical components assembled in pre-lightweighted slit mask frame (Fig. 4.9(a)). A xenon light bulb was utilized as a light source to secure broad NIR wavelength (from 0.9 μm to 1.7 μm) and formed an f/15 beam to simulate LBT (Fig. 4.9(b)). The specification of the detector employed [57] is summarized in Table 4.2.

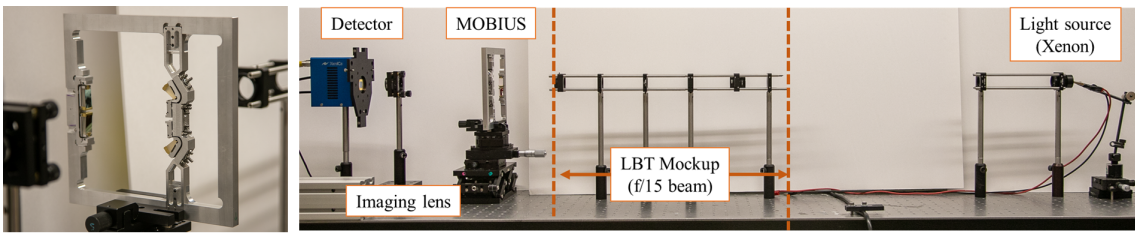
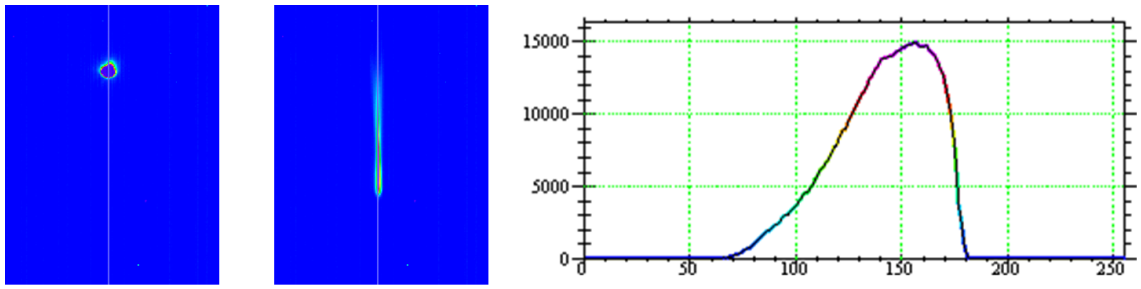


Figure 4.9 (a) MOBIUS with pre-lightweighted frame is mounted in the table-top test setup. (b) The test setup of MOBIUS.

Table 4.2 Specification of detector for table-top test.[57]

	XEVA-FPA-320 by XenICs
Type	InGaAs
Format	320×256 pixels
Pixel pitch	$30\mu m$
Spectral range	900 - 1700 μm

The table-top result is shown in Fig. 4.10. The length of resulted MOBIUS spectrum is about 110 pixels (3.3 mm) at the detector. Considering the quantum efficiency of the detector, this result is validated with the expected spectrum length from the Zemax model (3.6 mm).



(a) (b) (c)

Figure 4.10 The table-top results. (a) Image without MOBIUS and (b) with MOBIUS. (c) The profile of MOBIUS spectrum along with the center gray line in (b). The length of the MOBIUS spectrum is about 110 pixels (3.3 mm) which corresponds to the expected result from the Zemax model (3.6 mm).

CHAPTER 5

Concluding Remarks

This dissertation has presented contributions in design, fabrication, and alignment for modern optical systems. Three novel methodologies and tools have been discussed.

The first topic is the development of a dwell time optimization method called GEANS (GEnetic Algorithm-powered Non-Sequential), which can combine the modern numerical optimization computing power and the skilled human expert's brainpower (*e.g.,* optician's intuitive dwell time estimation). To provide a practical and applicable dwell time map solution, an influence matrix was built through grouping, dividing, and smoothing procedures. In this process, the excessive number of parameters were needed to be optimized such as criteria of grouping and dividing, and the size of the Gaussian smoothing filter. However, the correlation between parameters and the final dwell time map was not easy to identify mathematically. Therefore, a genetic algorithm was employed to find optimal parameters associated with the influence matrix. The performance of GEANS was demonstrated with CCOS simulation using the real surface error map and TIF data. Compared to CNS, GEANS achieved comparable FE (94.3 %) and 1000 times faster computation speed. Further, the result dwell time maps were closely reproduced the shape of the target removal map which are preferable in actual CCOS running. Error analyses were also performed to demonstrate the stability and applicability of each algorithm. Up to 10 mm of tool position and 10 % of TIF were perturbed and checked impact in PSD. Results showed that dwell time maps from GEANS were remarkably more practicable and stable than those of CNS in given perturbations. Maximum achievable tool acceleration was also applied, and the variation of dwell time maps and final residual surface error maps were investigated. The GEANS dwell time maps were smooth and continuous compared to CNS, which allowed much slower tool ac-

celeration to complete calculated dwell time maps. The flexibility and capability of being expanded add more unique value to GEANS. The optimizing parameters can be included or withdrawn depending on the achievable system conditions. Further, beyond the dwell time, other CCOS items such as the tool path or types of TIF also can be optimized while reflecting the priorities of CCOS result in GEANS.

The second part of this work is developing an alignment algorithm for deflectometry systems. The algorithm utilized computational fiducials and $\mathbf{G}$, $\mathbf{C}$ vector polynomial. The performance of the algorithm is demonstrated through alignment simulation and experimentally. In the simulation, the remaining amounts of displacement were about tens of microns in translation and about 0.001° in tilt. In the actual alignment experiment, the remaining amounts were slightly higher than simulated due to hardware limitations but still less than 100 μm in translation and 0.01° in tilt. The optical testing results show only 8.4 μm of maximum difference from the ideal metrology case. The proposed algorithm provides quick guidelines and accurate solutions in alignment that benefit freeform metrology especially when rapid and repeated surface measurements are needed in commercial applications such as quality checks for mass production without extra cost and hardware.

The last part of this work is the development of a cross-dispersion module called MOBIUS that expands the wavelength coverage of the LUCI. As MOBIUS is installed in a slit mask frame and utilized current control hardware (*i.e.* MOS-unit), additional modification to the current instrument is not necessary. With a Littrow prism configuration, MOBIUS provides a simultaneous and continuous spectrum from 0.86 μm to 2.4 μm for a single LUCI unit while having minimal impact on ensquared energy. A table-top test was performed to validate the performance of MOBIUS. With MOBIUS, LUCI can cover the NIR bands simultaneously and continuously with up to 2.3 arcsecond of slit length. An instrument with the capabilities of MOBIUS would be useful for studies of asteroids and other faint objects in the Solar System via the mixed operating mode of LBT, such as one MODS and one MOBIUS-equipped LUCI to observe a target simultaneously from UV to NIR.

The advanced methodologies and instruments developed in this dissertation will

contribute to achieve the next level of performance requirements in modern optical systems. GEANS may open a new trend in future optical fabrication and have the potential to be expanded to more serious machine learning techniques. Computational vector fiducial gives a self-calibration and alignment capability to deflectometry that is inevitable for high accuracy testing. The modular concept can be applied to other telescopes to improve functionality and efficiency with low risk.

REFERENCES

[1] Matt Johns. The giant magellan telescope (gmt). In *Ground-based and Airborne Telescopes*, volume 6267, page 626729. International Society for Optics and Photonics, 2006.

[2] Jerry Nelson and Gary H Sanders. The status of the thirty meter telescope project. In *Ground-based and Airborne Telescopes II*, volume 7012, page 70121A. International Society for Optics and Photonics, 2008.

[3] Torben Andersen, Arne L Ardeberg, Jacques Beckers, Alexander Goncharov, Mette Owner-Petersen, Holger Riewaldt, Ralph Snel, and David Walker. The euro50 extremely large telescope. In *Future Giant Telescopes*, volume 4840, pages 214–225. International Society for Optics and Photonics, 2003.

[4] Arne Ardeberg, Torben Andersen, Jacques Beckers, Michael Browne, Anita Enmark, Per Knutsson, and Mette Owner-Petersen. From euro50 toward a european elt. In *Ground-based and Airborne Telescopes*, volume 6267, page 626725. International Society for Optics and Photonics, 2006.

[5] Ronald Aspden, Ralph McDonough, and Francis R Nitchie. Computer assisted optical surfacing. *Applied optics*, 11(12):2739–2747, 1972.

[6] RE Wagner and RR Shannon. Fabrication of aspherics using a mathematical model for material removal. *Applied Optics*, 13(7):1683–1689, 1974.

[7] Robert A Jones. Computer-controlled polishing of telescope mirror segments. *Optical Engineering*, 22(2):222236, 1983.

[8] Robert A Jones. Computer-controlled optical surfacing with orbital tool motion. *Optical engineering*, 25(6):256785, 1986.

[9] Robert A. Jones and Wiktor J. Rupp. Rapid optical fabrication with CCOS. In Gregory M. Sanger, Paul B. Reid, and Lionel R. Baker, editors, *Advanced Optical Manufacturing and Testing*, volume 1333, pages 34 – 43. International Society for Optics and Photonics, SPIE, 1990. doi: 10.1117/12.22787. URL `https://doi.org/10.1117/12.22787`.

[10] Harvey Pollicove and Don Golini. Deterministic manufacturing processes for precision optical surfaces. In *Key Engineering Materials*, volume 238, pages 53–58. Trans Tech Publ, 2003.

[11] James H Burge, S Benjamin, D Caywood, C Noble, M Novak, C Oh, R Parks, B Smith, P Su, M Valente, et al. Fabrication and testing of 1.4-m convex off-axis aspheric optical surfaces. In *Optical manufacturing and testing VIII*, volume 7426, page 74260L. International Society for Optics and Photonics, 2009.

[12] M. J. Valente, D. W. Kim, C. J. Oh, M. J. Novak, and J. H. Burge. Fabrication of 4-meter class astronomical optics. In Eli Atad-Ettedgui and Dietrich Lemke, editors, *Modern Technologies in Space- and Ground-based Telescopes and Instrumentation*, volume 7739, pages 880 – 892. International Society for Optics and Photonics, SPIE, 2010. doi: 10.1117/12.861979. URL `https://doi.org/10.1117/12.861979`.

[13] HM Martin, RG Allen, JH Burge, DW Kim, JS Kingsley, MT Tuell, SC West, C Zhao, and T Zobrist. Fabrication and testing of the first 8.4-m off-axis segment for the giant magellan telescope. In *Modern Technologies in Space- and Ground-based Telescopes and Instrumentation*, volume 7739, page 77390A. International Society for Optics and Photonics, 2010.

[14] James H Burge, Dae Wook Kim, and Hubert M Martin. Process optimization for polishing large aspheric mirrors. In *Advances in Optical and Mechanical Technologies for Telescopes and Instrumentation*, volume 9151, page 91512R. International Society for Optics and Photonics, 2014.

[15] Chang Jin Oh, Andrew E Lowman, Greg A Smith, Peng Su, Run Huang, Tianquan Su, Daewook Kim, Chunyu Zhao, Ping Zhou, and James H Burge. Fabrication and testing of 4.2 m off-axis aspheric primary mirror of daniel k. inouye solar telescope. In *Advances in Optical and Mechanical Technologies for Telescopes and Instrumentation II*, volume 9912, page 99120O. International Society for Optics and Photonics, 2016.

[16] Peng Su, Robert E. Parks, Lirong Wang, Roger P. Angel, and James H. Burge. Software configurable optical test system: a computerized reverse hartmann test. *Appl. Opt.*, 49(23):4404–4412, Aug 2010. doi: 10.1364/AO.49.004404. URL `http://ao.osa.org/abstract.cfm?URI=ao-49-23-4404`.

[17] Peng Su, Shanshan Wang, Manal Khreishi, Yuhao Wang, Tianquan Su, Ping Zhou, Robert E. Parks, Kevin Law, Mario Rascon, Tom Zobrist, Hubert Martin, and James H. Burge. SCOTS: a reverse Hartmann test with high dynamic range for Giant Magellan Telescope primary mirror segments. In *Modern Technologies in Space- and Ground-based Telescopes and Instrumentation II*, volume 8450, page 340. International Society for Optics and Photonics, Proc. SPIE, 2012. URL `https://doi.org/10.1117/12.926719`.

[18] Run Huang, Peng Su, James H. Burge, Lei Huang, and Mourad Idir. High-accuracy aspheric x-ray mirror metrology using Software Configurable Optical Test System/deflectometry. *Optical Engineering*, 54(8):1 – 10, 2015. doi: 10.1117/1.OE.54.8.084103. URL https://doi.org/10.1117/1.OE.54.8.084103.

[19] Marcus Petz and Rainer Tutsch. Reflection grating photogrammetry: a technique for absolute shape measurement of specular free-form surfaces. In *Optical Manufacturing and Testing VI*, volume 5869, page 366. International Society for Optics and Photonics, Proc. SPIE, 2005. URL https://doi.org/10.1117/12.617325.

[20] Yong-Liang Xiao, Xianyu Su, and Wenjing Chen. Flexible geometrical calibration for fringe-reflection 3d measurement. *Opt. Lett.*, 37(4):620–622, Feb 2012. doi: 10.1364/OL.37.000620. URL http://ol.osa.org/abstract.cfm?URI=ol-37-4-620.

[21] Tian Zhou, Kun Chen, Haoyun Wei, and Yan Li. Improved system calibration for specular surface measurement by using reflections from a plane mirror. *Appl. Opt.*, 55(25):7018–7028, Sep 2016. doi: 10.1364/AO.55.007018. URL http://ao.osa.org/abstract.cfm?URI=ao-55-25-7018.

[22] Xiaoting Deng, Nan Gao, and Zonghua Zhang. A calibration method for system parameters in direct phase measuring deflectometry. *Applied Sciences*, 9(7), 2019. ISSN 2076-3417. doi: 10.3390/app9071444. URL https://www.mdpi.com/2076-3417/9/7/1444.

[23] Mei Hui, Xinji Li, Ning Li, Ming Liu, Liquan Dong, Lingqin Kong, and Yuejin Zhao. Precise positioning of the test surface and screen in a coaxial software configurable optical test system. *Measurement Science and Technology*, 31(4): 045010, 2020.

[24] Evelyn Olesch, Christian Faber, and Gerd Häusler. Deflectometric self-calibration for arbitrary specular surfaces. In *Proc. DGao*, page 7536, 2011.

[25] Xueyang Xu, Xiangchao Zhang, Zhenqi Niu, Wei Wang, Yifan Zhu, and Min Xu. Self-calibration of in situ monoscopic deflectometric measurement in precision optical manufacturing. *Optics Express*, 27(5):7523–7536, 2019.

[26] Congli Wang, Ni Chen, and Wolfgang Heidrich. Towards self-calibrated lens metrology by differentiable refractive deflectometry. *Optics Express*, 29(19): 30284–30295, 2021.

[27] Daodang Wang, Sen Zhang, Rengmao Wu, Chih Yu Huang, Hsiang-Nan Cheng, and Rongguang Liang. Computer-aided high-accuracy testing of reflective

surface with reverse hartmann test. *Opt. Express*, 24(17):19671–19681, Aug 2016. doi: 10.1364/OE.24.019671. URL http://www.opticsexpress.org/abstract.cfm?URI=oe-24-17-19671.

[28] Daodang Wang, Zhidong Gong, Ping Xu, Chao Wang, Rongguang Liang, Ming Kong, and Jun Zhao. Accurate calibration of geometrical error in reflective surface testing based on reverse hartmann test. *Opt. Express*, 26(7):8113–8124, Apr 2018. doi: 10.1364/OE.26.008113. URL http://www.opticsexpress.org/abstract.cfm?URI=oe-26-7-8113.

[29] Angela Davies, Trent Vann, Christopher Evans, and Mark Butkiewicz. Phase measuring deflectometry for determining 5 dof misalignment of segmented mirrors. In *Applied Optical Metrology II*, volume 10373, page 103730H. International Society for Optics and Photonics, Proc. SPIE, 2017.

[30] John Mineo Kam. Differential phase measuring deflectometry for high-sag freeform optics. Master's thesis, The University of Arizona, 2019.

[31] Maham Aftab, James H Burge, Greg A Smith, Logan Graves, Chang-jin Oh, and Dae Wook Kim. Modal data processing for high resolution deflectometry. *International Journal of Precision Engineering and Manufacturing-Green Technology*, 6(2):255–270, 2019.

[32] Maham Aftab, Logan R. Graves, James H. Burge, Greg A. Smith, Chang Jin Oh, and Dae Wook Kim. Rectangular domain curl polynomial set for optical vector data processing and analysis. *Optical Engineering*, 58(9):1 – 10, 2019. doi: 10.1117/1.OE.58.9.095105. URL https://doi.org/10.1117/1.OE.58.9.095105.

[33] Vishnu Reddy, Tasha L Dunn, Cristina A Thomas, Nicholas A Moskovitz, and Thomas H Burbine. Mineralogy and surface composition of asteroids. *Asteroids*, IV(2867), 2015.

[34] J. M. Hill, D. S. Ashby, J. G. Brynnel, J. C. Christou, John K. Little, D. M. Summers, C. Veillet, and R. M. Wagner. The large binocular telescope: binocular all the time. In *Ground-based Airborne Telesc. V*, volume 9145 of *Proc. SPIE*, page 914502, 2014.

[35] R. W. Pogge, B. Atwood, D. F. Brewer, P. L. Byard, M. A. Derwent, R. Gonzalez, P. Martini, J. A. Mason, T. P. O'Brien, P. S. Osmer, D. P. Pappalardo, D. P. Steinbrecher, E. J. Teiga, and R. Zhelem. The multi-object double spectrographs for the large binocular telescope. In *Ground-based and Airborne Instrumentation for Astronomy III*, volume 7735 of *Proc. SPIE*, page 77350A, 2010.

[36] Holger Mandel, Walter Seifert, Reiner Hofmann, Marcus Jütte, Rainer Lenzen, Nancy Ageorges, Dominik Bomans, Peter Buschkamp, Ralf-Jürgen Dettmar, Carmen Feiz, Hans Gemperlein, André Germeroth, Lutz Geuer, Jochen Heidt, Volker Knierim, Werner Laun, Michael Lehmitz, Ulrich Mall, Peter Müller, Vianac Naranjo, Kai Polsterer, Andreas Quirrenbach, Ludwig Schäffner, Florian Schwind, Peter Weiser, and Harald Weisz. LUCIFER status report: summer 2008. In *Ground-based Airborne Instrum. Astron. II*, volume 7014 of *Proc. SPIE*, page 70143S, 2008.

[37] Dae Wook Kim, Sug-Whan Kim, and James H Burge. Non-sequential optimization technique for a computer controlled optical surfacing process using multiple tool influence functions. *Optics express*, 17(24):21850–21866, 2009.

[38] Charles L Carnal, Charles M Egert, and Kathy W Hylton. Advanced matrix-based algorithm for ion-beam milling of optical components. In *Current Developments in Optical Design and Optical Engineering II*, volume 1752, pages 54–63, 1992. doi: 10.1117/12.130719. URL `https://doi.org/10.1117/12.130719`.

[39] Jian Fen Wu, Zhen Wu Lu, Hong Xin Zhang, and Tai Sheng Wang. Dwell time algorithm in ion beam figuring. *Applied optics*, 48(20):3930–3937, 2009.

[40] Tianyi Wang, Lei Huang, Matthew Vescovi, Dennis Kuhne, Kashmira Tayabaly, Nathalie Bouet, and Mourad Idir. Study on an effective one-dimensional ion-beam figuring method. *Opt. Express*, 27(11):15368–15381, May 2019. doi: 10.1364/OE.27.015368. URL `http://www.opticsexpress.org/abstract.cfm?URI=oe-27-11-15368`.

[41] Peng Ji, Duo Li, Xing Su, Zheng Qiao, Kaiji Wu, Li Song, Bing Peng, and Bo Wang. Optimization strategy for the velocity distribution based on tool influence function non-linearity in atmospheric pressure plasma processing. *Precision Engineering*, 65:269–278, 2020.

[42] Aleksei Chernyshev, Nikolay Chkhalo, Ilya Malyshev, Mikhail Mikhailenko, Alexey Pestov, Roman Pleshkov, Ruslan Smertin, Mikhail Svechnikov, and Mikhail Toropov. Matrix based algorithm for ion-beam figuring of optical elements. *Precision Engineering*, 69:29–35, 2021.

[43] Tianyi Wang, Lei Huang, Matthew Vescovi, Dennis Kuhne, Yi Zhu, Vipender S Negi, Zili Zhang, Chunjin Wang, Xiaolong Ke, Heejoo Choi, et al. Universal dwell time optimization for deterministic optics fabrication. *Optics Express*, 29 (23):38737–38757, 2021.

[44] Dae Wook Kim and Sug-Whan Kim. Static tool influence function for fabrication simulation of hexagonal mirror segments for extremely large telescopes. *optics express*, 13(3):910–917, 2005.

[45] JH Holland. Adaptation in natural and artificial systems, univ. of mich. press. *Ann Arbor*, 1975.

[46] Kenneth Alan De Jong. *An analysis of the behavior of a class of genetic adaptive systems.* University of Michigan, 1975.

[47] Zhou Wang, Alan C Bovik, Hamid R Sheikh, and Eero P Simoncelli. Image quality assessment: from error visibility to structural similarity. *IEEE transactions on image processing*, 13(4):600–612, 2004.

[48] Hyukmo Kang, Henry Quach, Heejoo Choi, Greg A. Smith, and Dae Wook Kim. Computational alignment of on-machine deflectometry. In *Optical Manufacturing and Testing XIII*, volume 11487, page 139. International Society for Optics and Photonics, Proc. SPIE, 2020. URL `https://doi.org/10.1117/12.2576955`.

[49] Hwan Joo Jeong, George N. Lawrence, and Kie B. Nahm. Auto-Alignment Of A Three-Mirror Off-Axis Telescope By Reverse Optimization And End-To-End Aberration Measurements. In *Current Developments in Optical Engineering II*, volume 0818, page 430. International Society for Optics and Photonics, Proc. SPIE, 1987. URL `https://doi.org/10.1117/12.978915`.

[50] Eugene D Kim, Young-Wan Choi, Myung-Seok Kang, and Se Chol Choi. Reverse-optimization alignment algorithm using zernike sensitivity. *Journal of the Optical Society of Korea*, 9(2):68–73, 2005.

[51] Peter Buschkamp, Reiner Hofmann, Hans Gemperlein, Kai Polsterer, Nancy Ageorges, Frank Eisenhauer, Reinhard Lederer, Mathias Honsberg, Marcus Haug, Johann Eibl, et al. The lucifer mos: a full cryogenic mask handling unit for a near-infrared multi-object spectrograph. In *Ground-based and Airborne Instrumentation for Astronomy III*, volume 7735 of *Proc. SPIE*, page 773579, 2010.

[52] IK Ilev. Simple autocollimation laser refractometer with highly sensitive, fiber-optic output. *Applied optics*, 34(10):1741–1743, 1995.

[53] David W Warren and Sara Lampen. Littrow spectrographs for moderate resolution infrared applications. In *Imaging Spectrometry XXI*, volume 9976, pages 18–23. SPIE, 2016.

[54] Jochen Heidt and David Thompson. LUCI User Manual. September 7, 2016 `https://sites.google.com/a/lbto.org/luci/documents-and-links`, 2016.

[55] Michael Bass and Optical Society of America. *Handbook of optics*. New York : McGraw-Hill, New York, 2nd ed. edition, 1995.

[56] Jean-François Lavigne. Design of an infrared integral field spectrograph specialized for direct imaging of exoplanets. In *International Optical Design Conference 2006*, volume 6342, page 63421M. International Society for Optics and Photonics, 2006.

[57] Italo Foppiani, Matteo Lombini, Giovanni Bregoli, Giuseppe Cosentino, Emiliano Diolaiti, Giancarlo Innocenti, Daniel Meschke, Ralf-Rainer Rohloff, Thomas M Herbst, and Costantino Ciattaglia. An infrared test camera for lbt adaptive optics commissioning. In *Adaptive Optics Systems*, volume 7015, page 701562. International Society for Optics and Photonics, 2008.

APPENDIX A

Genetic algorithm-powered non-sequential dwell time optimization for large optics fabrication

Hyukmo Kang, Tianyi Wang, Heejoo Choi, and Daewook Kim

Journal article published at ***Optics Express***

Copyright Transfer Agreement Opt. Express 30(10), 16442-16458 (2022). Copyright Optical Society of America. Reprinted with permission.

Research Article | Vol. 30, No. 10 / 9 May 2022 / Optics Express 16442
Optics EXPRESS

Genetic algorithm-powered non-sequential dwell time optimization for large optics fabrication

HYUKMO KANG,[1] TIANYI WANG,[2] HEEJOO CHOI,[1,3] AND DAEWOOK KIM[1,3,4,*]

[1]Wyant College of Optical Sciences, University of Arizona, 1630 E. University Blvd., Tucson, AZ 85721, USA
[2]National Synchrotron Light Source II (NSLS-II), Brookhaven National Laboratory, PO Box 5000, Upton, New York 11973, USA
[3]Large Binocular Telescope Observatory, University of Arizona, 933 N. Cherry Ave., Tucson, AZ 85721, USA
[4]Department of Astronomy and Steward Observatory, University of Arizona, 933 N. Cherry Ave., Tucson, AZ 85721, USA
*dkim@optics.arizona.edu

Abstract: Computer Controlled Optical Surfacing (CCOS) is widely applied for fabricating large aspheric optical surfaces. For large optics fabrication, various sizes of polishing tools are used sequentially. This raises the importance of efficient and globally optimized dwell time map of each tool. In this study, we propose a GEnetic Algorithm-powered Non-Sequential (GEANS) optimization technique to improve the feasibility of the conventional non-sequential optimization technique. GEANS consists of two interdependent parts: i) compose an influence matrix by imposing constraints on adjacent dwell points and ii) induce the desired dwell time map through the genetic algorithm. CCOS simulation results show that GEANS generates a preferable dwell time map that provides high figuring efficiency and structural similarity with the shape of target removal map, while improving computational efficiency more than 1000 times over the conventional non-sequential optimization method. The practicability of GEANS is demonstrated through error analyses. Random tool positioning error and tool influence function errors are imposed on dwell time maps. Compared to the conventional non-sequential optimization method, the power spectral density values of residual surface error from GEANS remain stable. GEANS also shows superior applicability when the maximum acceleration of a tool is applied.

© 2022 Optica Publishing Group under the terms of the Optica Open Access Publishing Agreement

1. Introduction

Since Computer Controlled Optical Surfacing (CCOS) developed, it has been widely applied for large aspheric optical surface fabrication [1–8]. The next generation telescope projects, such as Giant Magellan Telescope (GMT) [9], Thirty Meter Telescope (TMT) [10], and Extremely Large Telescope (ELT) [11,12] are required to meet the challenge of manufacturing off-axis segments. These projects contain from seven to several hundreds of meter-class segmented aspheric mirrors, so the advanced CCOS process must be efficient while accomplishing high precision optical surfaces.

In the CCOS process, dwell time calculation is an essential procedure. It deterministically guides the motion of machine tools at successive dwell points to remove material from an optical surface. In the past few decades, researchers have studied dwell time calculation algorithms which can be categorized into iterative algorithms [13,14], Fourier transform-based algorithms [15–17], matrix-based algorithms [18–24], and Bayesian-based algorithms [25]. These algorithms aim to obtain non-negative and smooth dwell time solutions that minimize the estimated residual errors of the optical surface. In the CCOS process of large optics fabrication, such as the CCOS platform for GMT fabrication at The University of Arizona, multiple tools with different sizes

#457505 https://doi.org/10.1364/OE.457505
Journal © 2022 Received 7 Mar 2022; revised 14 Apr 2022; accepted 19 Apr 2022; published 28 Apr 2022

and tool paths are utilized for a single workpiece [26–28] to correct the surface errors for various spatial frequencies. The tool path parameters, such as the machining interval and the path type (raster path, spiral path, random path, *etc.*.), usually vary depending on the shape of the workpiece and the physical constraints of the machine tools. Therefore, the matrix-based methods are preferred in our CCOS process since the dwell time can be flexibly calculated for arbitrary dwell positions. Also, to improve the overall processing efficiency, the dwell time is expected to be calculated for multiple tools in the planning phase, and the metrology is only performed after all the tools complete their assigned works.

The dwell time for multiple tools was mostly optimized sequentially until the Non-Sequential dwell time optimization method (NS) was proposed in our previous research [19]. The NS method considers multiple Tool Influence Functions (TIFs) simultaneously in a single optimization run, which implicitly adds the necessary regularization to stabilize the linear solver. Therefore, it balances the dwell time for each tool and reduces the generation of mid-spatial-frequency errors effectively, which is a common issue in the sequential matrix-based methods. The results from the Conventional NS (CNS) are mathematically ideal and show high figuring efficiency in terms of the estimated residual errors. However, they have limitations in practical application. First, in terms of accuracy, CNS considers neither the Computer Numerical Control (CNC) hardware limitations (*i.e.*, the maximum local slope of the dwell time between each two consecutive dwell points) nor the practical preference that the dwell time map should smoothly resemble the shape of the target removal map in order to minimize any mid-to-high spatial frequency residual errors. Furthermore, in terms of computational efficiency, the increased size of the influence function matrix due to multiple TIFs brings heavier computational burden and makes iterative optimization difficult.

In this study, we proposed a GEnetic Algorithm-powered Non-Sequential (GEANS) dwell time optimization method which enhances the feasibility of a dwell time map and improves its adaptability in the practical CCOS process. GEANS provides a novel method to compose the influence function matrix for multiple TIFs. It not only improves the computational efficiency of CNS by a factor of 1000, but also induces the optimized dwell time map to be smooth and have similar structure to the target removal map. The Genetic Algorithm (GA) is used to globally optimize the detailed parameters related to CNC dynamics limitations such as local slope of the dwell time. It also promotes the optimization results to have preferred characteristics that are mentioned above while achieving high figuring efficiency. These features enable to find desirable and practical dwell time maps for CCOS process.

The rest of the paper is organized as follows. The theoretical backgrounds for NS dwell time optimization and genetic algorithm are briefly reviewed in Section 2. In Section 3, we introduce GEANS method in detail. Section 4 presents the simulation results and the performance comparison between CNS and GEANS. Section 5 discusses the limitations of the proposed method, and Section 6 summarizes the implications of GEANS and concludes the paper.

2. Background

2.1. Non-sequential dwell time optimization

The purpose of dwell time optimization is to find a removal map, $z(x, y)$, which is close or equal to the target removal map, $z_d(x, y)$. Derived from the Preston equation [29], the material removal process in CCOS has been modeled as the convolution of a TIF, $t(x, y)$, with the corresponding dwell time, $d(\xi, \eta)$. When the sampling has finite resolution, the convolution process can be represented in matrix form as

$$z(x_k, y_k) = \sum_{i=1}^{N_d} t(x_k - \xi_i, y_k - \eta_i)\, d(\xi_i, \eta_i) \tag{1}$$

for $k = 1, 2, \cdots, N_z$, where N_z is the number of sampling points in $z(x_k, y_k)$, N_d is the number of dwell points, (ξ_i, η_i) is the ith dwell point, and $t\,(x_k - \xi_i, y_k - \eta_i)$ represents the material removed per unit time at point (x_k, y_k) when the TIF dwells at (ξ_i, η_i). Depending on the tool path or available tool overhang distance, (x_k, y_k) and (ξ_i, η_i) coordinates can be different. Equation (1) can also be represented as

$$\underbrace{\begin{pmatrix} z_1 \\ z_2 \\ \vdots \\ z_{N_z} \end{pmatrix}}_{\mathbf{z}} = \underbrace{\begin{pmatrix} t_{1,1} & t_{1,2} & \cdots & t_{1,N_d} \\ t_{2,1} & t_{2,2} & \cdots & t_{2,N_d} \\ \vdots & \vdots & \ddots & \vdots \\ t_{N_z,1} & t_{N_z,2} & \cdots & t_{N_z,N_d} \end{pmatrix}}_{\mathbf{t}} \underbrace{\begin{pmatrix} d_1 \\ d_2 \\ \vdots \\ d_{N_d} \end{pmatrix}}_{\mathbf{d}} \tag{2}$$

where $\mathbf{z}$ represents material removal map, $\mathbf{t}$ represents influence function, and $\mathbf{d}$ represents dwell time of each dwell point in matrix form. Since the convolution result between a dwell time basis, which is a group of tool location points with relative weights, and a TIF will compose a row of $\mathbf{t}$, it would be a sparse matrix that most elements of $\mathbf{t}$ are zero except the convolution area.

In large optics fabrication, multiple TIFs are combined with different tool paths to achieve the desired residual error, $z_r(x, y) = z_d(x, y) - z(x, y)$, in the shortest available overall polishing time. In a previous study [19], we proposed the NS technique that counts multiple TIFs simultaneously in a single optimization process, which can be expressed as

$$z(x_k, y_k) = \sum_{j=1}^{N_t} \sum_{i=1}^{N_d^j} t_j(x_k - \xi_{j,i}, y_k - \eta_{j,i})\; d_j(\xi_{j,i}, \eta_{j,i}) \tag{3}$$

where N_t is the number of TIFs, $(\xi_{j,i}, \eta_{j,i})$ represents the ith dwell point on the tool path of the jth TIF, and N_d^j is the number of total dwell points for the jth TIF. Each TIF has its own dwell time map, and the dwell points of each TIF can be varied when necessary. By considering multiple TIFs in optimization, the NS can achieve more balanced dwell time maps for each TIF to enhance CCOS efficiency than those optimized in the sequential way. Equation (3) can be represented as

$$\mathbf{z} = \left[\mathbf{t_1}, \quad \cdots \quad , \mathbf{t_{N_t}}\right] \left[\mathbf{d_1}, \quad \cdots \quad , \mathbf{d_{N_t}}\right]^T \tag{4}$$

In Eq. (4), as the NS method utilizes multiple tools, multiple influence matrices ($\mathbf{t_{N_t}}$) and corresponding dwell time matrices are included in the calculation.

Additionally, we can add alignment terms, such as piston, tip and tilt, to the target removal amount and run optimization. This process can be expressed as

$$z(x_k, y_k) = \sum_{j=1}^{N_t} \sum_{i=1}^{N_d^j} t_j(x - \xi_{j,i}, y - \eta_{j,i})\; d_j(\xi_{j,i}, \eta_{j,i}) + \sum_{l=1}^{N_a} a_l(x, y) \tag{5}$$

where N_a is the number of optimized alignment terms and $a_l(x, y)$ is adjusted amount of the lth term. Considering the solution of a dwell time map must be non-negative in CCOS processes, the alignment terms help relax this constraint in the optimization, although the total dwell time may slightly increase.

The optimized dwell time map $\mathbf{d}_{opt}$ is calculated as

$$\mathbf{d}_{opt} = \min_{\mathbf{d},\mathbf{a}} \|\mathbf{td} - (\mathbf{z}_d + \mathbf{a})\|_2^2 \quad s.t.\ \mathbf{d} \geq \mathbf{0} \tag{6}$$

where $\mathbf{z}_d$, represent the target removal map and $\mathbf{a}$ represents adjusted alignment map. The amount of alignments will be calculated and optimized to minimize residual figure error. Therefore the estimated residual error map, $\mathbf{z}_f$, can be represented as

$$\mathbf{z}_f = \mathbf{z}_d - \mathbf{td}_{opt} - \mathbf{a} \tag{7}$$

2.2. Genetic algorithm

A GA is an evolutionary algorithm that models processes of natural selection to search a globally optimized solution [30,31]. It finds an optimized solution set (*i.e.*, chromosome) which is encoded in a sequence of numbers that representing optimizing parameters (*i.e.*, gene) among given parameter candidates (*i.e.*, gene pool). Each chromosome of a population is evaluated by predefined fitness function. The next generation of population is created through following genetic operations. To prompt the evolution path towards as our preference, those operations are based on the fitness. Chromosomes with higher fitness score has more probability to be mated (selection) and transfer their genes to the next generation by exchanging genes (crossover). Especially, chromosomes which have the highest fitness can be carried to the next generation directly (elitism) to keep the superiority. While exchanging genes, some of genes can be randomly selected and changed to others with a certain probability (mutation). Often, immigrants are joining to the next generation to keep the diversity in population. Over generations, the chromosomes are evolving toward the optimal solution until the maximum number of generation.

The GA has a high potential in solving complex problems such as dwell time optimization in CCOS process. For example, we can guide the optimization result to reflect our preference using the fitness function with preferred target criteria. Besides, if the gene pool has practical machining parameters only, the optimized dwell time map will be achievable solution in consequence. Thus, the GA enables us to find optimal combination of parameters while considering machining feasibility or our preference in CCOS process.

3. Genetic algorithm-powered non-sequential dwell time optimization

Our previously proposed CNS method [19] has shown the performance improvement in figuring efficiency compared to the sequential optimization. The optimized dwell time map from CNS, however, has issues when applying it in a laboratory setting. Firstly, the hardware capabilities are not reflected during the calculation. The applicable maximum local slope of dwell time map is limited due to the finite acceleration of machine. Hence a smooth dwell time map is preferred in actual CCOS processes, yet is not considered machine axis motion in CNS. Secondly, the calculated dwell time map barely resembles the target surface error map shape. Because of uncertainties in tool positioning and tool vibration, a dwell time map that is different from the target removal map increases the risk of inducing new surface error after figuring. Lastly, as the size of the influence matrix is multiplied by the number of TIFs in CNS, the computation time rises considerably. Especially in large optics fabrication (*e.g.*, GMT 8.4 *m* diameter mirror segment), the computational burden is even heavier since the sizes of measured removal maps and TIFs are enormous.

The main objectives of GEANS is to enhance the performance of CNS to produce a preferable dwell time map which closely duplicates the shape of a target error map and reflects the machining capability of the CNC unit while boosting the computational efficiency. GEANS consists of two interdependent parts: Composing the bases of the influence function matrix, and optimizing the dwell time using those bases via GA. Details of GEANS are explained in the rest of this section.

3.1. Set up the bases of influence function matrix

As Eq. (3) is usually ill-posed, finding the dwell time map relies on an optimization process. Constructing proper building blocks of the influence function matrix enables the optimization algorithm to find desired results easily and improves computational efficiency. We set up dwell time bases using following fundamental rules: i) grouping ii) dividing and iii) smoothing. Because each TIF has its own dwell time map in NS, the following process would be applied to each TIF case independently as well.

The first step is to form a single dwell time basis by grouping neighboring dwell points with similar removal amount. The idea of grouping is valid as adjacent dwell points with similar target removal amounts are expected to require similar dwell time distribution as well. It also benefits in computing costs as the total size of dwell time matrix is decreased. For instance, if n-points are combined and worked as a single dwell basis, the size of dwell time matrix is reduced by $n - 1$. Then, if the size of a single basis is too large, the optimization engine would not have enough degree of freedom in solution space. Therefore, in the algorithm, a criterion is set and a big single basis will be divided into smaller pieces to secure flexibility in optimization so that the overall figuring efficiency can be improved. A Smoothing filter is applied to all dwell time bases that are generated from above steps. We applied the Gaussian smoothing filter in GEANS to prevent sharp features and impose constraints on the local slope of the dwell time map. In addition, smoothing prevents square-wave like dwell time solutions from grouping and dividing processes and provides more reasonable solutions. After all, the convolution between each dwell time basis and TIF forms the influence matrix ($\mathbf{t}$) from Section 2. Through these processes, as the dwell time basis is more chunky and smooth than that of CNS, we can expect the result dwell time map would be less pointy than CNS. Figure 1 illustrates the process of making influence matrix.

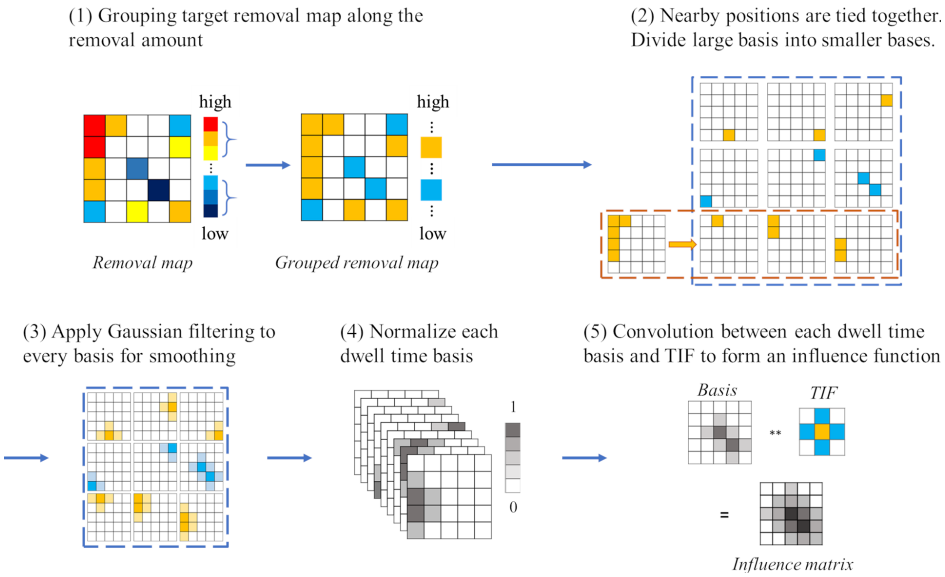


Fig. 1. The flowchart of generating an influence matrix. Specific figures relate to each step, such as the number of groups at step will be optimized through GA. The detailed explanations are illustrated in Fig. 2 in the following section.

3.2. Optimization parameters to construct influence function matrix

By leveraging GA, we can find optimal parameter sets for the influence function matrix and GEANS to generate a dwell time map while reflecting our preference in solution.

To implement GA, we need to define the parameters to be optimized (genes) and solution space (gene pool) first. In the case of GEANS, the parameters related in making influence matrix, explained in Section 3.1, comprise genes. Then the gene pool is built within the range available to the machine to assure the feasibility of a dwell time map. The gene pool should be wide enough to not restrain a possible solution space too hard, but at the same time, should not be too wide for efficient optimization.

The dwell position of a tool is another essential parameter to be determined. Since the accessible dwell points are limited by tool size and motion, a smaller size tool is advantageous to edge-side fabrication of the workpiece in general. Therefore, in our application of GEANS, we limited the coverage of the smallest tool to edge-side only to find reasonable balance between total fabrication time and remaining surface error. The applied parameters are summarized in Fig. 2.

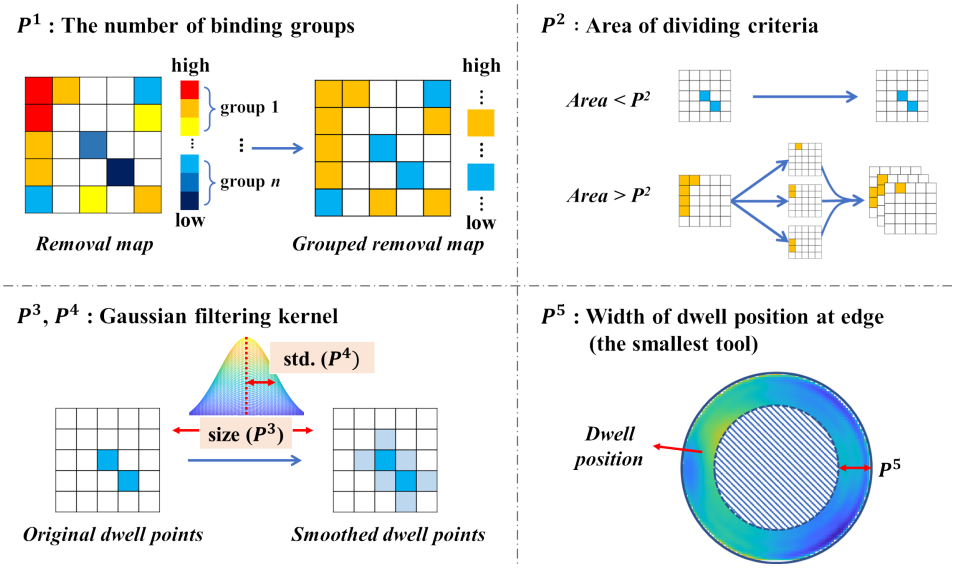


Fig. 2. Parameters to be optimized through genetic algorithm. For GEANS, the number of optimization parameters is multiplied with the number of TIFs. Note that P^1 and P^2 are simulation-related parameters while P^3, P^4 and P^5 are tool-related parameters which are determined by machining capabilities.

3.3. Optimization and fitness function

Setting an appropriate fitness function is critical to lead the evolution of GA for our needs. The valid dwell time map in CCOS should duplicate the target removal map shape while achieving high figuring efficiency. Therefore, we evaluated the performance of the dwell time map with two indices: figuring efficiency and structural similarity.

Figuring Efficiency (FE) represents the accuracy of the algorithm for a given target removal map. The FE is defined as

$$FE(\mathbf{z}_d, \mathbf{z}_f) \equiv \frac{RMS[\mathbf{z}_d] - RMS[\mathbf{z}_f]}{RMS[\mathbf{z}_d]} \tag{8}$$

where RMS means Root Mean Squared value of each map. FE varies from 0 to 1, and a higher value means better figuring performance.

The Structural SIMilarity (SSIM) [32] is a quantified index to represent the visual similarity between two signals, μ_A and μ_B, by comparing luminance (l), contrast (c), and structural information (s). SSIM score varies from 0 to 1, and higher score means better similarity. The SSIM equation is represented as

$$SSIM(\mu_A, \mu_B) = l(\mu_A, \mu_B) \cdot c(\mu_A, \mu_B) \cdot s(\mu_A, \mu_B) \tag{9}$$

This index can be utilized to evaluate the validity of the dwell time map in CCOS since the valid dwell time map should closely copy the shape of the target removal map. We represent SSIM index between the normalized target error map and dwell time map of a TIF as

$$S_k(\mathbf{z}_d^{norm}, \mathbf{d}_k^{norm}) \equiv SSIM(\mathbf{z}_d^{norm}, \mathbf{d}_k^{norm}) \tag{10}$$

where $\mathbf{z}_d^{norm}$ and $\mathbf{d}_k^{norm}$ represent normalized target error map and dwell time map of kth TIF.

With FE and S_k, we form the fitness function (Q) as

$$Q(FE, S_k) = \frac{FE + \sum_{k=1}^{l} w_k \cdot S_k}{1 + \sum_{k=1}^{l} w_k} \tag{11}$$

where w is relative weight of SSIM of each TIF case compared to FE. Note that the w has no general solution for the simulation, and can be changed based on the priority of the optimization result or machining capability.

The whole process of GEANS simulation is shown in the following Fig. 3.

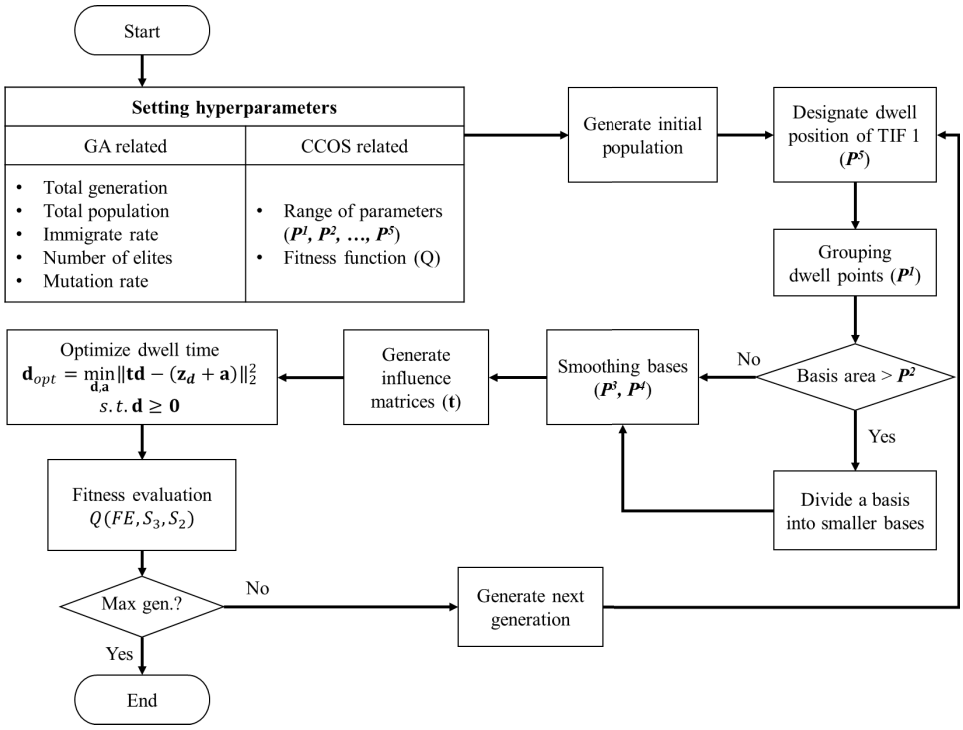


Fig. 3. Flowchart of GEANS simulation.

4. Verification of GEANS through simulations

4.1. CCOS simulation setup

We performed CCOS simulation to verify the performance of GEANS compared to CNS. We employed actual measurement data of the target removal map (Fig. 4), and TIF data for a more realistic simulation. The target workpiece was a mirror, 4.25 m in diameter with an initial RMS surface figure error of 0.749 μm. The target removal map was 341 by 341 pixels with a 12.5 mm pixel scale.

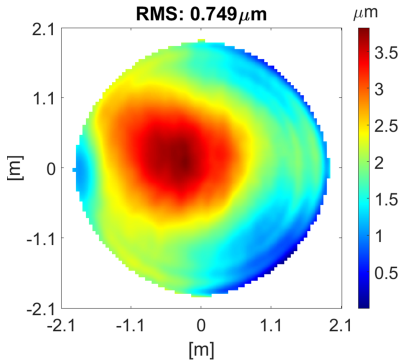


Fig. 4. Target removal map for CCOS simulation. RMS of surface figure error is 0.749 μm.

Three different TIFs were used for the simulation. The radius of orbital stroke TIFs [29] were 100 mm (TIF 1), 250 mm (TIF 2), and 400 mm (TIF 3) respectively. Due to the limited overhang ratio, we assumed that TIF 2 and 3 cannot travel farther than 100 mm (8 pixels) from the edge.

Defining the proper range of our parameters and hyperparameters are important to induce the desired result from GEANS. It is worthy to note that the used range of optimization parameters and hyperparameters can be varied upon the CCOS circumstances of users based on their target removal map, practical limitations (*e.g.* maximum tool size and weight), available polishing resources (*e.g.* sufficient and stable polishing compound supply chain, available pitch types), or achievable machining specifications (*e.g.* maximum motor speed, gear wear). For hyperparameters related to GA, we set the maximum generation number to 20, and each generation consists of 50 chromosomes. Among 50 chromosomes, 5 chromosomes were from the previous generation which scores high, 30 chromosomes were children that formed through crossover with a random multiplication rate of 0.3, and 15 chromosomes were new immigrants.

Domains of parameters illustrated in Section. 3.1 is another critical part to improve the performance of GEANS, yet the general solutions do not exist. In this simulation, we set the domains of each parameter empirically as summarized in Table 1.

As the smallest TIF (TIF 1) is dedicated to edge area only, we take into account the SSIM index of TIF 2 and 3 in the fitness function. Although multiple TIF sizes will be optimized simultaneously in GEANS, the actual polishing runs will remain sequential (*e.g.*, from larger to smaller tool sizes). We set higher weight to the TIF 3 than TIF 2 in the simulation. The fitness function we used here is

$$Q(FE, S_3, S_2) = \frac{FE + 5 \cdot S_3 + 2 \cdot S_2}{8} \tag{12}$$

The simulations were performed with MATLAB verison 2021a on a desktop equipped with AMD Ryzen 9 3950X (16 cores, 3.5 GHz) and 128 GB RAM.

Table 1. Ranges of parameters to be optimized through GA. These values are determined empirically. Numbers in brackets represent the range of each parameter. For example, [5:5:30] means [minimum : steps : maximum].

	TIF 1	TIF 2, 3
P^1 (px.)	[5:5:30]	
P^2 (px.^{2})	[1000:200:2000]	[20000:20000:120000]
P^3 (px.)	[13×13]:[4×4]:[29×29]	
P^4 (px.)	[1:1:4]	
P^5 (px.)	[5:5:30]	N.A

4.2. Simulation results

4.2.1. Simulation result from CNS

We baseline our performance with the results of the CNS algorithm. In the simulation, we assume the dwell points are equal to the sampling points, and the raster tool path is used while this can be any other tool path (*e.g.*, spiral) according to the actual machine's configuration. Note that the CCOS simulation conditions were mostly identical between CNS and GEANS except for the constraints of TIF 1 and the spatial resolution of data. Due to the high memory occupation, we needed to use less sampled data that has half the spatial resolution (171 by 171) in CNS. The computing efficiency between algorithms is summarized at Table 2 in the following chapter.

Table 2. Computing speed comparison between GEANS and CNS.

Method	Map size [px.]	Size of $\mathbf{t_{m\times n}}$	$m \times n$	Computation [s]	FE [%]
GEANS	341 × 341	72641×3681	267,391,521	Single: 24.4 Total: 22,082	94.3
GEANS (Low samp.)	171 × 171	18317×3898	71,399,666	Single: 4.9 Total: 4,437	94.4
CNS (Low samp.)	171 × 171	18317×51423	941,915,091	5,131	98.0

Figure 5 shows the dwell time maps of each TIF and remaining error map after applied each dwell time map from CNS method. In this simulation, we assumed TIFs were applied sequentially from TIF 3 to TIF 1. The adjusted alignment amounts for CNS were $-0.86\ \mu m$ of piston, $6.57 \times 10^{-5} mrad$ in x-tilt and $-3.04 \times 10^{-4} mrad$ in y-tilt. The RMS of residual surface error (Fig. 5(f)) is about 15 *nm* which corresponds to 98 % of FE. Although CNS shows very high FE, the outcome dwell time maps have several point-like, disconnected spots (top row of Fig. 5). These dwell time maps are not preferred in actual CCOS running because the machine requires high acceleration and deceleration. It usually requires the post-processing to translate dwell time maps into affordable machine motion, and it induces the unexpected error on final outcome. Besides, the dwell time maps barely followed the shape of target removal map, so that the risk of inducing unexpected spatial frequency errors on residual surface is high. Therefore the results from CNS have limited potential for practical implementation.

4.2.2. Simulation result from GEANS

Figure 6 shows the result of GEANS. Similar to CNS, the dwell points were equal to the sampling points. In GEANS, however, the smallest tool (TIF 1) only covers the area determined by $\boldsymbol{P^5}$ as illustrated at Section. 3.2, and the sampling interval is 12.5 *mm* which yields double resolution of CNS. After optimization the RMS of the residual surface error was 0.043 μm which corresponds to 94.3% of FE. Adjusted alignment amounts were $-1.26\ \mu m$ of piston, $-1.46 \times 10^{-6} mrad$ in x-tilt and $1.79 \times 10^{-5} mrad$ in y-tilt. Compared to CNS, the FE value was dropped 3.7 percentage points but still reasonably high FE. In terms of similarity of dwell time map, dwell time map of

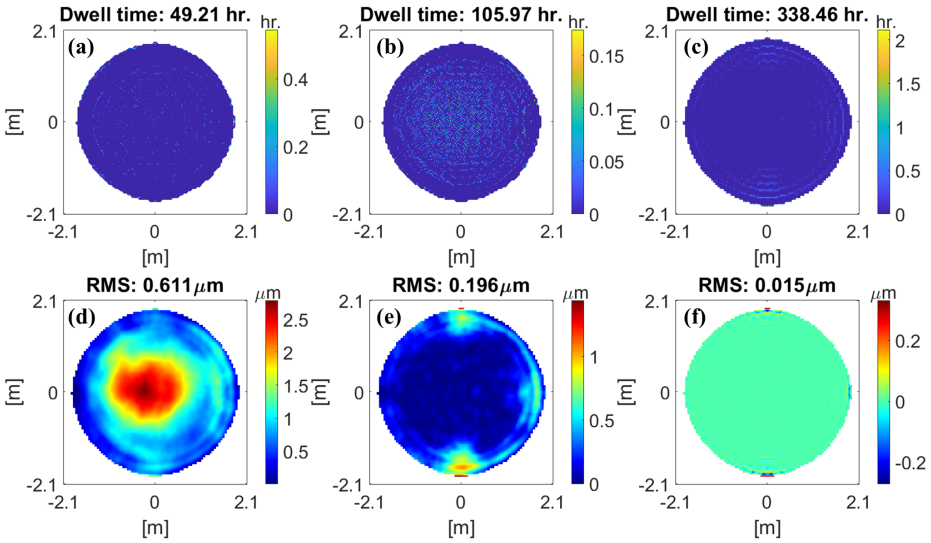


Fig. 5. CNS results dwell time maps and residual error maps. Dwell time map of (a) TIF 3 (b) TIF 2 and (c) TIF 1. Surface error maps after applying (d) TIF 3 (e) TIF 2 and (f) TIF 1 sequentially. Residual surface figure error after CNS was about about 15 *nm*.

TIF 3 (Fig. 6(a)) and 2 (Fig. 6(b)) closely replicate the shape of target removal map (Fig. 4) as we intended. The SSIM indices of each tool are 0.91 for TIF 3 and 0.85 for TIF 2.

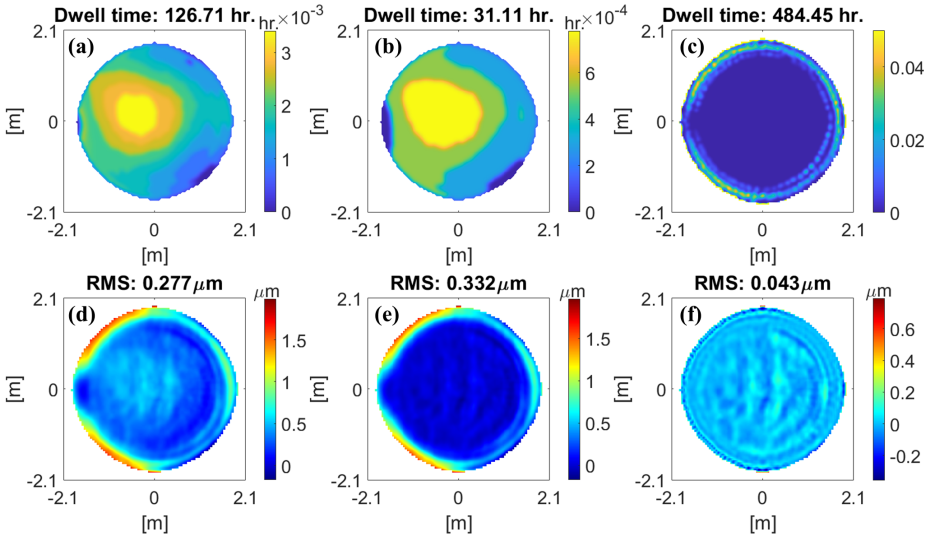


Fig. 6. Resulted maps from GEANS. Dwell time maps of (a) TIF 3 (b) TIF 2 (c) TIF 1. Residual surface error maps after applying (d) TIF 3 (e) TIF 2 and (f) TIF 1 in sequentially. Residual error map of GEANS was 43 *nm* of RMS.

Figure 7 shows how the fitness function, RMS of residual surface error, and similarity of TIF 2 and 3 were changed over 20 generations. The RMS and similarity values were from the chromosome which has the highest score in that generation. Though the RMS of the residual

map and both SSIM do not monotonically decrease or increase, the fitness function increases as the generations pass.

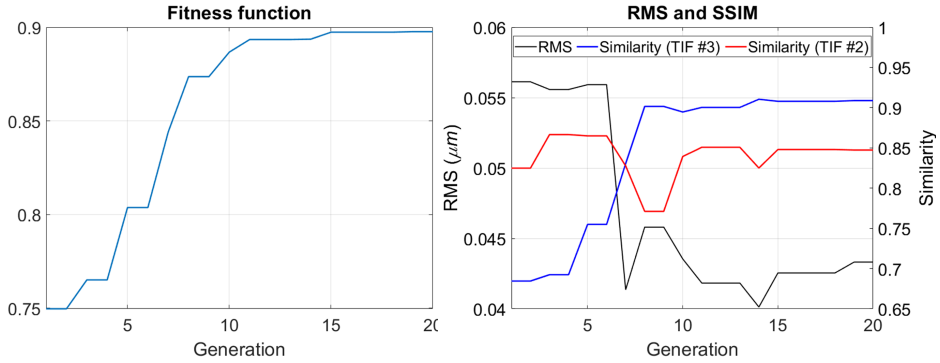


Fig. 7. (Left) Fitness function value over 20 generations of evolving. (Right) RMS of remained surface error and S_2 and S_3 of each generations. The transformation of TIF 3 over generations is shown in Visualization 1.

4.3. Validation of GEANS

Compared to CNS, GEANS shows enhanced practicality of dwell time maps through three main features: building the influence matrix, smoothing dwell time maps, and employing SSIM index to make dwell time map to copy the shape of target removal map. In this chapter, we analyze how these aspects affect GEANS's performance.

Since GEANS utilized a GA that requires large number of repeated optimization calculations, improved computing efficiency was essential. By grouping and dividing, GEANS cuts down the size of elements of the influence function ($\mathbf{t}$) to more than 10 times smaller than CNS at the same resolution (Table 2) while maintaining enough degrees of freedom in optimization for figuring efficiency. As a result, GEANS shows 1000 times optimization speed increase for a single optimization on average. The total calculation time was shorter yet, as GEANS required 905 (50 times from the first generation, and 45 times from the rest generations) iterative optimizations. It also enables us to use higher resolution data which benefits in large optics fabrication. Even with higher resolution, the size of influence matrix of GEANS is smaller so that the single computation took still less time than CNS.

Smoothing with Gaussian filtering also increased practicality of dwell time maps from GEANS. Figure 8 shows the resulted dwell time map of TIF 3 from GEANS when smoothing was applied (Fig. 8(a)) and was not (Fig. 8(b)). Without smoothing, the slope of dwell time change was abruptly between adjacent well points. Further the dwell time map was less similar ($S_3 = 0.59$) to the shape of target removal map than GEANS result ($S_3 = 0.91$).

SSIM also has an important role to produce desirable dwell time map in GEANS. Figure 9 shows the obtained dwell time maps of TIF 3 with and without SSIM index in the fitness function. Without SSIM (Fig. 9(b)), dwell time map is not duplicating the target removal map noticeably. Besides, some dwell points were not linked together and slope of dwell time map is steep which causes inessential acceleration of tool (Fig. 9(c)).

4.4. Error analysis of dwell time maps

Simulation results are degraded while applying in actual CCOS process due to various error sources which include tool positioning error, random variation in TIF, limited acceleration of

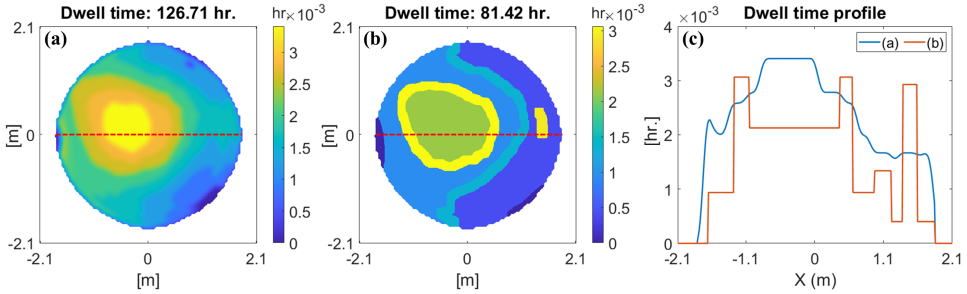


Fig. 8. Comparison of dwell time map to show smoothing affects. Dwell time map of TIF 3 are shown here. (a) GEANS (b) GEANS without smoothing. (c) Center line profile (Red dotted lines in (a) and (b)) of each dwell time map.

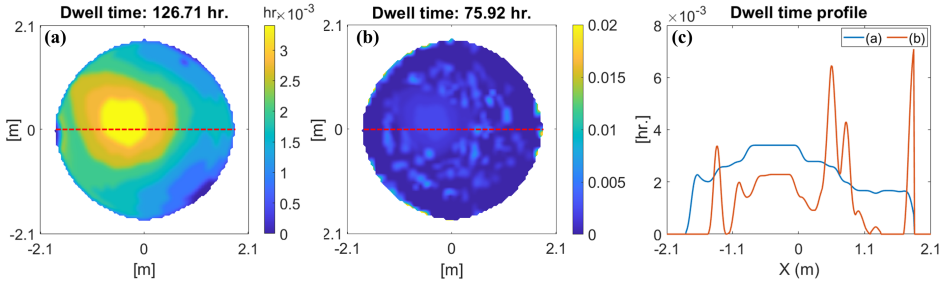


Fig. 9. Dwell time maps of TIF 3 when SSIM was (a) considered and (b) not considered in fitness function. Without SSIM, the resulted dwell time map was neither copying the shape of target removal map and smoothly continuous. (c) Center line profile (Red dotted lines in (a) and (b)) of each dwell time map.

tool, or laboratory environment. Considering these factors, we implemented robustness test to compare the stability and usability of dwell time maps from GEANS and CNS.

First, we imposed random errors to dwell position and TIF and checked how the Power Spectral Density (PSD) is changed. Both random error had rectangular distribution function of which boundary values were up to ±10 *mm* for tool positioning errors and ±10% for TIF value errors. Within the boundary, random errors were added or subtracted from the original dwell time. Figure 10 shows the variation of PSD with perturbations. Without error (thick blue lines in the figure), the CNS method (Fig. 10(b)) shows lower PSD in overall frequency than GEANS (Fig. 10(a)). However, with perturbations, PSD of CNS was changed and distributed broadly while PSD of GEANS was remained stable. These results implied that GEANS result is more predictable and robust against to the given errors so that more applicable than CNS in actual CCOS operation.

We then evaluated applicability of dwell time maps from each method. In actual CCOS running, since the maximum acceleration of tool is limited, dwell time maps that have smooth slopes along tool path are preferred and feasible solutions. Especially in large optics fabrication, as the sizes of tools are larger, controlling the tool acceleration is getting more difficult. Figure 11 is a histogram showing distribution of dwell time slopes of TIF 2 and TIF 3 from GEANS and CNS. As expected, slopes of CNS were higher than GEANS in general.

We investigated how the limited acceleration affects the residual error map. We employed the continuous raster motion tool path, and set limits in dwell time difference along the path. If the difference is larger than the set limit, the dwell time limit is added or subtracted to an adjacent

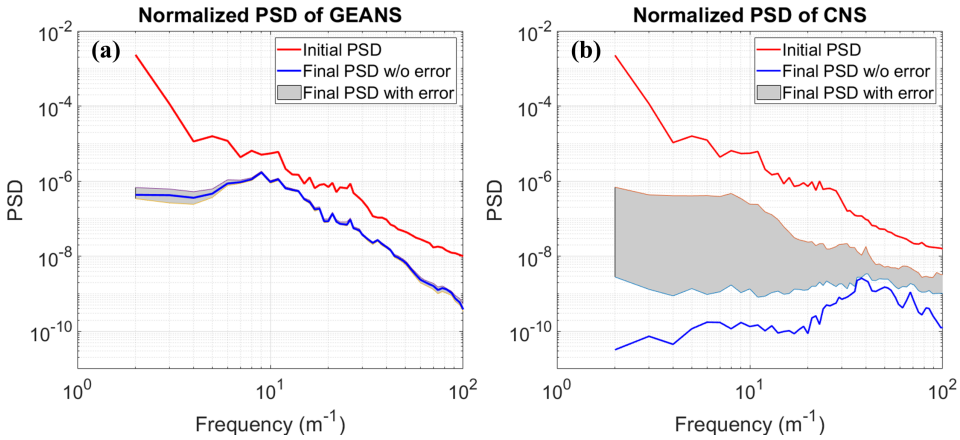


Fig. 10. Compared PSD of remained surface error map after considering practical operation of (a) GEANS method and (b) CNS method. PSD of GEANS was remained steady while the PSD of CNS was worsened with perturbation.

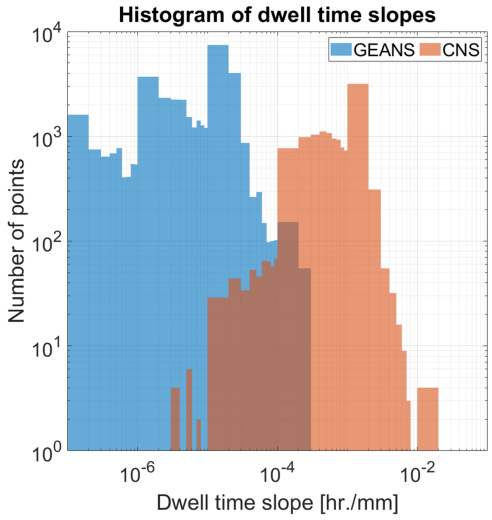


Fig. 11. Histogram of dwell time slopes. X and Y axis are represented in log-scale. This different distribution in slopes of each method implies that the required maximum acceleration for GEANS is lower than CNS.

dwell point along the tool path until every difference is under the limit. Assuming the TIF 1 can have higher acceleration, this adjustment is applied to TIF 2 and 3.

We applied various slope limitations from 10^{-2} $mm/hour$ to 10^{-5} $mm/hour$ and analyzed how the dwell time maps and residual maps were changed. Figure 12 shows how the dwell time map of TIF 3 is changed when the maximum slope is limited to 0.001 $mm/hour$. In CNS, compared to the original map (Fig. 12(a)), dwell points with steep slopes were elongated and in consequence total dwell time was increased (Fig. 12(b)). GEANS, on the other hand, had no change in dwell time maps from the initial results since most of dwell points were already within the limit (Fig. 12(c), (d)).

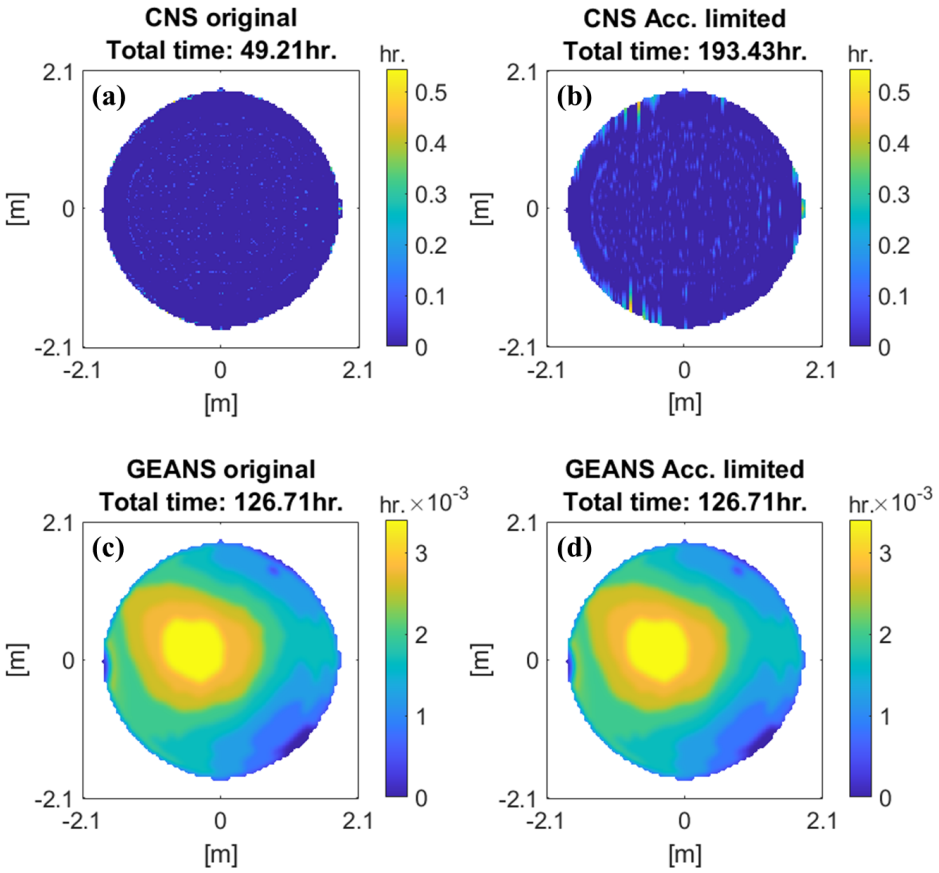


Fig. 12. Variation of dwell time map when the acceleration limit (0.001 $mm/hour$) is applied. (a) Original dwell time map of TIF 3 from CNS and (b) Dwell points with high slopes were adjusted. As dwell time map was smoothed, total dwell time was extended as well. (c) Original dwell time map of TIF 3 from GEANS. (d) Slope limitation was applied but no difference in dwell time map.

The variation in dwell time maps, of course, affect to the final CCOS results as well. Figure 13 shows how the residual error map changed due to acceleration limitations. The FE of CNS was rapidly worsening because the dwell time maps could not be applied as optimized yet the results fron GEANS remained stable. The effects of other maximum slope cases are shown in Visualization 2 for GEANS case and Visualization 3 for CNS case.

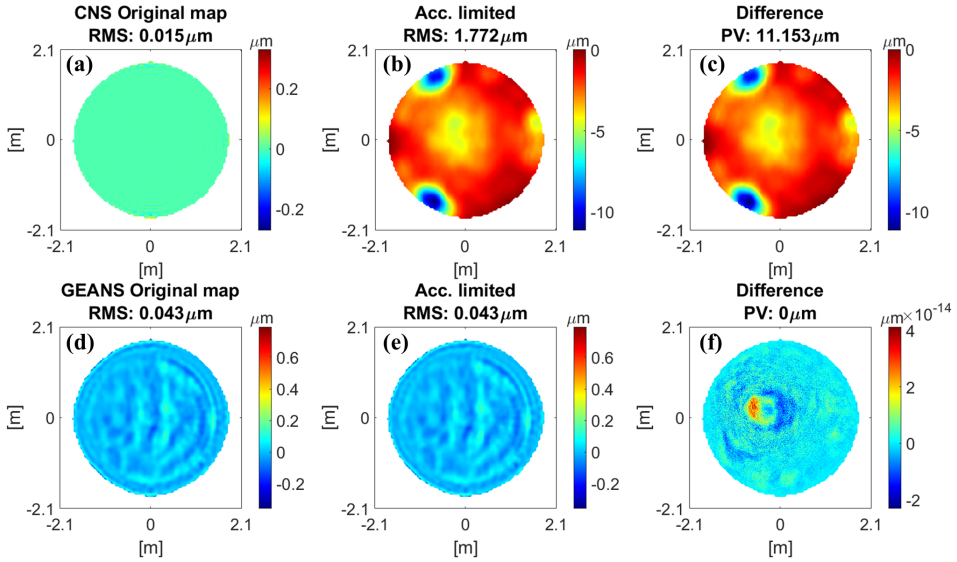


Fig. 13. Changes of residual error map when the acceleration limit was applied. (a) Original result from CNS. (b) Residual map when maximum acceleration was applied (CNS). (c) Difference map between (a) and (b). (d) Original result from GEANS. (e) Residual map when maximum acceleration was applied (GEANS). (f) Difference map between (d) and (e).

5. Discussion

The increased residual RMS and total dwell time in GEANS compared to CNS. It is also worth mentioning that, although CNS showed better initial results than GEANS in simulation, the results from CNS have limited potential for practical implementation as the results from CNS are very sensitive to common errors in CCOS process (*e.g.* tool positioning, TIF model accuracy) or machine capabilities (*e.g.* tool acceleration limits). For example, the total dwell times of each CNS (Fig. 5) and GEANS (Fig. 6) were 494 hour and 642 hour respectively. Also the residual RMS of CNS (0.015 μm) was lower than that of GEANS (0.043 μm). However, with machining errors, the outcome from CNS is less predictable than that of GEANS (Fig. 10). Further, when we consider the limit in tool acceleration as shown in Figs. 12, 13 and Visualization 3, the total run time of CNS will be increased notably as well as the estimated residual RMS unless the CCOS machine can meet the rapid motion limit which is not easy to be achieved especially for large optics fabrication tools.

6. Conclusion

In this paper, we proposed a novel dwell time optimization method called GEANS (Genetic algorithm-powered non-sequential), which can combine the modern numerical optimization computing power and the skilled human expert's brain power (*e.g.*, optician's intuitive dwell time estimation). To provide practical and applicable dwell time map solution, we built an influence matrix through grouping, dividing, and smoothing procedures. In this process, excessive number of parameters were needed to be optimized such as criteria of grouping and dividing, and the size of Gaussian smoothing filter. However, the correlation between parameters and final dwell time map was not easy to identify mathematically. Therefore, we employed genetic algorithms to find optimal parameters associated with influence matrix. The performance of GEANS was demonstrated with CCOS simulation using the real surface error map and TIF data. Compared

to CNS, GEANS achieved comparable FE (94.3 %) and 1000 times faster computation speed. Further, the result dwell time maps were closely reproduced the shape of target removal map which are preferable in actual CCOS running. Error analyses were also performed to demonstrate the stability and applicability of each algorithm. Up to 10 *mm* of tool position and 10 % of TIF were perturbed and checked impact in PSD. Results showed that dwell time maps from GEANS were remarkably more practicable and stable than those of CNS in given perturbations. We also applied maximum achievable tool acceleration and examined how dwell time maps and final residual surface error maps were changed. The GEANS dwell time maps were smooth and continuous compared to CNS, which allowed much slower tool acceleration to complete calculated dwell time maps.

We believe that the flexibility and capability of being expanded adds more unique value to GEANS. The optimizing parameters can be included or withdrawn depending on the achievable system conditions. Further, beyond the dwell time, other CCOS items such as the tool path or types of TIF also can be optimized while reflecting the priorities of CCOS result in GEANS.

Acknowledgments. We also want to thank the people who contributed to the editing and reviewing of the manuscript. A special thank you goes to Jaren Ashcraft and Henry Quach who helped edit and gave feedback on the article.

Disclosures. The authors declare no conflicts of interest.

Data availability. Data underlying the results presented in this paper are not publicly available at this time but may be obtained from the authors upon reasonable request.

References

1. R. Aspden, R. McDonough, and F. R. Nitchie, "Computer assisted optical surfacing," Appl. Opt. **11**(12), 2739–2747 (1972).
2. R. Wagner and R. Shannon, "Fabrication of aspherics using a mathematical model for material removal," Appl. Opt. **13**(7), 1683–1689 (1974).
3. R. A. Jones, "Computer-controlled polishing of telescope mirror segments," Opt. Eng. **22**(2), 222236 (1983).
4. R. A. Jones, "Computer-controlled optical surfacing with orbital tool motion," Opt. Eng. **25**(6), 256785 (1986).
5. R. A. Jones and W. J. Rupp, "Rapid optical fabrication with CCOS," in *Advanced Optical Manufacturing and Testing*, vol. 1333 G. M. Sanger, P. B. Reid, and L. R. Baker, eds., International Society for Optics and Photonics (SPIE, 1990), pp. 34–43.
6. H. Pollicove and D. Golini, "Deterministic manufacturing processes for precision optical surfaces," in *Key Engineering Materials*, vol. 238 (Trans Tech Publ, 2003), pp. 53–58.
7. J. H. Burge, S. Benjamin, D. Caywood, C. Noble, M. Novak, C. Oh, R. Parks, B. Smith, P. Su, M. Valente, and C. Zhao, "Fabrication and testing of 1.4-m convex off-axis aspheric optical surfaces," in *Optical manufacturing and testing VIII*, vol. 7426 (International Society for Optics and Photonics, 2009), p. 74260L.
8. M. J. Valente, D. W. Kim, C. J. Oh, M. J. Novak, and J. H. Burge, "Fabrication of 4-meter class astronomical optics," in *Modern Technologies in Space- and Ground-based Telescopes and Instrumentation*, vol. 7739 E. Atad-EttedguiD. Lemke, eds., International Society for Optics and Photonics (SPIE, 2010), pp. 880–892.
9. M. Johns, "The giant magellan telescope (gmt)," in *Ground-based and Airborne Telescopes*, vol. 6267 (International Society for Optics and Photonics, 2006), p. 626729.
10. J. Nelson and G. H. Sanders, "The status of the thirty meter telescope project," in *Ground-based and Airborne Telescopes II*, vol. 7012 (International Society for Optics and Photonics, 2008), p. 70121A.
11. T. Andersen, A. L. Ardeberg, J. Beckers, A. Goncharov, M. Owner-Petersen, H. Riewaldt, R. Snel, and D. Walker, "The euro50 extremely large telescope," in *Future Giant Telescopes*, vol. 4840 (International Society for Optics and Photonics, 2003), pp. 214–225.
12. A. Ardeberg, T. Andersen, J. Beckers, M. Browne, A. Enmark, P. Knutsson, and M. Owner-Petersen, "From euro50 toward a european elt," in *Ground-based and Airborne Telescopes*, vol. 6267 (International Society for Optics and Photonics, 2006), p. 626725.
13. R. A. Jones, "Optimization of computer controlled polishing," Appl. Opt. **16**(1), 218–224 (1977).
14. C. Wang, W. Yang, Z. Wang, X. Yang, C. Hu, B. Zhong, Y. Guo, and Q. Xu, "Dwell-time algorithm for polishing large optics," Appl. Opt. **53**(21), 4752–4760 (2014).
15. S. Wilson and J. McNeil, "Neutral ion beam figuring of large optical surfaces," in *Current Developments in Optical Engineering II*, vol. 818 (1987), pp. 320–325.
16. T. Wang, L. Huang, H. Kang, H. Choi, D. W. Kim, K. Tayabaly, and M. Idir, "RIFTA: A Robust Iterative Fourier Transform-based dwell time Algorithm for ultra-precision ion beam figuring of synchrotron mirrors," Sci. Rep. **10**(1), 8135 (2020).

Optics EXPRESS

17. T. Wang, L. Huang, H. Choi, M. Vescovi, D. Kuhne, Y. Zhu, W. C. Pullen, X. Ke, D. W. Kim, Q. Kemao, K. Tayabaly, N. Bouet, and M. Idir, "Rise: robust iterative surface extension for sub-nanometer x-ray mirror fabrication," Opt. Express **29**(10), 15114–15132 (2021).
18. C. L. Carnal, C. M. Egert, and K. W. Hylton, "Advanced matrix-based algorithm for ion-beam milling of optical components," in *Current Developments in Optical Design and Optical Engineering II*, vol. 1752 (1992), pp. 54–63.
19. D. W. Kim, S.-W. Kim, and J. H. Burge, "Non-sequential optimization technique for a computer controlled optical surfacing process using multiple tool influence functions," Opt. Express **17**(24), 21850–21866 (2009).
20. J. F. Wu, Z. W. Lu, H. X. Zhang, and T. S. Wang, "Dwell time algorithm in ion beam figuring," Appl. Opt. **48**(20), 3930–3937 (2009).
21. T. Wang, L. Huang, M. Vescovi, D. Kuhne, K. Tayabaly, N. Bouet, and M. Idir, "Study on an effective one-dimensional ion-beam figuring method," Opt. Express **27**(11), 15368–15381 (2019).
22. P. Ji, D. Li, X. Su, Z. Qiao, K. Wu, L. Song, B. Peng, and B. Wang, "Optimization strategy for the velocity distribution based on tool influence function non-linearity in atmospheric pressure plasma processing," Precis. Eng. **65**, 269–278 (2020).
23. A. Chernyshev, N. Chkhalo, I. Malyshev, M. Mikhailenko, A. Pestov, R. Pleshkov, R. Smertin, M. Svechnikov, and M. Toropov, "Matrix based algorithm for ion-beam figuring of optical elements," Precis. Eng. **69**, 29–35 (2021).
24. T. Wang, L. Huang, M. Vescovi, D. Kuhne, Y. Zhu, V. S. Negi, Z. Zhang, C. Wang, X. Ke, H. Choi, W. C. Pullen, D. Kim, Q. Kemao, K. Nakhoda, N. Bouet, and M. Idir, "Universal dwell time optimization for deterministic optics fabrication," Opt. Express **29**(23), 38737–38757 (2021).
25. C. Jiao, S. Li, and X. Xie, "Algorithm for ion beam figuring of low-gradient mirrors," Appl. Opt. **48**(21), 4090–4096 (2009).
26. H. Martin, R. Allen, J. Burge, D. Kim, J. Kingsley, M. Tuell, S. West, C. Zhao, and T. Zobrist, "Fabrication and testing of the first 8.4-m off-axis segment for the giant magellan telescope," in *Modern Technologies in Space-and Ground-based Telescopes and Instrumentation*, vol. 7739 (International Society for Optics and Photonics, 2010), p. 77390A.
27. J. H. Burge, D. W. Kim, and H. M. Martin, "Process optimization for polishing large aspheric mirrors," in *Advances in Optical and Mechanical Technologies for Telescopes and Instrumentation*, vol. 9151 (International Society for Optics and Photonics, 2014), p. 91512R.
28. C. J. Oh, A. E. Lowman, G. A. Smith, P. Su, R. Huang, T. Su, D. Kim, C. Zhao, P. Zhou, and J. H. Burge, "Fabrication and testing of 4.2 m off-axis aspheric primary mirror of daniel k. inouye solar telescope," in *Advances in Optical and Mechanical Technologies for Telescopes and Instrumentation II*, vol. 9912 (International Society for Optics and Photonics, 2016), p. 99120O.
29. D. W. Kim and S.-W. Kim, "Static tool influence function for fabrication simulation of hexagonal mirror segments for extremely large telescopes," Opt. Express **13**(3), 910–917 (2005).
30. J. H. Holland, *Adaptation in natural and artificial systems: an introductory analysis with applications to biology, control, and artificial intelligence* (MIT press, 1992).
31. K. A. De Jong, *An analysis of the behavior of a class of genetic adaptive systems*. (University of Michigan, 1975).
32. Z. Wang, A. C. Bovik, H. R. Sheikh, and E. P. Simoncelli, "Image quality assessment: from error visibility to structural similarity," IEEE Trans. on Image Process. **13**(4), 600–612 (2004).

150.135.165.9 {ts '2022-04-28 11:58:45'}

APPENDIX B

Computational vector fiducial for deflectometry system alignment

Hyukmo Kang, Henry Quach, Joel Berkson, Maham Aftab, George Smith, Heejoo Choi, and Daewook Kim

Journal article published at ***Optics Letters***

Copyright Transfer Agreement Opt. Lett. 46(22), 5571-5574 (2021). Copyright Optical Society of America. Reprinted with permission.

Letter Vol. 46, No. 22 / 15 November 2021 / Optics Letters 5571

Optics Letters

Computational vector fiducial for deflectometry system alignment

Hyukmo Kang,[1] Henry Quach,[1] Joel Berkson,[1] Maham Aftab,[1] George Smith,[1] Heejoo Choi,[1,2] and Daewook Kim[1,2,3,*]

[1]Wyant College of Optical Sciences, University of Arizona, 1630 E. University Blvd., Tucson, Arizona 85721, USA
[2]Large Binocular Telescope Observatory, 933 N. Cherry Ave., Tucson, Arizona 85721, USA
[3]Department of Astronomy and Steward Observatory, University of Arizona, 933 N. Cherry Ave., Tucson, Arizona 85721, USA
*Corresponding author: dkim@optics.arizona.edu

Received 3 September 2021; revised 4 October 2021; accepted 17 October 2021; posted 18 October 2021 (Doc. ID 442223); published 4 November 2021

One of deflectometry's cardinal strengths is its ability to measure highly dynamically sloped optics without needing physical null references. Accurate surface measurements using deflectometry, however, require precise calibration processes. In this Letter, we introduce an alignment technique using a computational fiducial to align a deflectometry system without additional hardware equipment (i.e., algorithmic innovation). Using the ray tracing program, we build relationships between the plane of the screen and detector and algorithmically generate a fiducial pattern for the deflectometry configuration. Since the fiducial pattern is based on ideal system geometry, misalignment of the unit under test with its target position causes a discrepancy between the actual image on the camera detector and the ideal fiducial image. We leverage *G* and *C* vector polynomials to quantify misalignment and estimate the alignment status through a reverse optimization method. Simulation and experimental results demonstrate that the proposed algorithm can align the 195 mm × 80 mm of a rectangular aperture freeform optic within 10 μm of peak-to-valley accuracy. The computational fiducial-based alignment algorithm is simple to apply and can be an essential procedure for conventional methods of deflectometry system alignment. © 2021 Optical Society of America

https://doi.org/10.1364/OL.442223

The demand for freeform metrology remains commensurate with the growing demand for freeform optics in high-performance systems. Deflectometry is an attractive solution in this metrology solution space because it possesses a large dynamic slope-measuring range and does not require null optics [1,2]. These features enable a single deflectometry system to measure various types of optical surfaces without extensive changes.

Without significant effort for pre-alignment, deflectometry can measure the optics, but reliable calibration and alignment are critical for accurate surface slope measurement. To determine the positions of deflectometry system components, external measuring devices such as coordinate measuring machines or laser trackers can be used [2,3]. Additionally, calibration techniques utilizing reference features with known surfaces [4–8], employing Zernike polynomial to analyze misalignment [9–11], or minimizing differences between model and observed geometric parameters through iterative calculation [12–14] are studied by various researchers to calibrate the deflectometry system or align optical surfaces.

In this Letter, we introduce an alignment algorithm for deflectometry systems using an inversely calculated computational fiducial and demonstrate it in both simulation and experiments. This method is analogous to an interferometer's alignment mode, which guides users to overlap two focused spots from the reference beam and the test beam. The presented algorithm leveraged ***G*** and ***C*** vector polynomials [15,16] to quantify the alignment status and calculate the misalignment using reverse optimization. Especially, the inverse ray tracing calculation creates uniformly distributed fiducial grid spots on the deflectometry camera image. This algorithmic innovation enables systematic vector polynomial fitting on the measured spots to solve the alignment problem of a non-null testing nature (e.g., configuration dependent complex sinusoidal patterns). The alignment quality was evaluated using optical testing criteria to illustrate its sensitivity and utility in metrology applications.

A deflectometry system consists of an illumination source, a unit under test (UUT), and a camera (Fig. 1). Typically a digital screen is used as the illumination source, and the camera is focused on the UUT to establish conjugate imaging between the camera detector and the UUT. By modulating the displayed phase-stepped sinusoidal patterns and calculating phase at the image detector, a pixel-to-pixel correspondence among the screen, UUT, and detector is obtained. Using the coordinate information of all associated data and the law of reflection, deflectometry calculates the local slope distribution of UUT [1].

The deflectometry ray tracing simulator [17] provides coordinate relationships among the screen, UUT, and detector pixels. This feature is used to inversely generate the computational fiducial pattern to assist alignment of the deflectometry setup. The fiducial pattern is a specific pattern displayed on the screen that maps a grid dot image onto the camera detector. In Fig. 2(a),

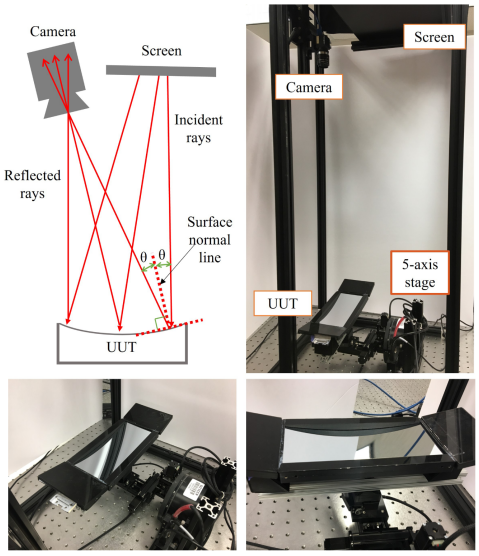


Fig. 1. (top left) Schematic diagram of deflectometry setup. The light source (screen) emits rays that are reflected at the UUT and collected by the camera. (top right) Experimental setup of deflectometry. (bottom left) UUT mounted on the computer-controlled rigid-body motion stage. (bottom right) Zoom-in view of the freeform UUT.

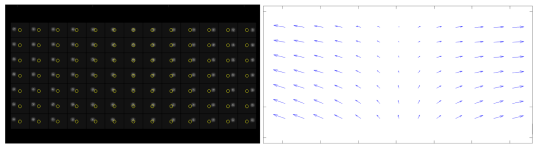


Fig. 2. Simulated images for computational fiducial pattern application. (a) Observed image of fiducial pattern at the detector plane. White dots are measured patterns and yellow circles are fiducial from model. (b) Vector map drawn from computational yellow circles to measured white dots, which are updated real-time.

the yellow circles are the locations of the fiducial for a perfectly aligned system, the recorded white dots mark their observed locations, and the gray squares are equally distributed areas for each zonal analysis. Each dot is 2D Gaussian shape to reduce the ambiguity in position determination. Since this pattern is calculated based on model geometry parameters, any deviation from the fiducial points implies an inconsistency in the geometry parameters between the model and the experimental setup. It is worthy to note that, if a surface shape error is in a way that it produces the same vector fiducial changes as a misalignment, such fundamental degeneracy cannot be distinguished. The rectangular grid dot pattern is also preferable to utilize $\boldsymbol{G}$ and $\boldsymbol{C}$ polynomials sets that are introduced in the following paragraphs.

The fiducial dot pattern can be used to systematically quantify the misalignment status when it is associated with vector polynomials. As misalignments shift the image of the fiducial dots from their reference points, we can connect corresponding dots from their referenced position to their perturbed position to make vectors [Fig. 2(b)].

$\boldsymbol{G}$ and $\boldsymbol{C}$ polynomial sets are vector polynomials derived from the two-dimensional Chebyshev polynomials [15,16]. The $\boldsymbol{G}$ polynomial set is derived from the gradients of the two-dimensional Chebyshev polynomials of the first kind, and the $\boldsymbol{C}$ polynomial set is based on the curl of two-dimensional Chebyshev polynomials of the first kind. Since both $\boldsymbol{G}$ and $\boldsymbol{C}$ polynomials are orthogonal sets in the rectangular domain, specific vector terms can be directly related to system errors in alignment of the UUT. While $\boldsymbol{G}$ and $\boldsymbol{C}$ vector polynomials are utilized in this Letter, the general computational vector fiducial method can be used with any other vector polynomials to be used for different UUT aperture shape applications (e.g., Zernike-based vector polynomials defined over a circular domain).

The reverse optimization algorithm (Eq. 1) is widely used to align optical systems [18,19]:

$$\boldsymbol{A} = \boldsymbol{S}\Delta\boldsymbol{D},$$

$$\boldsymbol{A} = [a_1 \ldots a_i]^T, \quad \boldsymbol{S}_{ij} = \frac{\delta a_i}{\delta x_j}, \quad \Delta\boldsymbol{D} = \boldsymbol{x}_j - \boldsymbol{x}_{jo}. \tag{1}$$

This algorithm consists of three matrices as follows: (1) the measured $\boldsymbol{G}$ and $\boldsymbol{C}$ polynomial coefficients ($\boldsymbol{A}$), (2) sensitivity ($\boldsymbol{S}$), and (3) the amount of misalignment ($\Delta\boldsymbol{D}$) displacement of each degree of freedom between the current position ($\boldsymbol{x}_j$) and target position ($\boldsymbol{x}_{jo}$). Sensitivity means how much the $\boldsymbol{G}$ and $\boldsymbol{C}$ polynomial coefficients are changed when the system is perturbed by a unit amount in each degree of freedom. The sensitivity can be determined through simulation or actual measurements at each location. After the sensitivity matrix is determined, the misalignment can be calculated using least square fitting from the measured coefficients [Eq. (2)]. This algorithm provides an accurate solution when the sensitivity is linear to the misalignment and the degrees of freedom are orthogonal to each other:

$$\Delta\boldsymbol{D} = (\boldsymbol{S}^T\boldsymbol{S})^{-1}\boldsymbol{S}^T\boldsymbol{A}. \tag{2}$$

The performance of the algorithm is verified through simulation and a physical alignment experiment. First the sensitivity was investigated by moving the UUT by a known amount. Random misalignments were then imposed to the UUT's position, and vector data of the fiducial displacements were collected. The set of vector data was then fitted to the $\boldsymbol{G}$ and $\boldsymbol{C}$ polynomials, and the amount of misalignment was calculated through a reverse optimization process. These processes were repeated until the criteria were met (Fig. 3).

A freeform optic with 2.99 mm peak-to-valley (PV) aspheric departure within a rectangular aperture is used for the simulation study (Fig. 4). During the computational fiducial and its alignment mode generation process, the ideal deflectometry-and-UUT configuration is perturbed and misaligned in the simulation model.

We generated a 27 × 20 grid of 540 dots for vector sampling over the whole UUT aperture for the simulation. The investigated range of sensitivity was ±0.5 mm for translations and ±0.1° for tilts. The collected vector data were fitted to 100 terms of each $\boldsymbol{G}$ and $\boldsymbol{C}$ polynomial. Among the 100 coefficients, we selected the first 22 terms from each $\boldsymbol{G}$ and $\boldsymbol{C}$ polynomial

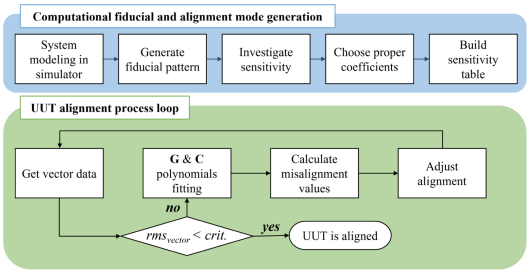


Fig. 3. Flowchart of the computational fiducial-based alignment procedure for simulation and physical experiment.

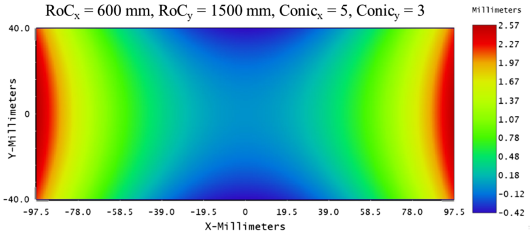


Fig. 4. Surface map of sag departure from best-fit sphere for the simulation.

coefficient as the alignment modes, a total of 44 coefficients to build the sensitivity matrix. To calculate the misalignment without degeneracy, each degree of freedom should have distinct sensitivities from one another. Hereafter, translation in x, y, and z axes are denoted as Dx, Dy, and Dz, and tilt about x, y, and z axes are denoted as Tx, Ty, and Tz, respectively. In general, Dx-Ty and Dy-Tx are coupled motions that show similar tendencies. Figure 5 shows the normalized sensitivity ratio of some representative coefficients that have high sensitivities among the used 44 terms. Their sensitivities resemble each other but have different ratios between coefficients to be distinguished as a unique set of alignment mode fingerprints. Considering these characteristics of the sensitivity matrix, we can expect that the misalignments would converge eventually in every degree of freedom with iterations (Fig. 3).

A total of 30 alignment simulations were performed, and the random alignment errors were imposed within the sensitivity investigated range. The alignment end criteria were 0.08 pixel of RMS vector size (0.2 μm in this case) at the image plane. Simulation results are shown in Fig. 6. Although the required

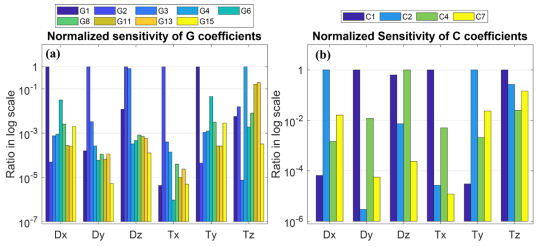


Fig. 5. (a) Normalized sensitivity of ***G*** coefficients. (b) Normalized sensitivity of ***C*** coefficients. Both graphs are represented in log scales due to small magnitudes of sensitivities.

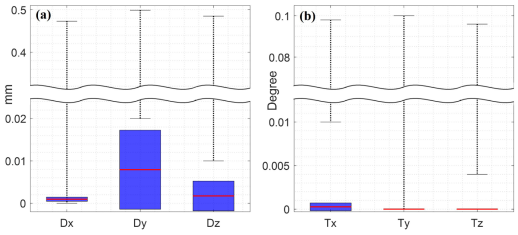


Fig. 6. Result of alignment simulation. Dotted lines mean initial random alignment error range, red lines represent mean values of remaining errors, and blue boxes represent standard deviations of each. (a) Translation errors. (b) Tilt errors.

number of alignment steps was varied, the RMS vector sizes were converged and met the criteria at the end. The remaining amounts of misalignments were reasonably small in all 6 deg of freedom. The remaining error for Dy was relatively higher than others (~8 μm), but still within an affordable range to have consistency in surface measurements with deflectometry.

Once the viability of the algorithm had been tested, it was applied to an experimental deflectometry setup (Fig. 1). A 546 mm LCD monitor with 1920 × 1080 resolution was utilized as the light source, and a 3.2 MP camera with a 16 mm focal length objective lens was mounted near the LCD monitor. The UUT we used was a freeform image projection mirror with a rectangular aperture with a width of 195 mm and height of 80 mm.

To track the alignment status precisely, we mounted the UUT on a five-axis motorized stage. (Note: the Tx was manually fixed due to the limited motorized hardware available in the laboratory.) The as-built vector fiducial alignment hardware system needs to be calibrated because the motion stage hardware, display, and camera are not ideal. It can be calibrated by aligning and measuring a reference UUT. Because the reference surface is known, after the alignment minimizing the surface residual error (i.e., difference between the measured and known surface shapes), the alignment state can be set as the nominal zero state, and the residual error can be calibrated out as systematic error.

Similar to the simulation process, the sensitivity matrix was investigated first. In this case, the UUT was translated ±0.5 mm along each axis, and tilted ±0.1° about the y and z axes. Then we fit the vector data into 100 terms of each ***G*** and ***C*** polynomial. The total measuring time for ***S*** was about 20 min, yet ~90% of the time was due to the series of image acquisition periods limited by the as-built motorized stage speed. We built the sensitivity table using the first 20 terms or more from each polynomial, and the alignment criteria were set to less than 0.3 pixel (0.75 μm) RMS for the vector size in the detector plane. Then, the random misalignments were imposed within the sensitivity investigated range, and the algorithm was applied to calculate the amount of misalignment. These processes were controlled automatically and calculated repeatedly in closed-loop until alignment criteria were met. A commercial laptop (CPU: i5-1135G7/RAM: 8 GB) was used for calculating and controlling the system, and each iteration took less than 2 min.

A total of 10 alignment experiments were performed, and results are summarized in Fig. 7. The RMS vector size met the criteria, but the remaining amounts of misalignments were various for each degree of freedom. Dy, Dz, and Tz converged

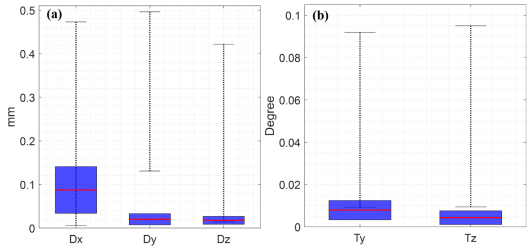


Fig. 7. Result of physical experiments. (a) Translation errors. (b) Tilt errors.

well, while Dx and Ty converged as well but had relatively large amounts of errors remaining. This is because Dx and Ty give the similar fiducial motion and are hard to distinguish in vector space.

We highlight that the performance of the alignment status estimation was limited by accuracy of the hardware, not the algorithm itself as long as the misalignment is within a linear range of sensitivity. Indeed, the coupled translation and tilt are already predicted from the simulation stage. As shown in Fig. 5, the translation and tilt motion have distinct behavior in higher order coefficients that are small in magnitude. For this reason, the accuracy of the algorithm can be improved by obtaining more precise vector data or utilizing higher resolution cameras in the deflectometry system. For application of a large misalignment case where misalignments are nonlinear, an adaptive or iteratively updating $\boldsymbol{S}$ throughout the alignment process can be applied. Then, updating $\boldsymbol{S}$ comes at the cost of modeling or measurement time.

Alignment in most metrology systems is important so that misalignment is not embedded into surface measurements. To validate alignment results, we compared the PV of the subtracted map between a reference surface map and a before/after aligned surface map. The reference is the surface map measured at the home position. Thus the difference map shows both the capability of the alignment loop to bring back the UUT to its original position and repeatability of optical testing. The PV surface map error due to the residual misalignment is less than 8.4 μm in 10 experiments (Fig. 8). The result demonstrated that the proposed computational alignment algorithm can guide deflectometry system alignment to secure repeatability in optical testing without additional alignment devices. This

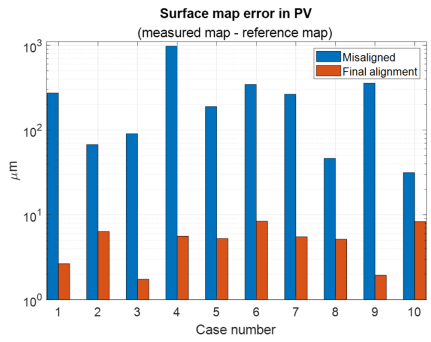


Fig. 8. Improvement of surface map matching via alignment loop.

is the deflectometry counterpart of the alignment mode of interferometry.

In conclusion, we have introduced an automatic alignment algorithm for deflectometry systems using computational fiducials and $\boldsymbol{G}$, $\boldsymbol{C}$ vector polynomials. The algorithm is demonstrated through alignment simulation and experiments. In simulation, remaining amounts of displacement were about tens of micrometers in translation and about 0.001° in tilt. In the actual alignment experiment, remaining amounts were slightly higher than simulated due to hardware limitations, but still less than 100 μm in translation and 0.01° in tilt. The optical testing results show only 8.4 μm of maximum difference from the ideal metrology case. These results imply that the proposed algorithm gives a self-calibration and alignment capability to deflectometry that is inevitable for high accuracy testing.

The proposed algorithm provides quick guidelines and accurate solutions in alignment that benefit freeform metrology, especially when rapid and repeated surface measurements are needed in commercial applications such as quality checks for mass production without extra cost or hardware.

Acknowledgment. The authors acknowledge the II-VI Foundation Block-Gift Program for helping support general deflectometry research in the LOFT group.

Disclosures. The authors declare no conflicts of interest.

Data Availability. Data underlying the results presented in this Letter are not publicly available at this time but may be obtained from the authors upon reasonable request.

REFERENCES

1. P. Su, R. E. Parks, L. Wang, R. P. Angel, and J. H. Burge, Appl. Opt. **49**, 4404 (2010).
2. P. Su, S. Wang, M. Khreishi, Y. Wang, T. Su, P. Zhou, R. E. Parks, K. Law, M. Rascon, T. Zobrist, H. Martin, and J. H. Burge, Proc. SPIE **8450**, 340 (2012).
3. R. Huang, P. Su, J. H. Burge, L. Huang, and M. Idir, Opt. Eng. **54**, 084103 (2015).
4. M. Petz and R. Tutsch, Proc. SPIE **5869**, 366 (2005).
5. Y.-L. Xiao, X. Su, and W. Chen, Opt. Lett. **37**, 620 (2012).
6. T. Zhou, K. Chen, H. Wei, and Y. Li, Appl. Opt. **55**, 7018 (2016).
7. X. Deng, N. Gao, and Z. Zhang, Appl. Sci. **9**, 1444 (2019).
8. M. Hui, X. Li, N. Li, M. Liu, L. Dong, L. Kong, and Y. Zhao, Meas. Sci. Technol. **31**, 045010 (2020).
9. D. Wang, S. Zhang, R. Wu, C. Y. Huang, H.-N. Cheng, and R. Liang, Opt. Express **24**, 19671 (2016).
10. D. Wang, Z. Gong, P. Xu, C. Wang, R. Liang, M. Kong, and J. Zhao, Opt. Express **26**, 8113 (2018).
11. A. Davies, T. Vann, C. Evans, and M. Butkiewicz, Proc. SPIE **10373**, 103730H (2017).
12. E. Olesch, C. Faber, and G. Häuslerin, in *DGaO Proceedings* (2011), p. 7536.
13. X. Xu, X. Zhang, Z. Niu, W. Wang, Y. Zhu, and M. Xu, Opt. Express **27**, 7523 (2019).
14. C. Wang, N. Chen, and W. Heidrich, Opt. Express **29**, 30284 (2021).
15. M. Aftab, J. H. Burge, G. A. Smith, L. Graves, C.-J. Oh, and D. W. Kim, Int. J. Precis. Eng. Manuf. Technol. **6**, 255 (2019).
16. M. Aftab, L. R. Graves, J. H. Burge, G. A. Smith, C. J. Oh, and D. W. Kim, Opt. Eng. **58**, 095105 (2019).
17. H. Kang, H. Quach, H. Choi, G. A. Smith, and D. W. Kim, Proc. SPIE **11487**, 139 (2020).
18. H. J. Jeong, G. N. Lawrence, and K. B. Nahm, Proc. SPIE **0818**, 430 (1987).
19. E. D. Kim, Y.-W. Choi, M.-S. Kang, and S. C. Choi, J. Opt. Soc. Korea **9**, 68 (2005).

APPENDIX C

Computational alignment of on-machine deflectometry

Hyukmo Kang, Henry Quach, Heejoo Choi, Greg A. Smith, and Dae Wook Kim

Publisher's permission is hereby granted under the following conditions: (1) the material to be used has appeared in our publication without credit or acknowledgment to another source; and (2) you credit the original SPIE publication. Include the authors' names, title of paper, volume title, SPIE volume number, and year of publication in your credit statement.

Computational alignment of on-machine deflectometry

Hyukmo Kang[a], Henry Quach[a], Heejoo Choi[a,b], Greg A. Smith[a], and Dae Wook Kim[a,b,c,*]

[a]Wyant College of Optical Sciences, University of Arizona, 1630 E. University Blvd., Tucson, AZ 85721 USA
[b]Large Binocular Telescope Observatory, 933 N. Cherry Ave., Tucson, AZ, 85721 USA
[c]Department of Astronomy and Steward Observatory, University of Arizona, 933 N. Cherry Ave., Tucson, AZ 85721, USA

ABSTRACT

Accurate system calibration remains an area of active improvement in deflectometry. Since deflectometry requires the geometry information of all participating hardware to be well known, miscalibration can mar the accuracy of surface reconstruction especially in lower order shapes. To uphold reconstruction fidelity, extra measuring instruments (i.e. coordinate measuring machines, laser trackers, metering rods) or reference features (i.e. fiducial points or reference mirror) to find out the positions of a camera, a screen, and a unit under test are used. These methods provide reliable calibration but are resource-intensive. In this paper, we introduce an alignment algorithm to calibrate the geometry of a deflectometry configuration. We leverage the concept of alignment algorithm which uses a sensitivity model. With the aid of ray tracing simulation, the relationship between camera pixels and screen pixels of a deflectometer is quantitatively established. This pixel-to-pixel relationship enables us to generate computational imaging of screen and characterize the tendency of misalignments of the deflectometer. On top of that, we can calculate and make multiplexed patterns of screen which highlight the effect of misalignments. We set specific indices and corresponding screen patterns for each alignment parameters to build the sensitivity model. The initial simulation result shows that the algorithm can estimate misalignment status. We believe that this algorithm can be an alternative and efficient calibration process for the deflectometry system, especially when the usage of extra measuring devices is limited.

Keywords: Deflectometry, Alignment, On-machine metrology, Calibration, Computational imaging

1. INTRODUCTION

Deflectometry is an attractive solution for on-machine metrology as it has a high slope measurement range, does not require a physical null reference.[1,2] However, obtaining reliable geometrical information for a deflectometry system is critical for high surface reconstruction accuracy, and imprecise calibration can significantly alter lower order shapes. To uphold reconstruction fidelity, extra measuring devices (i.e. coordinate measuring machines, laser trackers, metering rods) or reference features (i.e. fiducial points or reference mirror) are used to find the geometry of the deflectometry system.[3,4] For an on-machine deflectometer mounted on a computer numerically controlled (CNC) machine, we can easily and precisely obtain the position of the unit under test (UUT), but the relative position between UUT and deflectometer hardware remains uncertain. Furthermore, due to machine costs or the size of the UUT, an external measuring device is not always available.

*E-mail: letter2dwk@hotmail.com

Optical Manufacturing and Testing XIII, edited by Dae Wook Kim, Rolf Rascher,
Proc. of SPIE Vol. 11487, 114870O · © 2020 SPIE · CCC code:
0277-786X/20/$21 · doi: 10.1117/12.2576955

Downloaded From: https://www.spiedigitallibrary.org/conference-proceedings-of-spie on 04 Sep 2020
Terms of Use: https://www.spiedigitallibrary.org/terms-of-use

2. DEFLECTOMETRY SIMULATOR AND ALIGNMENT ALGORITHM

2.1 Deflectometry Simulator

Deflectometry uses the local slope of the optic obtained from a point-to-point correspondence between the planes of the screen, UUT, and detector (Fig. 1). With the aid of ray tracing programs, we establish relationship between the screen, UUT, and detector pixels. After obtaining relationships in multiple scenario (e.g. misalignment), we applied a linear fitting to determine the pair coordinates of screen and detector pixels. This virtual deflectometry simulator (Fig. 2) enables us to characterize misalignments within the deflectometer and surface figure error of the UUT. This simulator has the potential to be applicable towards many deflectometry experiments beyond just alignment, including surface reconstruction and result validation.

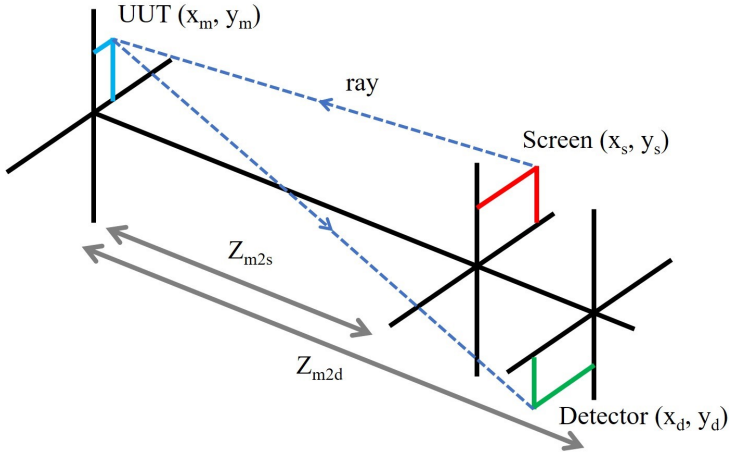
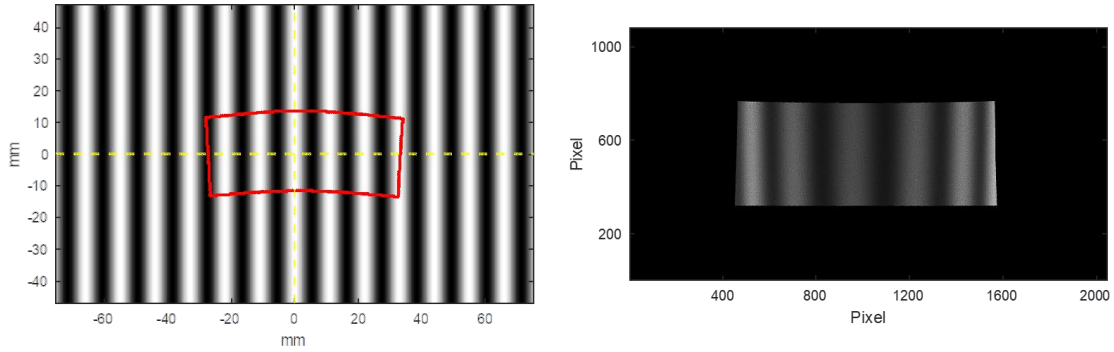


Figure 1. Simple diagram of a deflectometry system.[5] The path of a single ray traced in the deflectometry system. To obtain local slope of UUT, we need the coordinates of screen pixel (x_s, y_s), detector pixel (x_d, y_d), sampled position (x_m, y_m), and distances along the optical axis from UUT to screen and detector, Z_{m2s}, Z_{m2d}.



(a) (b)

Figure 2. Example images from the deflectometry simulator. (a) Sinusoidal pattern is displayed on the screen, and the red outline shows corresponding region to shine the UUT. (b) Image of UUT at the conjugated camera detector plane.

2.2 Sensitivity Matrix

The reverse-optimization algorithm is a widely used method to align optical system.[6–8] This method estimates the misalignments by measuring the wavefront errors or Zernike coefficients at multiple fields (ΔZ), then applying the measured parameters to the theoretical sensitivity matrix (S) to quantify the amount of misalignment (ΔD). For n Zernike terms and m misalignment parameters, it can be expressed as

Downloaded From: https://www.spiedigitallibrary.org/conference-proceedings-of-spie on 04 Sep 2020
Terms of Use: https://www.spiedigitallibrary.org/terms-of-use

$$\Delta Z = S\Delta D, \qquad where$$
$$\Delta Z = \begin{bmatrix} \Delta Z_1 \\ \vdots \\ \Delta Z_n \end{bmatrix} = \begin{bmatrix} Z_1 \\ \vdots \\ Z_n \end{bmatrix} - \begin{bmatrix} Z_{1o} \\ \vdots \\ Z_{no} \end{bmatrix}, S = \begin{bmatrix} \frac{\delta Z_1}{\delta x_1} \cdots \frac{\delta Z_1}{\delta x_m} \\ \vdots \\ \frac{\delta Z_n}{\delta x_1} \cdots \frac{\delta Z_n}{\delta x_m} \end{bmatrix}, \Delta D = \begin{bmatrix} \Delta x_1 \\ \vdots \\ \Delta x_n \end{bmatrix} = \begin{bmatrix} x_1 \\ \vdots \\ x_n \end{bmatrix} - \begin{bmatrix} x_{1o} \\ \vdots \\ x_{no} \end{bmatrix}. \quad (1)$$

In practice this approach shows convergence of misalignment values after iterative alignment if the sensitivity is linear. To utilize this approach, finding linear sensitive indicators for the computational deflectometry alignment process is essential, which are discussed in chapter 3.2.

3. COMPUTATIONAL ALIGNMENT SIMULATION

3.1 End-to-end simulation setup

We developed and built the deflectometry model simulation analyze algorithm. In this simulation, we set the deflectometer to have a screen size 7 inches across the diagonal with resolution of 1920×1080 pixels and a 2MP color camera located 10 mm above the screen where both centers lie on the Y axis. We utilized a freeform mirror with rectangular aperture (Tab. 1). The center of the UUT lies on the Z axis 200 mm away from the camera and is slightly tilted such that the screen fills the field of view. The overall simulation layout is shown in Fig. 3.

Table 1. Specification of the UUT

Surface Type	X Width	Y Width	X Radius of Curvature	Y Radius of Curvature	X Conic Constant	Y Conic Constant
Bi-aspheric	60 mm	24 mm	150 mm	400 mm	4	-2

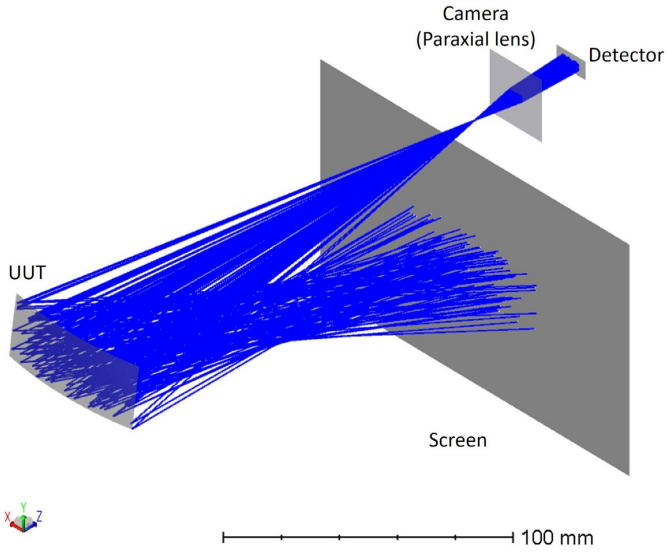


Figure 3. Layout of the deflectometry simulation. Camera and the center of UUT are aligned along the Z-axis for symmetry.

Downloaded From: https://www.spiedigitallibrary.org/conference-proceedings-of-spie on 04 Sep 2020
Terms of Use: https://www.spiedigitallibrary.org/terms-of-use

3.2 Alignment parameters

The alignment parameters utilized in the sensitivity matrix require two features to be effective; i) Linearity for misalignment ii) Orthogonality between different degree of freedoms. We must consider these features to correctly set the indices and corresponding screen patterns for each alignment parameter to highlight the effects of misalignments. For X and Y translation of the UUT against deflectometry system (Dx, Dy) we set X and Y centroid position of UUT image as alignment parameters. For Z translation (Dz), we set the image size at the camera sensor as alignment parameter. Generally, it is hard to distinguish between translation and tilt while watching the UUT image via camera because they show similar aspects in deviation. However, contrary to the translation, tilting uses a smaller region on screen to shine the UUT due to the projection (Fig. 4). We find that the rgb-triplet values could be used as an alignment parameter to separate tilt from translation. In this simulation, the binary red/blue pattern on the screen and recorded r/b ratio (in terms of areas on detector) shows sensitivity to tilt in X and Y (Tx, Ty). (Fig. 5 (a),(b)) For the tilt in Z (Tz, clocking of the UUT), we displayed a rgb pattern (similar to Bayer filter layout) and used g-value (i.e., green area on detector) itself as the alignment parameter (Fig. 5(c)). We investigated how each of the alignment parameters are changing from -1 mm to 1 mm in translation, and from -1 degree to 1 degree in tilt using Zemax OpticStudio, and linear fitting. The linear fitting coefficients are shown in Tab. 2.

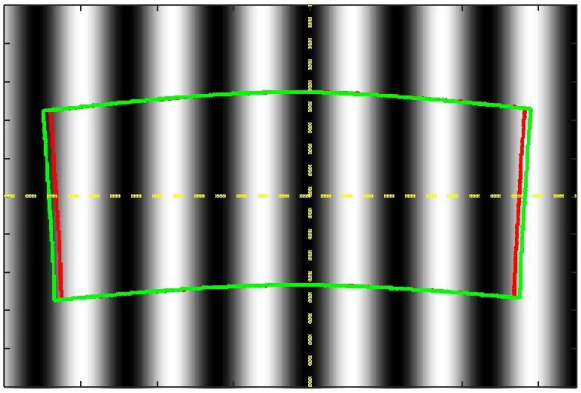
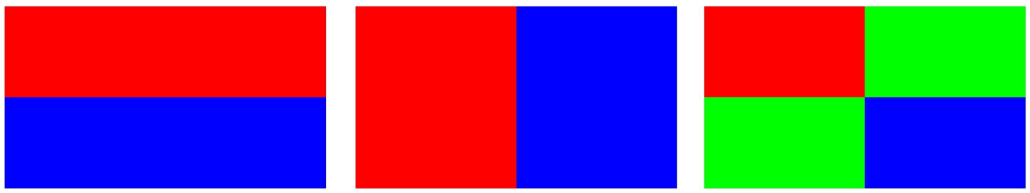


Figure 4. Effective area of screen when perturb the UUT with translation in X (red outline) and tilt in Y (green outline). The position of effective area is similar, but different in size especially in horizontal direction.



(a) (b) (c)

Figure 5. Color patterns that used to define alignment parameters for tilt. (a) Tilt in X (Tx) (b) Tilt in Y (Ty) (c) Tilt in Z (Tz)

Sensitivity graphs of X centroid and r/b ratio for left-right color pattern are shown in Fig. 6 and Fig. 7 as examples. In Fig. 6, translation in X is most sensitive, and other degree of freedoms are negligible. In Fig. 7, tilt in Y shows most rapid slope, but translation in X also has some gradient. This coupling effect would affect the performance of alignment state estimation. However, since the slope is 5 times greater, and the translation in X would be corrected by other parameter (X centroid), we could mitigate the coupling effect by iteration. The effect of imperfect linearity in tilt in Y also can be relieved by iteration.

Downloaded From: https://www.spiedigitallibrary.org/conference-proceedings-of-spie on 04 Sep 2020
Terms of Use: https://www.spiedigitallibrary.org/terms-of-use

Table 2. Sensitivity table for all possible degree of freedom. Highlighted cells mean the most sensitive degree of freedom for each alignment parameters that will be used as indicator.

DoF	Cen.X	Cen.Y	Img. Size	r/b (a)	r/b (b)	g
Dx	-22.50	0.00	-0.02	0.00	0.10	0.01
Dy	-0.03	-22.93	0.50	-0.32	0.00	0.00
Dz	0.01	-0.06	5.01	-0.03	0.00	0.00
Tx	0.00	0.60	-1.74	1.86	0.00	0.00
Ty	0.69	-0.01	0.06	0.00	0.53	0.00
Tz	-0.09	-0.03	-0.07	0.00	0.03	-0.02

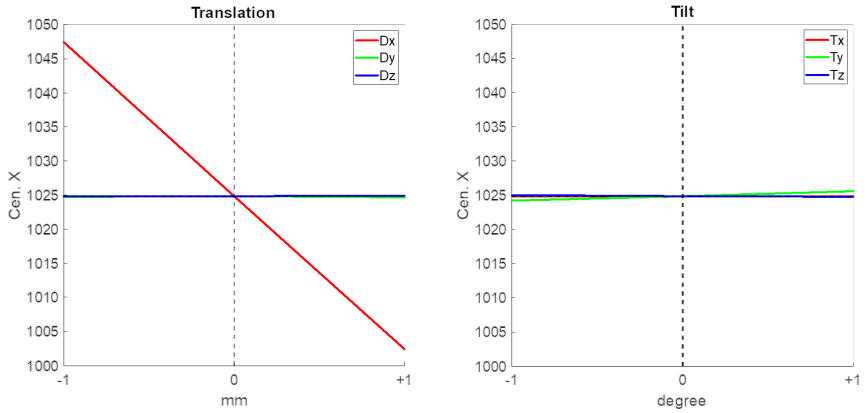


Figure 6. Sensitivity trend plots of X-centroid for all misalignment cases. Translation in X shows most sensitivity, and other misalignments have negligible slopes.

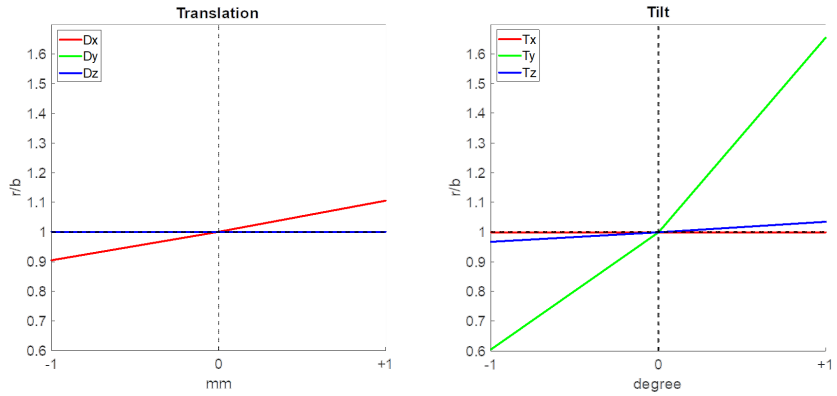


Figure 7. Sensitivity trend plots of r/b ratio when Fig. 5(b) is used. Tilt in Y shows most sensitivity compared to other misalignments. The effects of coupling and insufficient linearity could be mitigated by iterative alignment steps.

Downloaded From: https://www.spiedigitallibrary.org/conference-proceedings-of-spie on 04 Sep 2020
Terms of Use: https://www.spiedigitallibrary.org/terms-of-use

3.3 Iterative alignment process simulation

Fig. 8 shows the results of an iterative alignment process simulation assuming an on-machine alignment using the CNC machine axis in each iteration. We imposed random initial misalignment errors to the UUT position and utilized our simulator to obtain the misalignment amount for all degree of freedoms, simultaneously. As a result, calculated misalignment values are converged in induced initial errors after 7 iterations. Dx and Dy converged faster due to their higher sensitivities. Ty and Tz converged shortly after Dx, since Dx disturbs both the r/b ratio and g value. Finally, Dz and Tx converge, but are not fully corrected; however, the converged values for Dz and Tx are within the regime of mechanical error.

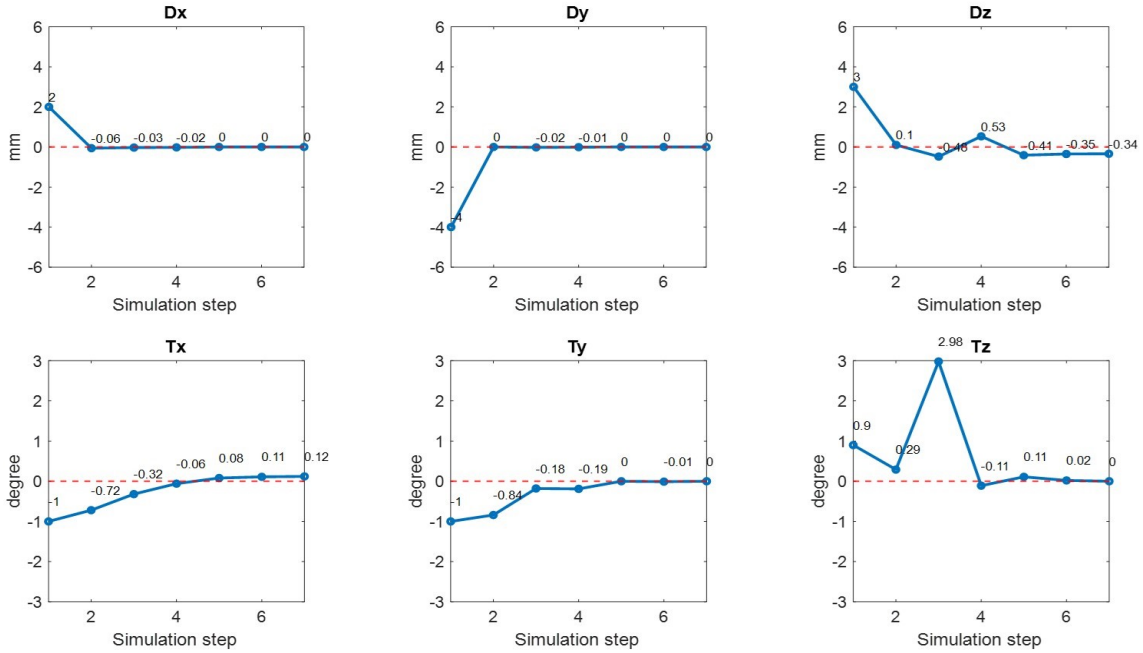


Figure 8. Iterative on-machine deflectometry alignment simulation results using the proposed computational alignment method. After 7 times of iteration, all alignment parameters are successfully converged. As the parameter for Tz is also varies with Dx and the sensitivity is similar (Tab. 2), it shows spike in third iteration step. However, after Dx is corrected, Tz is corrected and converged as well.

4. CONCLUSION

A computational alignment algorithm to calibrate the geometry of a deflectometry configuration is introduced and simulated. We obtained the required pixel-to-pixel relationship between the detector, UUT, and screen using ray tracing programs. Then set specific indices and corresponding screen patterns to determine the effect of misalignments for each degree of freedom. The initial simulation result shows that the algorithm can estimate each misalignment for each degree of freedom and provide a convergent solution for *all* degree of freedoms. This algorithm can be used as an efficient alternative calibration process for deflectometry systems, especially when the usage of extra measuring devices is limited and the CNC machine axis can provide precise alignment adjustments. We plan to perform further error analysis including other calibration errors, and apply the algorithm to an actual measurement process.

Downloaded From: https://www.spiedigitallibrary.org/conference-proceedings-of-spie on 04 Sep 2020
Terms of Use: https://www.spiedigitallibrary.org/terms-of-use

ACKNOWLEDGMENTS

The authors would like to acknowledge the II-VI Foundation Block-Gift Program for helping support general deflectometry research in the LOFT group. A special thank you goes to John Kam who helped edit and gave feedback on the article.

REFERENCES

[1] Su, P., Parks, R. E., Wang, L., Angel, R. P., and Burge, J. H., "Software configurable optical test system: a computerized reverse hartmann test," *Appl. Opt.* **49**, 4404–4412 (Aug 2010).

[2] Su, P., Wang, S., Khreishi, M., Wang, Y., Su, T., Zhou, P., Parks, R. E., Law, K., Rascon, M., Zobrist, T., Martin, H., and Burge, J. H., "SCOTS: a reverse Hartmann test with high dynamic range for Giant Magellan Telescope primary mirror segments," in [*Modern Technologies in Space- and Ground-based Telescopes and Instrumentation II*], Navarro, R., Cunningham, C. R., and Prieto, E., eds., **8450**, 332 – 340, International Society for Optics and Photonics, SPIE (2012).

[3] Huang, R., Su, P., Burge, J. H., Huang, L., and Idir, M., "High-accuracy aspheric x-ray mirror metrology using software configurable optical test system/deflectometry," *Optical Engineering* **54**(8), 084103 (2015).

[4] Su, P., Khreishi, M., Huang, R., Su, T., and Burge, J. H., "Precision aspheric optics testing with SCOTS: a deflectometry approach," in [*Optical Measurement Systems for Industrial Inspection VIII*], Lehmann, P. H., Osten, W., and Albertazzi, A., eds., **8788**, 392 – 398, International Society for Optics and Photonics, SPIE (2013).

[5] Kam, J., "Differential phase measuring deflectometry for high-sag freeform optics," (2019).

[6] Figoski, J. W., Shrode, T. E., and Moore, G. F., "Computer-aided alignment of a wide-field, three-mirror, unobscured, high-resolution sensor," in [*Recent trends in Optical systems design and computer lens design workshop II*], **1049**, 166–177, International Society for Optics and Photonics (1989).

[7] Zhang, B., Zhang, X., Wang, C., and Han, C., "Computer-aided alignment of the complex optical system," in [*Advanced Optical Manufacturing and Testing Technology 2000*], **4231**, 67–72, International Society for Optics and Photonics (2000).

[8] Kim, E. D., Choi, Y.-W., Kang, M.-S., and Choi, S. C., "Reverse-optimization alignment algorithm using zernike sensitivity," *Journal of the Optical Society of Korea* **9**(2), 68–73 (2005).

Downloaded From: https://www.spiedigitallibrary.org/conference-proceedings-of-spie on 04 Sep 2020
Terms of Use: https://www.spiedigitallibrary.org/terms-of-use

APPENDIX D

Plug-in spectrograph module enabling cross-dispersion for Large Binocular Telescope

Hyukmo Kang, David Thompson, Al Conrad, James Wiese, Heejoo Choi, Vishnu Reddy, and Daewook Kim

Journal article submitted to ***Journal of Astronomical Telescopes, Instruments, and Systems***.

Plug-in spectrograph module enabling cross-dispersion for Large Binocular Telescope

Hyukmo Kang[a], David Thompson[b], Al Conrad[b], James Wiese[b], Heejoo Choi[a,b], Vishnu Reddy[c], Daewook Kim[a,b,d,*]

[a]James C. Wyant College of Optical Sciences, University of Arizona, 1630 E. University Blvd., Tucson, AZ 85721 USA

[b]Large Binocular Telescope Observatory, 933 N. Cherry Ave., Tucson, AZ, 85721 USA

[c]Lunar and Planetary Laboratory, University of Arizona, 1629 E. University Blvd., Tucson, AZ 85721, USA

[d]Department of Astronomy, University of Arizona, 933 N. Cherry Ave., Tucson, AZ, 85721 USA

Abstract. The Large Binocular Telescope (LBT) can spectrally characterize faint objects from the Ultra Violet (UV) to the Near InfraRed (NIR) using two instruments, MODS (The Multi-Objects Double Spectrograph) and LUCI (LBT Utility Camera in the Infrared) which are pairs of imagers and spectrographs. Although LUCI can cover the continuous NIR spectrum, we need to use both LUCIs at the same time with existing gratings and filters. In this paper we report on the optical design, tolerances, and initial (warm) laboratory testing of the as-built optics. The designed system is called MOBIUS (Mask-Oriented Breadboard Implementation for Unscrambling Spectra) that enables a single LUCI to produce a simultaneous zJHK spectrum in a single exposure. MOBIUS is a Littrow type spectrograph that consists of a pick-off mirror, a spherical mirror, and a dispersing prism. This system will be installed within the limited space of exchangeable mask frame and located near the focal plane of LBT by the MOS (Multi-Object Spectroscopy) unit. This plug-in concept requires no additional modification to the current instrument while dispersing the input slit perpendicular to the dispersion direction of the gratings in LUCI. With MOBIUS, we can utilize a slit length up to 2.3 arcsecond to acquire zJHK spectra without mixing orders at the LUCI image plane. The performance of MOBIUS is verified via tabletop experiments. Eventually, the binocular observation mode of LBT that combines MODS with LUCI+MOBIUS enables to cover the wavelength range from 0.3 to 2.4 μm simultaneously to benefit studies of planetary science programs.

Keywords: LBT, LUCI, Infrared, Spectrograph, Cross dispersion, Instrument Design.

*Daewook Kim, dkim@optics.arizona.edu

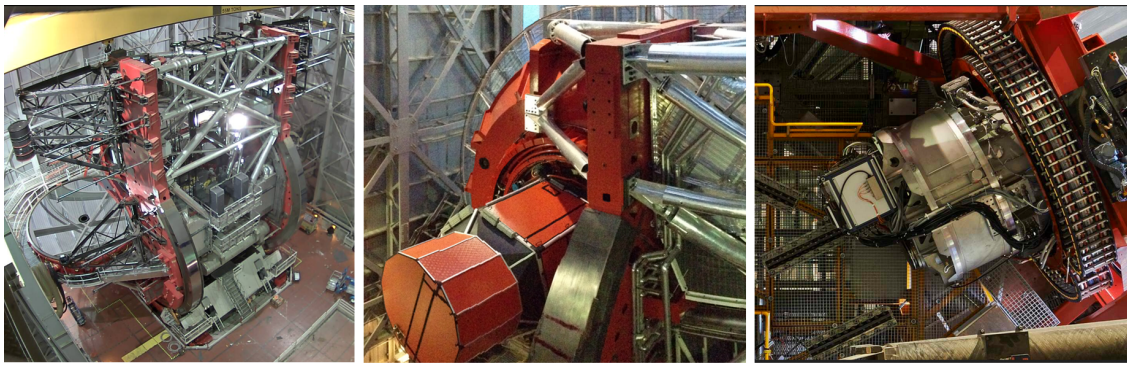
1 Introduction

What was the chemical composition of the Solar System during its formation about 4.6 billion years ago? Asteroids or comets are recognized as leftover building blocks that remain relatively unchanged from the early stages of the Solar System. Therefore, studying these types of objects is essential to figure out the chemical composition of primordial mixtures.

Spectroscopy provides clues about the surface chemical compositions of these observation targets. UltraViolet (UV) to Near-InfraRed (NIR) spectra ($0.3 - 2.5\ \mu m$) have been widely used to determine surface compositions of asteroids.[1] This is because the most common components

of asteroid surface materials such as pyroxene, olivine, and other mafic materials have diagnostic spectral features in these bands.

The Large Binocular Telescope (LBT) is made up of two f/15 Gregorian telescopes, and two $8.4\ m$ diameter primary mirrors are located side-by-side for the $11.8\ m$ of effective diameter (Fig. 1(a)).[2] LBT can spectrally characterize faint objects from UV to NIR using two instruments, MODS (The Multi-Objects Double Spectrographs) (Fig. 1(b))[3] and LUCI (LBT Utility Camera in the Infrared) (Fig. 1(c)).[4] The MODS are a pair of UV to NIR ($0.32 - 1\mu m$) imager/spectrographs, and the LUCI are a pair of NIR ($0.86\mu m - 2.4\mu m$) imagers/spectrographs. Both instruments provide long-slit spectroscopy and Multi-Object Spectroscopy (MOS). As each mirror of LBT can be equipped independently, we can configure mixed spectrographs pairs depending on scientific studies. For example, we can use both LUCIs simultaneously to get a continuous NIR spectrum coverage of the zJHK bands (zJ and HK filters).[5] Or we can extend the coverage from UV to NIR by running one MODS and one LUCI at the expense of either the zJ or HK bands.



(a) **(b)** **(c)**

Fig 1 Photos of (a) LBT, (b) one unit of MODS, and (c) one unit of LUCI. Both MODS and LUCI are existing on both sides of the binocular. Therefore each side could be configured with different instruments (mixed-mode) such as LUCI and MODS[3]

What if we could not only extend this coverage to the UV as well but over a continuous wave-

length range? First, wide wavelength coverage is an advantage to compare emission lines across the NIR bands in the same atmospheric conditions because the chances of getting more spectral features are increased. Also, the simultaneous coverage of the zJHK band enables to use telescope time efficiently. This implies that we can save instrument calibration time and have advantages for the target which changes on a relatively short time scale such as rotating asteroids, comets, or other transient astronomical events.

In this paper, we present our design of a cross-disperser module called MOBIUS (Mask-Oriented Breadboard Implementation for Unscrambling Spectra) which produces a simultaneous zJHK spectrum with a single LUCI.[6] Requirements for the MOBIUS design included that there would be no modifications to the existing LUCI instruments and that it would not affect the image quality of LUCI. This is achieved by mounting MOBIUS inside of an exchangeable slit mask frame, located at the telescope focal plane. We compared the ensquared energy of each band with and without MOBIUS to show that the plug-in extension would not degrade the performance of LUCI. A tabletop experiment with fabricated optical components was also performed to demonstrate the performance of MOBIUS. By combining this system with MODS through binocular observations, MOBIUS in LUCI provides simultaneous coverage from UV to NIR with little penalty.[5]

2 Design of MOBIUS

2.1 Concepts

The main objective of MOBIUS is a plug-in extension module of LUCI to provide full wavelength coverage in a single unit subject to scientific objectives. For that purpose, the MOBIUS-equipped frame will be stored and handled by the MOS unit.[7] Thus, MOBIUS can be placed in the focal plane of the LBT and removed on demand easily (Fig. 2). MOBIUS is also required to minimize

the impact on the image quality at the LUCI detector plane while providing cross-dispersion in LUCI. This indicates that the optical properties of the incident beam from LBT (*i.e.,* f-number, chief ray angle, focal plane position) should be kept after the MOBIUS module is inserted. Lastly, MOBIUS consists of two identical cross-disperser modules symmetrically side by side in a single mask frame to offer sky-subtraction by dithering between source and sky positions.

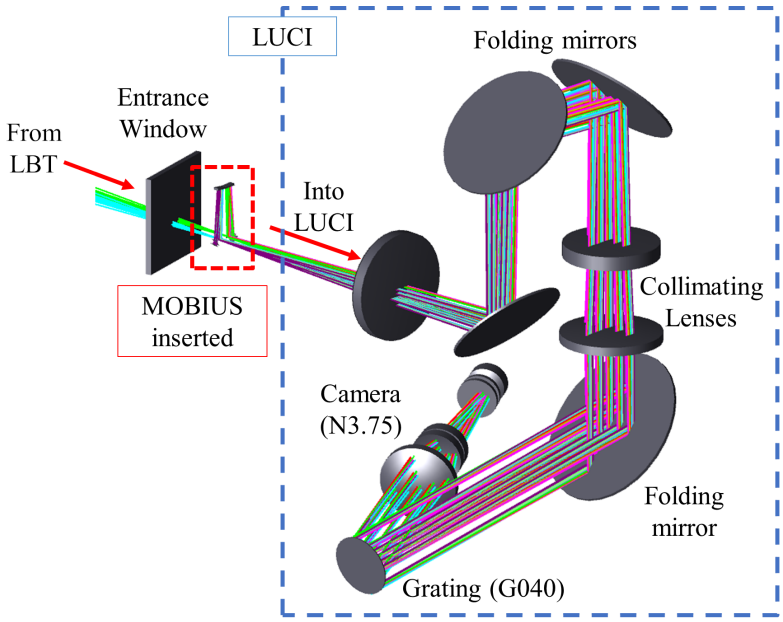


Fig 2 The optical layout shows how MOBIUS works with LUCI. The MOBIUS-installed frame will be placed at the focal plane of LBT by substituting the traditional slit mask frame. With MOBIUS, LUCI is able to observe zJHK spectra in a single exposure without mixing between wavelength bands without additional modification in instrument settings.

Littrow type of spectrographs[8,9] is perfectly fit to our concepts. With a mirror-coated rear surface, Littrow prism configurations utilize a double pass that enables increased dispersion in a compact form and returns dispersed rays to near the original slit position.

The schematic concept of MOBIUS is shown in Fig. 3.[6] The triangle shape pick-off mirror is located right before the focal plane of LBT to deflect the incident beam towards into the space in

the mask frame, and a slit will be installed right after the pick-off mirror (Fig. 3(a)). The beam is then collimated through a spherical mirror and enters the Littrow prism which provides retro-reflection and dispersion. After reflection, the dispersed beam hits the spherical mirror again and is imaged on the other side of the pick-off mirror to advance to LUCI (Fig. 3(b)). Since the dispersed beams are still within the field of view of LUCI, there would be no vignetting as long as the ray angle and focal planes have remained unchanged from the original LBT beam. As the beam is dispersed at the focal plane of LBT to the perpendicular direction of LUCI's dispersion, MOBIUS broadens the wavelength coverage of a single LUCI with no modification in the instrument setting.

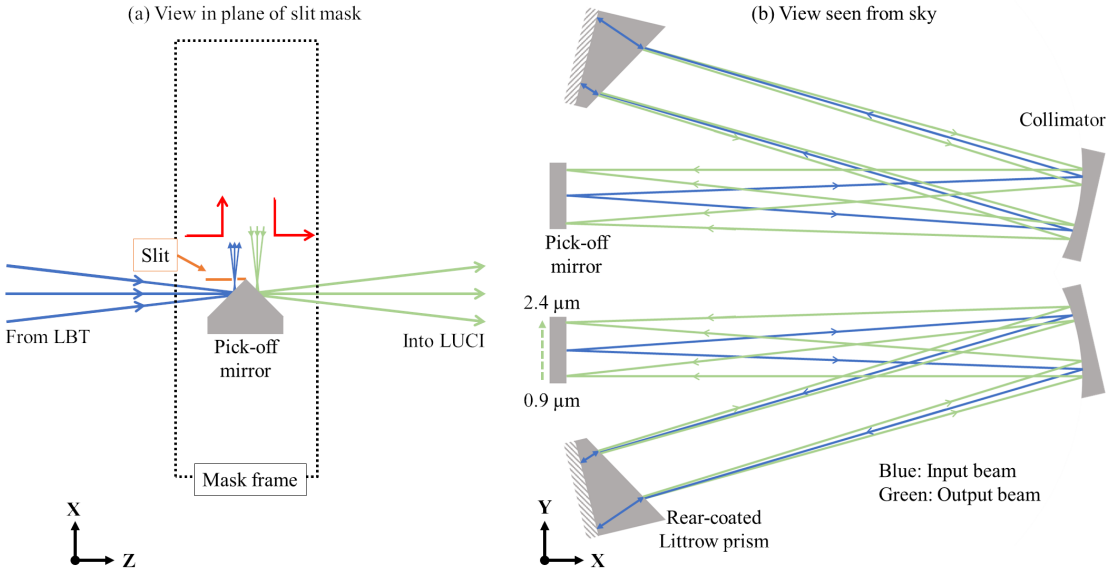


Fig 3 Schematic figure of MOBIUS.[6] (a) The pick-off mirror is placed near the focal point of LBT to deflect the input beam path (blue lines) into the plane of the mask frame. The beam is focused right after the reflection at the entrance surface of the pick-off mirror. (b) Inside of the frame mask, the beam is collimated and dispersed (green lines). The beam is reflected from the rear surface of the prism, then focused near the original focal point with shorter wavelength is located close to the prism. This process produces the cross-dispersion before the higher dispersion grating in LUCI. MOBIUS consists of two identical spectrographs to offer sky-subtraction by dithering between target and sky position.

2.2 Design boundary conditions

The modular plug-in concept utilizes an existing feature of LUCI (*i.e.* MOS unit[7]) to handle the MOBIUS-equipped make frame. Thus, the hardware boundary conditions are given from the capabilities of the MOS unit. Firstly, every optical and mechanical component needs to be packed within the slit mask frame space ($150\ mm \times 150\ mm \times 12\ mm$). Further, the extra weight of the MOBIUS system should be kept within 20 grams of a standard MOS mask to be operated safely.

MOBIUS should provide a large enough dispersion distance to prevent overlapping between diffraction order spectra at the LUCI detector while securing the minimum slit length, 2 arcsecond, for scientific objectives. As the current MOBIUS design is optimized for the N3.75 camera and G040 grating,[10] 2 arcsecond of slit length corresponds to the $1.2\ mm$ of dispersion distance at the LBT focal plane. Considering the margin between spectra at the detector, we set our target minimum dispersion distance between the central wavelength of each order as $1.5\ mm$ at the exit surface of pick-off mirror.

2.3 Design process

MOBIUS consists of three optical components: a pick-off mirror, a spherical mirror as collimator, and a Littrow dispersing prism which has a mirror-coated rear surface. The specific parameters of each component are determined considering dispersion distance, maximum beam footprint size, and the best focal region of LBT.

The shape of the pick-off mirror is a right-angle prism, yet the outer surfaces are employed for reflection (Fig. 5(a)). Since the dispersed beam is retro-reflected, the input and output beams are nearly parallel to each other. So the apex angle of the pick-off mirror is designed 90° to preserve the ray angles before and after the MOBIUS. The location of the pick-off mirror inside of slit mask

frame is determined by the best focal region of LBT ($\pm$ 1.25 arcminute in dispersion direction of LUCI which is perpendicular to the dispersion direction of MOBIUS)[7] as well as the focal length of the collimating mirror.

For the collimating mirror (Fig. 5(b)), although an Off-Axis Parabolic mirror (OAP) is commonly used, we chose a spherical mirror because it made negligible aberration on the focused, slow f/15 beam from the telescope. The spherical mirror is advantageous in fabrication and alignment as well. The focal length of a spherical mirror is directly related to the dispersion distance since the longer focal length produces greater dispersion. We set the radius of curvature of the spherical mirror to $180\ mm$ in MOBIUS. As a consequence, we could secure some margin at the clear aperture of spherical mirror while extending slit length for scientific objectives.

The Littrow dispersing prism (Fig. 5(c)) is made of Strontium Titanate ($SrTiO_3$, $n = 2.28$ at $\lambda = 1.65\ \mu m$) which is transmissive and highly dispersive at the operating wavelengths and temperature.[11,12] The apex angle of the prism determines dispersion distance primarily. To calculate the dispersion distance between two wavelengths, we need to find the deviation angle difference first. In the Littrow prism (Fig. 4), the apex angle (α) is equal to the refractive angle to make the refractive ray is reflected as normal to the rear surface. So the incident angle θ_i is determined as

$$\theta_i = \sin^{-1}(n_a \sin\alpha) \tag{1}$$

where n_a is refractive index of wavelength λ_a. Assumed that the base wavelength is λ_a, the refracted angle (θ_b) of wavelength λ_b inside of prism is

$$\theta_b = \sin^{-1}(\frac{n_a}{n_b} \sin\alpha) \tag{2}$$

Now, the beam is reflected from the rear surface, and resulted refracted angle from the prism (θ'_b) is

$$\theta'_b = \sin^{-1}[n_b \sin(2\theta_b - \alpha)] \tag{3}$$

Thus, deviation of λ_b when the base wavelength is λ_a ($\delta_{a,b}$) is

$$\begin{aligned} \delta_{a,b} &= \theta'_b - \theta_i \\ &= \theta'_b - \sin^{-1}(n_a \sin\alpha) \end{aligned} \tag{4}$$

Therefore the dispersion distance ($\Delta d_{a,b}$) is

$$\Delta d_{a,b} = f \tan(\delta_{a,b}) \tag{5}$$

where f represents the focal length of the spherical mirror.

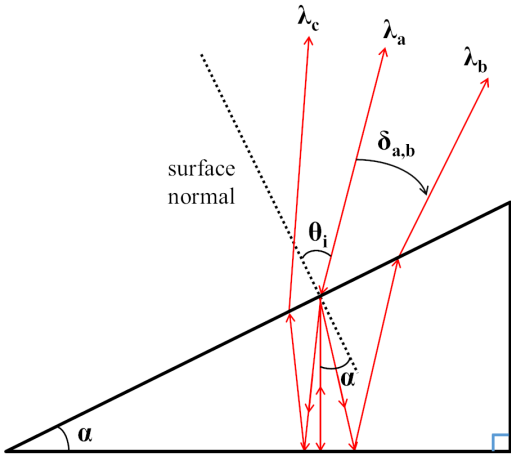
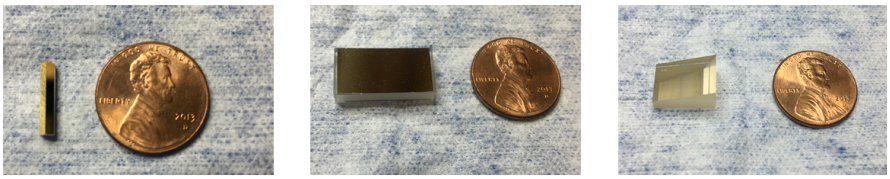


Fig 4 Ray diagram of Littrow prism. The apex angle (α) of prism should be equal to the refractive angle to make retro-reflection.

MOBIUS is required to separate four NIR bands corresponding to the orders of G040 grating in LUCI. The central wavelength (λ_c) of each band is $0.97\ \mu m$ (z), $1.25\ \mu m$ (J), $1.65\ \mu m$ (H), and $2.2\ \mu m$ (K).[10] Therefore we found the apex angle of prism to make minimum dispersion requirement between J-band and H-band since their refractive indices show the least difference. Above condition and Eq. 5 lead the apex angle as $19°$. Also, the derived incident angle is $48°$ and the dispersion distance between the J and H band is $1.65\ mm$ at the focal plane of the LBT which meets our requirement.



(a) (b) (c)

Fig 5 Fabricated optical components of MOBIUS. (a) The pick-off mirror is made of Zerodur and gold coated. Clear aperture is $12\ mm$ by $2\ mm$. (b) The spherical mirror is made of Zerodur and aluminum-coated. Clear aperture is $17.5\ mm$ by $9\ mm$. (c) Littrow prism with silver-coated on rear surface. The entrance surface has about $13\ mm$ by $8\ mm$ of clear aperture.

The optical design of a unit of MOBIUS is shown in Fig. 6(a)[6] and the overall layout with optical components mounted in a slit mask frame is in Fig. 6(b). The light-weighted features are implemented on the frame to meet the safe weight requirement (total frame weight of 326 grams with 20 grams of additional weight) of the MOS unit. We also added alignment screws in the MOBIUS module for fine adjustment.

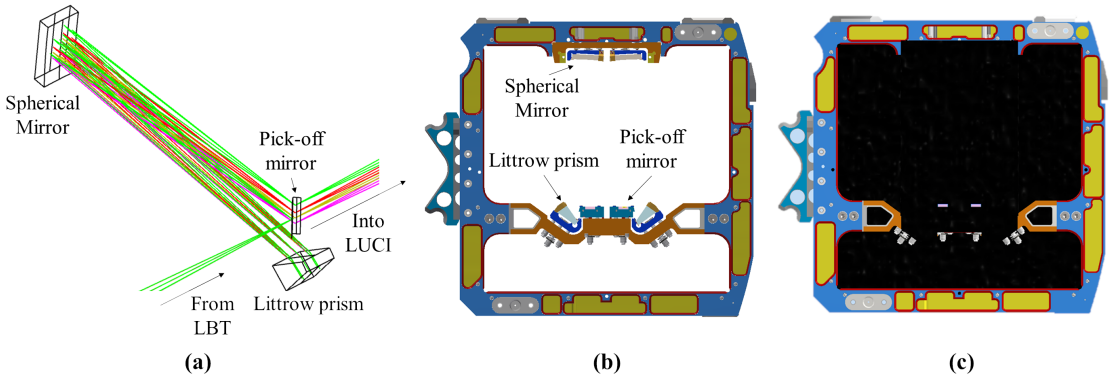


Fig 6 (a) Optical layouts of a unit of MOBIUS.[6] (b) The layout of MOBIUS mounted slit mask frame with alignment features. We light-weighted the frame to meet the weight limit of MOBIUS. Two identical spectrographs are located in plane symmetry and the slits are placed as close as possible for the sky subtraction by dithering. (c) MOBIUS with mask (black color). The mask blocks empty space of frame except the entrance to MOBIUS.

Main concerns of MOBIUS is vignetting as the optical performance is kept good enough as long as the beam is not vignetted. We performed a sensitivity analysis to figure out the alignment tolerance of each optical component. Z-axis is defined along with beam path of LBT, and Y-axis is the direction of dispersion from MOBIUS. Table. 1 shows the tolerance results of MOBIUS. Translation in x, y, and z-axis are denoted as Dx, Dy, Dz for each, and tilt about x, y, and z-axis are denoted as Tx, Ty, Tz. As the entrance slit is coupled together, the X, Y, Z coordinate of the pick-off mirror is set as reference. Tolerances of Tz of pick-off mirror, Tx of spherical mirror and prism are not specified as they have minor effects only. Overall alignment tolerance is quite generous while the apex angle of the pick-off mirror is the most sensitive factor for vignetting. The tolerable range of apex angle of the pick-off mirror (α) is from $-2.27\ mrad$ to $0.7\ mrad$ from the designed value, $90°$.

Table 1 Tolerance results for alignment of each component and apex angle of the pick-off mirror.

	Dx (mm)	Dy (mm)	Dz (mm)	Tx (mrad)	Ty (mrad)	Tz (mrad)
Pick-off mirror	-	-	-	1.4	1.7	-
Spherical mirror	0.2	0.2	0.3	-	1.4	1.13
Prism	0.5	0.5	0.5	-	1.7	1.7
Apex angle of pick-off mirror	$89.87° \leq \alpha \leq 90.04°$					

3 Performance analysis

3.1 Designed performance

The footprint diagram of LUCI and LUCI with MOBIUS are shown in Fig. 7.[6] In LUCI alone, (Fig. 7(a)), all the spectra are overlapped in a line so that the filter is essential to distinguish different bands. On the other hand, as MOBIUS generates perpendicular dispersion to LUCI, each spectrum is separated and distinguishable regardless of filters (Fig. 7(b)). In the current design configuration with N3.75 camera and G040 grating, MOBIUS can utilize a slit length up to 2.3 arcsecond without mixing different wavelength bands.

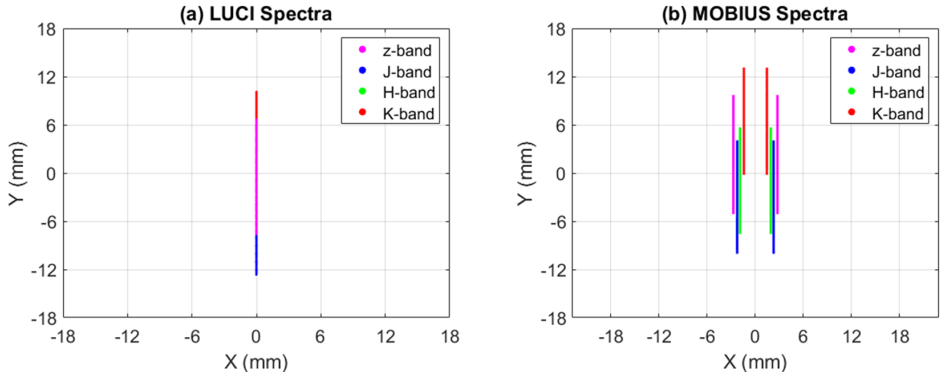


Fig 7 Spectra results at the LUCI detector. (a) When observing using LUCI and (b) LUCI with MOBIUS. With MOBIUS, spectra of each order are not overlapped up to 2.3 arcsecond of slit length. Two sets of zJHK spectra are found as the two spectrographs in MOBIUS are mirror-symmetric to allow the entrance slits to be closer together on sky.[6]

On top of cross-dispersion, another important requirement for MOBIUS maintains the image

quality of LUCI after being plugged in. We compared the spot diagram at the LBT focal plane (Fig. 8)[6] and ensquared energy at the LUCI detector plane (Fig. 9)[6] to verify that the image quality remains the same with MOBIUS. Although the overall radius of rms spot size has increased after MOBIUS is plugged-in (Fig. 8), the difference is negligible as the expected smallest Full-Width Half Maximum (FWHM) at the LBT focal plane is $150\ \mu m$. In ensquared energy case (Fig. 9), the most measurable difference is at K-band in half width distance for 90% fraction energy, which is about $2\ \mu m$. Since the expecting seeing disk size delivered by the telescope is >2 pixels on the N3.75 camera and a pixel size is $18\ \mu m$, we can assume that MOBIUS is not limiting to the image quality while expanding wavelength coverage of LUCI with little penalty.

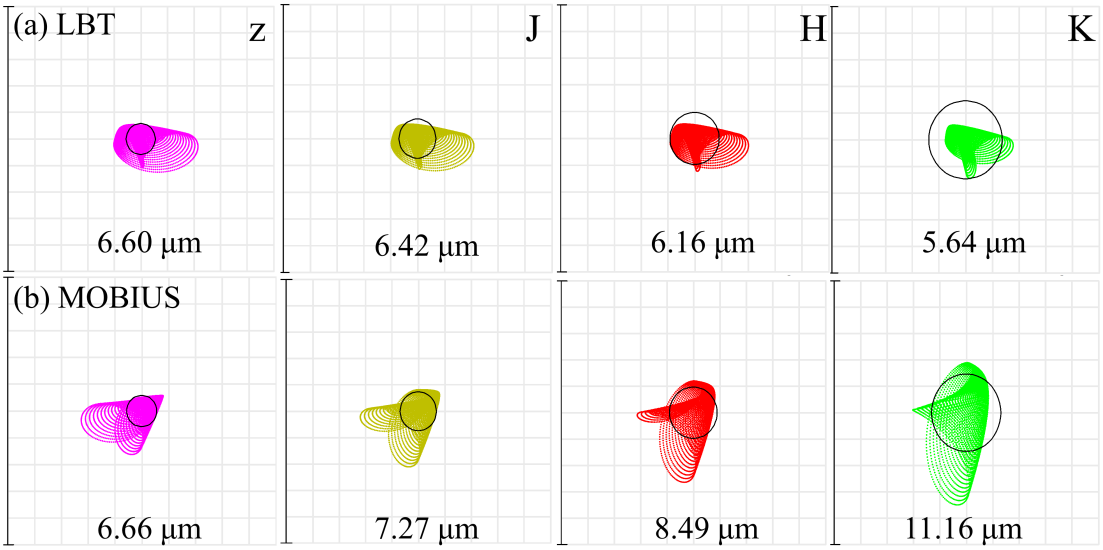


Fig 8 Spot diagrams at the focal plane of (a) LBT and (b) when MOBIUS is inserted in each wavelength band. Numbers in the figure show the rms radius of each spot diagram. Although the rms value is increased after the MOBIUS, considering the smallest expected FWHM at the focal plane delivered from the telescope is $150\ \mu m$, the image quality is seeing-limited.[6]

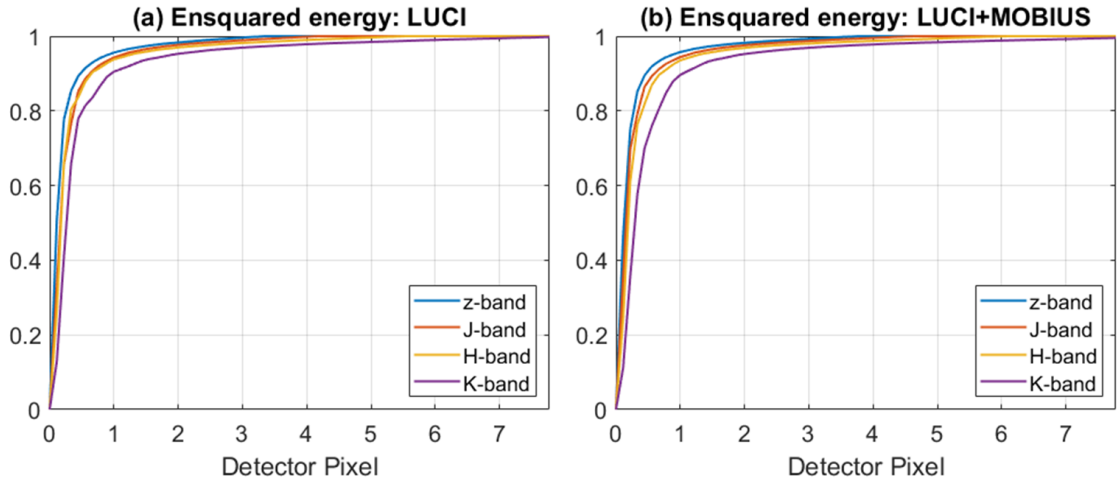


Fig 9 Ensquared energy comparison between (a) LUCI and (b) LUCI with MOBIUS-equipped. In every wavelength band, the difference in half width distance between LUCI and MOBIUS for 90% fraction energy is less than a pixel of the detector. This difference is insignificant as the expected seeing disk size is >2 pixels or 0.25 arcsecond.[6]

3.2 Table-top result

The table-top test was performed with optical components assembled in a rigid aluminum frame (Fig. 10(a)). We used a xenon light bulb as a light source to secure broad NIR wavelength (from $0.9\ \mu m$ to $1.7\ \mu m$) and formed an f/15 beam to simulate LBT (Fig. 10(b)). The specification of the detector we used[13] is summarized in Table 2.

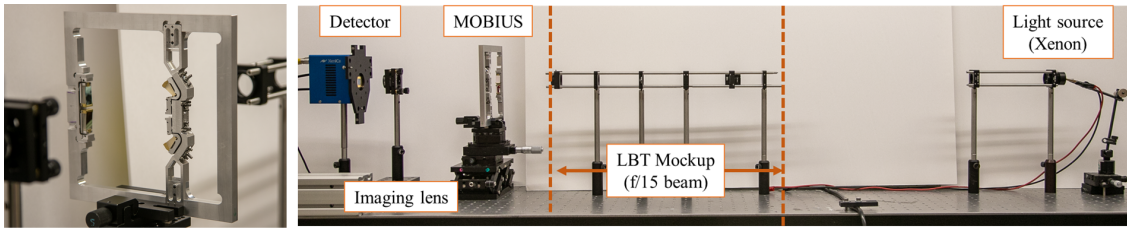


Fig 10 (a) MOBIUS with rigid aluminum frame is mounted in the table-top test setup. This frame allows alignment and testing of the MOBIUS optics in their proper positions. (b) The test setup of MOBIUS.

Table 2 Specification of detector[13]

	XEVA-FPA-320 by XenICs
Type	InGaAs
Format	320×256 pixels
Pixel pitch	30μm
Spectral range	900 - 1700 μm

The table-top result is shown in Fig. 11. The length of resulted MOBIUS spectrum is about 110 pixels (3.3 mm) at the detector. Considering the quantum efficiency of the detector, this result is validated with the expected spectrum length from the Zemax model (3.6 mm).

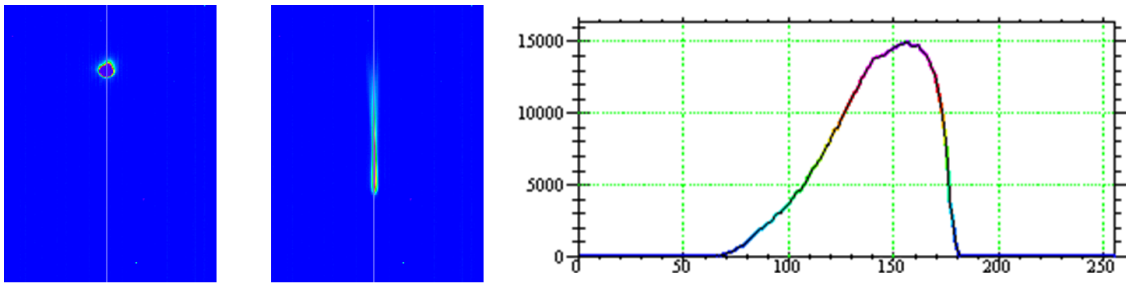


Fig 11 The table-top results. (a) Image without MOBIUS and (b) with MOBIUS. (c) The profile of MOBIUS spectrum along with the center gray line in (b). The length of the MOBIUS spectrum is about 110 pixels (3.3 mm) which corresponds to the expected result from the Zemax model (3.6 mm).

4 Conclusion

In this paper we presented MOBIUS, a cross-dispersion module that expands wavelength coverage of the existing NIR spectroscopic instrument, LUCI. As MOBIUS is installed in a slit mask frame and utilized current control hardware (*i.e.* MOS-unit), additional modification to the current instrument is not necessary. With a Littrow prism configuration, MOBIUS provides simultaneous and continuous spectrum from 0.86 μm to 2.4 μm for a single LUCI unit while having minimal impact on ensquared energy. A table-top test was performed to validate the performance of MOBIUS. With MOBIUS, LUCI can cover the NIR bands simultaneously and continuously with up

to 2.3 arcsecond of slit length. An instrument with the capabilities of MOBIUS would be useful for studies of asteroids and other faint objects in the Solar System via the mixed operating mode of LBT, such as one MODS and one MOBIUS-equipped LUCI to observe a target simultaneously from UV to NIR.

References

1 V. Reddy, T. L. Dunn, C. A. Thomas, *et al.*, "Mineralogy and surface composition of asteroids," *Asteroids IV* (2867) (2015).

2 J. M. Hill, D. S. Ashby, J. G. Brynnel, *et al.*, "The large binocular telescope: binocular all the time," in *Ground-based Airborne Telesc. V*, *Proc. SPIE* **9145**, 914502 (2014).

3 R. W. Pogge, B. Atwood, D. F. Brewer, *et al.*, "The multi-object double spectrographs for the large binocular telescope," in *Ground-based and Airborne Instrumentation for Astronomy III*, *Proc. SPIE* **7735**, 77350A (2010).

4 H. Mandel, W. Seifert, R. Hofmann, *et al.*, "LUCIFER status report: summer 2008," in *Ground-based Airborne Instrum. Astron. II*, *Proc. SPIE* **7014**, 70143S (2008).

5 B. Rothberg, O. Kuhn, M. Edwards, *et al.*, "Current status of the facility instruments at the Large Binocular telescope Observatory," in *Ground-based Airborne Instrum. Astron. VII*, *Proc. SPIE* **10702**, 1070205 (2018).

6 H. Kang, D. Thompson, A. Conrad, *et al.*, "Modular plug-in extension enabling cross-dispersed spectroscopy for large binocular telescope," in *Astronomical Optics: Design, Manufacture, and Test of Space and Ground Systems II*, **11116**, 1111606, International Society for Optics and Photonics (2019).

7 P. Buschkamp, R. Hofmann, H. Gemperlein, *et al.*, "The lucifer mos: a full cryogenic mask handling unit for a near-infrared multi-object spectrograph," in *Ground-based and Airborne Instrumentation for Astronomy III*, *Proc. SPIE* **7735**, 773579 (2010).

8 I. Ilev, "Simple autocollimation laser refractometer with highly sensitive, fiber-optic output," *Applied optics* **34**(10), 1741–1743 (1995).

9 D. W. Warren and S. Lampen, "Littrow spectrographs for moderate resolution infrared applications," in *Imaging Spectrometry XXI*, **9976**, 18–23, SPIE (2016).

10 J. Heidt and D. Thompson, "LUCI User Manual." September 7, 2016 https://sites.google.com/a/lbto.org/luci/documents-and-links.

11 M. Bass and Optical Society of America, *Handbook of optics*, New York : McGraw-Hill, New York, 2nd ed. ed. (1995).

12 J.-F. Lavigne, "Design of an infrared integral field spectrograph specialized for direct imaging of exoplanets," in *International Optical Design Conference 2006*, **6342**, 63421M, International Society for Optics and Photonics (2006).

13 I. Foppiani, M. Lombini, G. Bregoli, *et al.*, "An infrared test camera for lbt adaptive optics commissioning," in *Adaptive Optics Systems*, **7015**, 701562, International Society for Optics and Photonics (2008).

List of Figures

1 Photos of (a) LBT, (b) one unit of MODS, and (c) one unit of LUCI. Both MODS and LUCI are existing on both sides of the binocular. Therefore each side could be configured with different instruments (mixed-mode) such as LUCI and MODS[3]

2 The optical layout shows how MOBIUS works with LUCI. The MOBIUS-installed frame will be placed at the focal plane of LBT by substituting the traditional slit mask frame. With MOBIUS, LUCI is able to observe zJHK spectra in a single exposure without mixing between wavelength bands without additional modification in instrument settings.

3 Schematic figure of MOBIUS.[6] (a) The pick-off mirror is placed near the focal point of LBT to deflect the input beam path (blue lines) into the plane of the mask frame. The beam is focused right after the reflection at the entrance surface of the pick-off mirror. (b) Inside of the frame mask, the beam is collimated and dispersed (green lines). The beam is reflected from the rear surface of the prism, then focused near the original focal point with shorter wavelength is located close to the prism. This process produces the cross-dispersion before the higher dispersion grating in LUCI. MOBIUS consists of two identical spectrographs to offer sky-subtraction by dithering between target and sky position.

4 Ray diagram of Littrow prism. The apex angle (α) of prism should be equal to the refractive angle to make retro-reflection.

5 Fabricated optical components of MOBIUS. (a) The pick-off mirror is made of Zerodur and gold coated. Clear aperture is $12\ mm$ by $2\ mm$. (b) The spherical mirror is made of Zerodur and aluminum-coated. Clear aperture is $17.5\ mm$ by $9\ mm$. (c) Littrow prism with silver-coated on rear surface. The entrance surface has about $13\ mm$ by $8\ mm$ of clear aperture.

6 (a) Optical layouts of a unit of MOBIUS.[6] (b) The layout of MOBIUS mounted slit mask frame with alignment features. We light-weighted the frame to meet the weight limit of MOBIUS. Two identical spectrographs are located in plane symmetry and the slits are placed as close as possible for the sky subtraction by dithering. (c) MOBIUS with mask (black color). The mask blocks empty space of frame except the entrance to MOBIUS.

7 Spectra results at the LUCI detector. (a) When observing using LUCI and (b) LUCI with MOBIUS. With MOBIUS, spectra of each order are not overlapped up to 2.3 arcsecond of slit length. Two sets of zJHK spectra are found as the two spectrographs in MOBIUS are mirror-symmetric to allow the entrance slits to be closer together on sky.[6]

8 Spot diagrams at the focal plane of (a) LBT and (b) when MOBIUS is inserted in each wavelength band. Numbers in the figure show the rms radius of each spot diagram. Although the rms value is increased after the MOBIUS, considering the smallest expected FWHM at the focal plane delivered from the telescope is $150\ \mu m$, the image quality is seeing-limited.[6]

9 Ensquared energy comparison between (a) LUCI and (b) LUCI with MOBIUS-equipped. In every wavelength band, the difference in half width distance between LUCI and MOBIUS for 90% fraction energy is less than a pixel of the detector. This difference is insignificant as the expected seeing disk size is >2 pixels or 0.25 arcsecond.[6]

10 (a) MOBIUS with rigid aluminum frame is mounted in the table-top test setup. This frame allows alignment and testing of the MOBIUS optics in their proper positions. (b) The test setup of MOBIUS.

11 The table-top results. (a) Image without MOBIUS and (b) with MOBIUS. (c) The profile of MOBIUS spectrum along with the center gray line in (b). The length of the MOBIUS spectrum is about 110 pixels ($3.3\ mm$) which corresponds to the expected result from the Zemax model ($3.6\ mm$).

APPENDIX E

Modular plug-in extension enabling cross-dispersed spectroscopy for Large Binocular Telescope

Hyukmo Kang, David Thompson, Al Conrad, Conrad Vogel, Ariel Lamdan, and Dae Wook Kim

Publisher's permission is hereby granted under the following conditions: (1) the material to be used has appeared in our publication without credit or acknowledgment to another source; and (2) you credit the original SPIE publication. Include the authors' names, title of paper, volume title, SPIE volume number, and year of publication in your credit statement.

Modular plug-in extension enabling cross-dispersed spectroscopy for Large Binocular Telescope

Hyukmo Kang[a], David Thompson[b], Al Conrad[b], Conrad Vogel[b], Ariel Lamdan[a], and Dae Wook Kim[a,b,c]

[a]James C. Wyant College of Optical Sciences, University of Arizona, 1630 E. University Blvd., Tucson, AZ 85721 USA
[b]Large Binocular Telescope Observatory, 933 N. Cherry Ave., Tucson, AZ, 85721 USA
[c]Department of Astronomy, University of Arizona, 933 N. Cherry Ave., Tucson, AZ, 85721 USA

ABSTRACT

The LUCI (LBT Utility Camera in the Infrared) instruments are a pair of near infrared (NIR) imagers and spectrographs for the Large Binocular Telescope (LBT) that include a set of cryogenic exchangeable focal plane masks. Although LUCI covers the NIR zJHK bands at different resolutions with existing gratings, it is not currently possible to get zJHK in a single exposure with a single LUCI which is required for some planetary science programs. To produce a simultaneous zJHK spectrum with a single LUCI, we designed a system consisting of small and simple optical elements to fit within the limited space in the focal plane mask frame to cross-disperse fixed short slits. This system, called MOBIUS (Mask-Oriented Breadboard Implementation for Unscrambling Spectra), consists of a double-folding mirror, a collimating spherical mirror with 180 mm radius of curvature, and a dispersing prism with the rear surface mirror-coated. MOBIUS disperses the input slit perpendicular to the dispersion direction of the gratings in LUCI. The resulting order separation is at least ~2.7 arcsecond, allowing a slit length of up to ~2.3 arcsec without mixing orders at the LUCI image plane. Since MOBIUS would be introduced into the existing light path via the exchangeable slit mask mechanism, no modification to the current LUCI instrument is needed. Eventually, binocular observations combining one of the Multi-Object Double Spectrographs (MODS) with LUCI+MOBIUS at the LBT will provide simultaneous coverage from 0.3 to 2.4 μm for studies of asteroids and other faint solar system bodies.

Keywords: LBT, LUCI, Spectrograph, Cross dispersion, Instrument Design

1. INTRODUCTION

The LUCI (LBT Utility Camera in the Infrared) instruments are a pair of near infrared (0.89 μm to 2.4 μm) imagers and spectrographs for the Large Binocular Telescope (LBT)[1–4] (Fig. 1). LUCI1 and LUCI2 are installed at the front Bent-Gregorian f/15 focal stations of the LBT, and are equipped with a set of cryogenic exchangeable focal plane masks. Both LUCIs provide imaging, long-slit and Multi Object Spectroscopy (MOS) over a 4 square arcminute field of view as well as adaptive optics corrected imaging and spectroscopy over a 30 arcsecond field of view.

Currently, we can use both LUCIs simultaneously to get a spectrum covering the zJHK bands (zJ and HK).[4] We can extend the coverage down to 0.32 μm by running one MODS (The Multi-Object Double Spectrographs)[5] and one LUCI, at the expense of either the zJ or HK bands. It would be of benefit to extend the simultaneous coverage over the full range.

In this paper, we report on our design of a cross-disperser module called MOBIUS (Mask-Oriented Breadboard Implementation for Unscrambling Spectra) to produce a simultaneous zJHK spectrum with a single LUCI as shown in Fig. 2. Requirements for the MOBIUS design included that there would be no modifications to the existing LUCI

Further author information: (Send correspondence to David Thompson)
David Thompson: E-mail: dthompson@lbto.org

Astronomical Optics: Design, Manufacture, and Test of Space and Ground Systems II, edited by Tony B. Hull, Dae Wook Kim, Pascal Hallibert, Proc. of SPIE Vol. 11116, 1111606 · © 2019 SPIE
CCC code: 0277-786X/19/$21 · doi: 10.1117/12.2528865

Downloaded From: https://www.spiedigitallibrary.org/conference-proceedings-of-spie on 19 Sep 2019
Terms of Use: https://www.spiedigitallibrary.org/terms-of-use

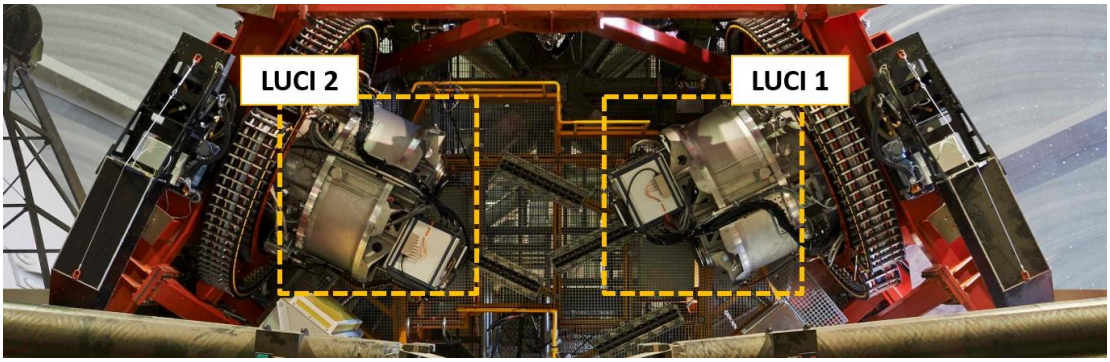


Figure 1. LUCIs on LBT.[6] LUCIs can have same (twinned mode) or different configurations (fraternal twin mode).[4] Also, at the binocular mode of LBT, each side could be configured with different instruments (mixed-mode) such as LUCI and MODS

instruments and that it would not affect the image quality of LUCI. This is achieved by mounting MOBIUS inside of the slit mask frame, located at the telescope focal plane. To demonstrate that the plug-in extension would not degrade performance of LUCI, we compare the spot radius and ensquared energy of each band with and without MOBIUS. By combining this system with MODS through binocular observations, MOBIUS in LUCI provides simultaneous coverage from UV to NIR.[4]

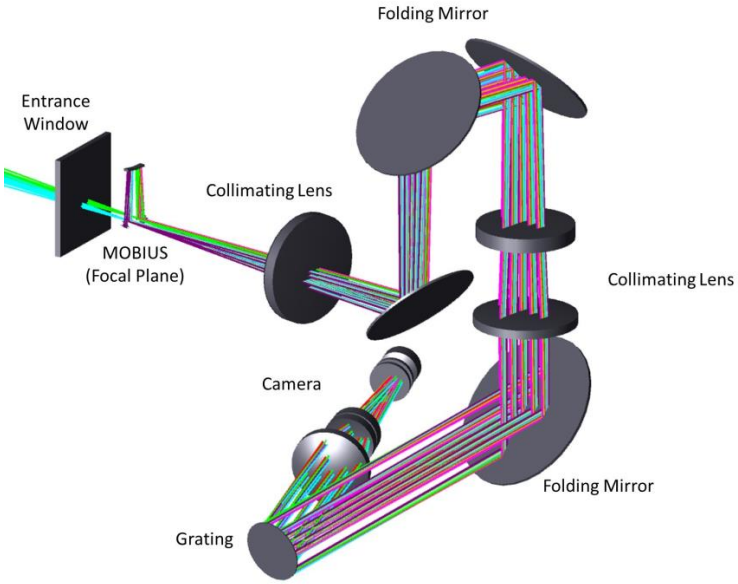


Figure 2. Optical layout shows MOBIUS introduced at the focal plane of LBT. By substituting the traditional slit frame mask with MOBIUS, LUCI is able to produce zJHK spectrum in a single exposure without any modifications in current instrument settings.

Downloaded From: https://www.spiedigitallibrary.org/conference-proceedings-of-spie on 19 Sep 2019
Terms of Use: https://www.spiedigitallibrary.org/terms-of-use

2. OPTICAL DESIGN OF MOBIUS

2.1 Concepts

The concept of MOBIUS is a modular cross-dispersing unit that can easily be deployed to and removed from the focal plane in LUCI without any other modifications to the current instrument. This characteristic provides broad band coverage (0.89 μm to 2.4 μm) in a single LUCI subject to scientific objectives with low cost and risk.

For that purpose, MOBIUS would be built into one of the exchangeable slit mask frames that are stored and handled by the MOS unit.[7] Then the MOBIUS-integrated mask frame would be placed in the focal plane of the LBT, and disperse the image of the slit perpendicular to the dispersion direction of the higher resolution gratings in LUCI. These concepts require that MOBIUS preserves the optical properties of the incident beam (e.g. position of focal plane, f-number, chief ray angle) and the image quality at the detector plane of LUCI. Additionally, the cross-dispersed distance between orders should be large enough to secure the required slit length while avoiding overlap. The current design of MOBIUS is optimized for the N3.75 camera with the G040 grating, so the minimum dispersion distance between orders should be larger than 1 mm to achieve the required slit length of 2 arcseconds or more. Lastly, two identical cross-disperser modules will be built into a single mask frame side by side, allowing for sky-subtraction by dithering between source and sky positions.

Figure 3 shows the schematic concept of MOBIUS. The incident beam from the LBT reflects off the side of a triangle pick-off mirror towards the inside of the mask frame. It is then collimated via a spherical mirror before entering the dispersing prism. The prism has a mirror-coated rear surface and is tilted to cause retroreflection. These processes happen in the plane of the slit mask, and the dispersed beam returns to the pick-off mirror. At this point, the beam hits the other side of triangle, and is directed into LUCI. As long as the ray angles and focal plane of the MOBIUS dispersed beams nominally match that of the initial LBT beam, the condition being that no rays are vingetted, the LUCI detector will see four spectra, each corresponding to a different NIR band. Therefore, MOBIUS can provide broad band coverage without any adjustments to the current instrument.

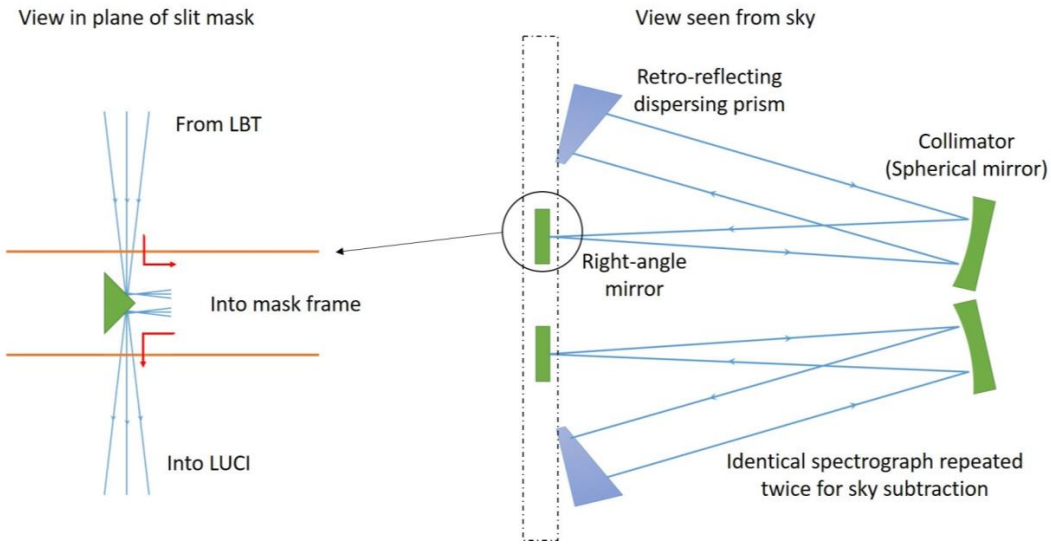


Figure 3. Schematic figure of MOBIUS a modular cross-disperser for LUCI. The right-angle mirror is inserted near the focal point of LBT to deflect the incoming beam from the LBT into the mask frame. Inside of the frame mask the beam is collimated and dispersed, then it is returned to the previous light path. Through this process, the input beam is cross dispersed before the higher dispersion grating in LUCI.

Downloaded From: https://www.spiedigitallibrary.org/conference-proceedings-of-spie on 19 Sep 2019
Terms of Use: https://www.spiedigitallibrary.org/terms-of-use

2.2 Optical Design

The components of MOBIUS are simple: a double folding mirror, a spherical mirror, and a dispersing prism. The double folding mirror is made of Zerodur and is shaped like a right-angle prism. This is located near the focal point of LBT to deflect the incident beam into the slit mask frame.

The collimator, a Zerodur spherical mirror with 180 mm radius of curvature, is located at the focal length of the spherical mirror from the focal point of the LBT, and tilted so the collimated beam does not hit the right-angle mirror. Typically an off-axis parabolic (OAP) mirror is used as a collimator, but we adopted a spherical mirror because with the slow f/15 beam from the telescope there is no significant difference in the Strehl's ratio between an OAP and a spherical mirror. Furthermore, the use of a spherical mirror is advantageous in fabrication and alignment.

The dispersion prism is made of Strontium Titanate ($SrTiO_3$). Strontium Titanate is a material transmissive in the operating temperature and wavelengths.[8] The apex angle of the prism is 19°, and it is tilted to cause retroreflection at the rear surface that is mirror-coated. The dispersed beam from the prism is returned to the other side of the right-angle mirror, and propagates into LUCI. As a consequence, the minimum separation of order by MOBIUS is ~1.6 mm at the focal plane of the LBT.

The optical design of a unit of MOBIUS is shown in Fig. 4(a). Fig. 4(b) shows the overall layout of MOBIUS with two identical mini spectrographs are located side by side to provide sky subtraction by dithering.

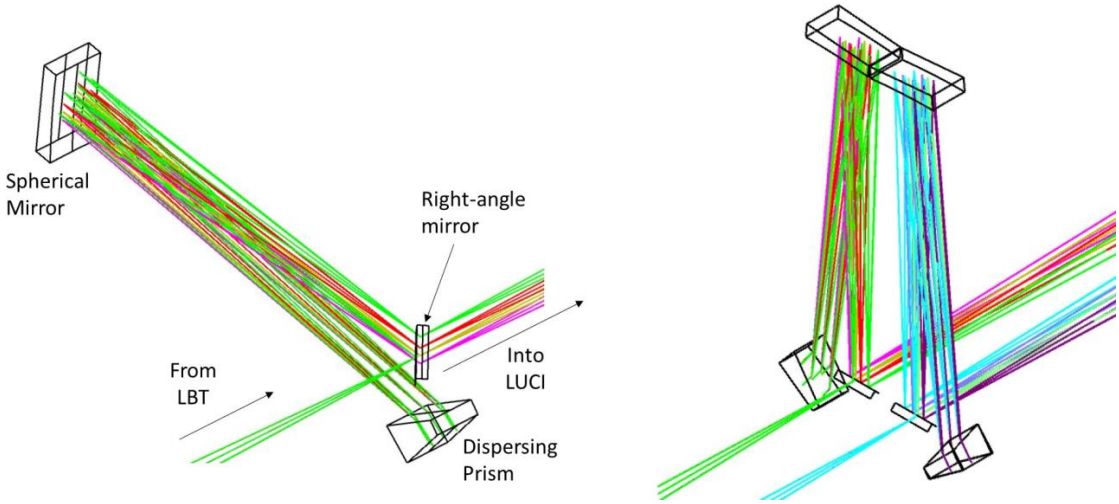


Figure 4. Optical layouts of MOBIUS. (a) shows an unit of MOBIUS. and (b) shows the overall layout of MOBIUS with two identical spectrograph units located side by side. For the sky subtraction by dithering, we flipped one unit to allow placement of the two entrance slits as close as possible.

Since MOBIUS needs to fit within a limited space (150 x 150 x 12 mm), the maximum width of optical elements is limited by the thickness of the slit mask frame (Fig. 5). Also, additional weight of the slit frame should be less than 20 grams so that the MOBIUS can be safely handled by the MOS-unit and focal plane unit of LUCI.

Downloaded From: https://www.spiedigitallibrary.org/conference-proceedings-of-spie on 19 Sep 2019
Terms of Use: https://www.spiedigitallibrary.org/terms-of-use

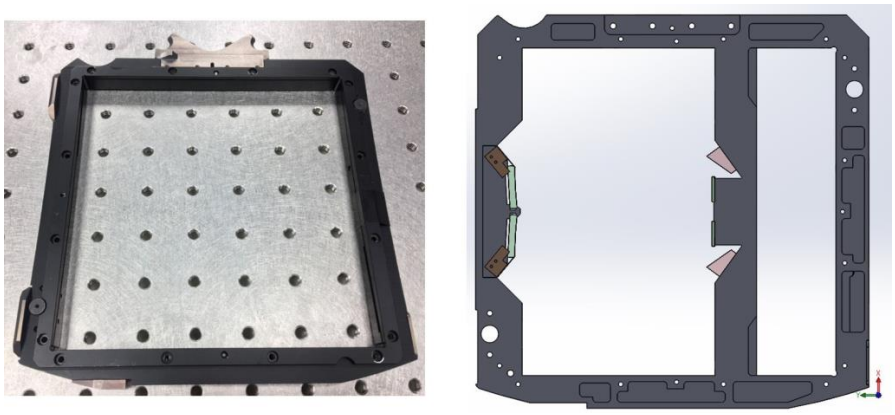


Figure 5. Slit frame of LUCI (left) and estimated 3D modelling of MOBIUS built in the frame (right). To compensate the additional weights of MOBIUS, light weighting features are included in the frame.

3. RESULT AND PERFORMANCE

Figure 6 shows how MOBIUS works with LUCI. Without MOBIUS (Fig. 6(a)), the footprint of different orders are dispersed in a line and overlapped such that they are indistinguishable. MOBIUS generates perpendicular dispersion that gives spectra without overlap (Fig. 6(b)). Because we put two mini cross dispersers, there are two sets of zJHK spectra, one for the target the other for sky subtraction. The configuration with N3.75 camera and G040 grating allows a slit length up to ~2.3 arcsecond at the LUCI image plane without mixing orders.

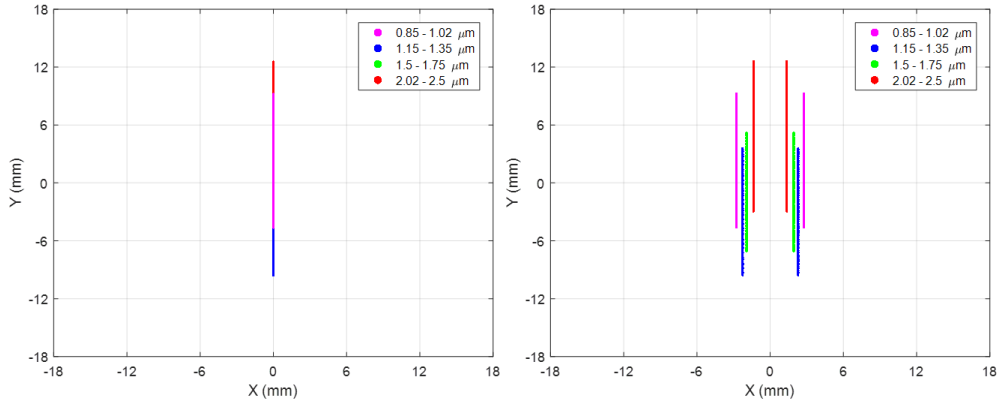


Figure 6. Footprint diagram at the detector when observing (a) only using LUCI and (b) LUCI with MOBIUS. With MOBIUS, spectra of each order are not overlapped. MOBIUS allows slit length up to ~2.3 arcsecond.

As a plug-in extension for LUCI, it is important not to degrade the image quality after introducing MOBIUS. To verify that the image quality remains the same, we compared the *rms* spot radius at the focal plane of the LBT and at the focal plane that is formed after MOBIUS (Fig 7). The radius of *rms* spot size has increased in every band after MOBIUS is introduced, however, it is still equivalent to the size of the Airy's disk. We also compare the ensquared

Downloaded From: https://www.spiedigitallibrary.org/conference-proceedings-of-spie on 19 Sep 2019
Terms of Use: https://www.spiedigitallibrary.org/terms-of-use

energy at the LUCI detector (Fig. 8). The greatest difference in half width distance for 90% fraction energy is at K band, which is about 2 μm. Considering the pixel size of the detector is 18 μm,[6] and the seeing disk delivered by the telescope is >2 pixels on the N3.75 camera, MOBIUS would not be a limitation to the delivered image quality. These results show that the MOBIUS can expand wavelength coverage of LUCI with little penalty.

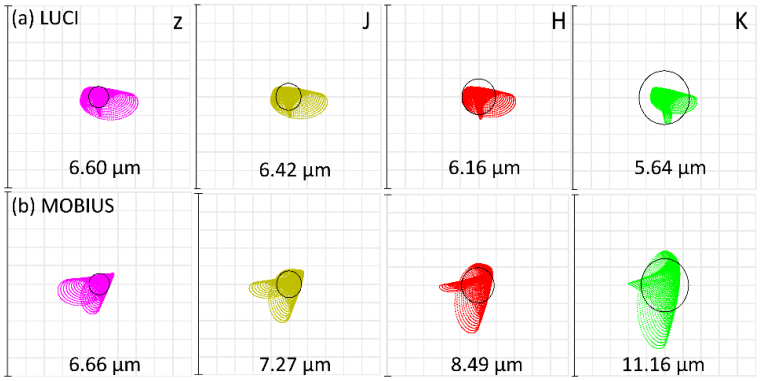


Figure 7. Spot diagrams at the focal plane of LBT when (a) LUCI only and (b) LUCI+MOBIUS is applied. The numbers in figure represent the rms spot radius of each spot diagram. Although the rms spot radius is slightly increased after the MOBIUS, it is still nearly the size of Airy's disk. Also, considering the smallest expected FWHM at the focal plane delivered from the telescope is 150 µm or 0.25 arcsecond, the image quality is dominated by the atmospheric seeing.

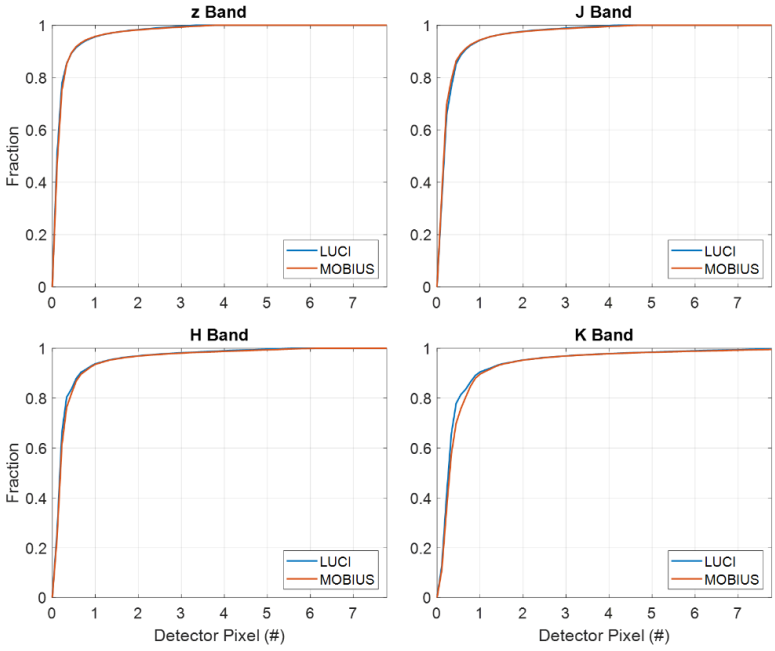


Figure 8. Ensquared energy comparison between LUCI and LUCI with MOBIUS. The difference in half width distance between LUCI and MOBIUS for 90% fraction energy is less than a pixel (on detector). Considering the seeing disk is >2 pixels or 0.25 arcsecond, this difference is insignificant.

Downloaded From: https://www.spiedigitallibrary.org/conference-proceedings-of-spie on 19 Sep 2019
Terms of Use: https://www.spiedigitallibrary.org/terms-of-use

4. CONCLUSION

We presented a slit mask based cross disperser expansion module which enables existing spectroscopic instruments to cover broad bands in a single exposure. Since MOBIUS utilizes the current mask frame and hardware, it is not required to modify the current instrument set up. MOBIUS provides simultaneous and continuous spectrum from 0.89 μm to 2.4 μm, while at most generating negligible variation in optical performance. Binocular observations with one MODS and one MOBIUS-equipped LUCI is expected to provide simultaneous coverage from UV to NIR.

ACKNOWLEDGEMENT

We also want to thank the people who contributed to the editing and reviewing of the manuscript. A special thank you goes to John Kam who helped edit and gave feedback on the article.

REFERENCES

[1] Seifert, W., Appenzeller, I., Baumeister, H., Bizenberger, P., Bomans, D., Dettmar, R.-J., Grimm, B., Herbst, T., Hofmann, R., Juette, M., Laun, W., Lehmitz, M., Lemke, R., Lenzen, R., Mandel, H., Polsterer, K., Rohloff, R.-R., Schuetze, A., Seltmann, A., Thatte, N. A., Weiser, P., and Xu, W., "LUCIFER: a MultiMode NIR Instrument for the LBT," in [*Instrum. Des. Perform. Opt. Ground-based Telesc.*], *Proc. SPIE* **4841**, 962 (2003).

[2] Mandel, H., Seifert, W., Hofmann, R., Ju¨tte, M., Lenzen, R., Ageorges, N., Bomans, D., Buschkamp, P., Dettmar, R.-J., Feiz, C., Gemperlein, H., Germeroth, A., Geuer, L., Heidt, J., Knierim, V., Laun, W., Lehmitz, M., Mall, U., Mu¨ller, P., Naranjo, V., Polsterer, K., Quirrenbach, A., Sch¨affner, L., Schwind, F., Weiser, P., and Weisz, H., "LUCIFER status report: summer 2008," **7014**, 70143S (2008).

[3] Hill, J. M., Ashby, D. S., Brynnel, J. G., Christou, J. C., Little, J. K., Summers, D. M., Veillet, C., and Wagner, R. M., "The large binocular telescope: binocular all the time," in [*Ground-based Airborne Telesc. V*], *Proc. SPIE* **9145**, 914502 (2014).

[4] Rothberg, B., Kuhn, O., Edwards, M., Hill, J., Thompson, D., Veillet, C., Wagner, R. M., and Power, J., "Current status of the facility instruments at the Large Binocular telescope Observatory," in [*Ground-based Airborne Instrum. Astron. VII*], *Proc. SPIE* **10702**, 1070205 (2018).

[5] Pogge, R. W., Atwood, B., Brewer, D. F., Byard, P. L., Derwent, M. A., Gonzalez, R., Martini, P., Mason, J. A., O'Brien, T. P., Osmer, P. S., Pappalardo, D. P., Steinbrecher, D. P., Teiga, E. J., and Zhelem, R., "The multi-object double spectrographs for the large binocular telescope," in [*Ground-based and Airborne Instrumentation for Astronomy III*], *Proc. SPIE* **7735**, 77350A (2010).

[6] Heidt, J. and Thompson, D., "LUCI User Manual." September 7, 2016 https://sites.google.com/a/lbto.org/luci/documents-and-links.

[7] Buschkamp, P., Hofmann, R., Gemperlein, H., Polsterer, K., Ageorges, N., Eisenhauer, F., Lederer, R., Honsberg, M., Haug, M., Eibl, J., et al., "The lucifer mos: a full cryogenic mask handling unit for a nearinfrared multi-object spectrograph," in [*Ground-based and Airborne Instrumentation for Astronomy III*], *Proc. SPIE* **7735**, 773579 (2010).

[8] Dore, P., De Marzi, G., and Paolone, A., "Refractive indices of SrTiO3 in the infrared region," *Int. J. Infrared Millimeter Waves* **18**, 125–138 (1997).

Downloaded From: https://www.spiedigitallibrary.org/conference-proceedings-of-spie on 19 Sep 2019
Terms of Use: https://www.spiedigitallibrary.org/terms-of-use